

Modification and Analysis of a Multimegawatt Floating Spar Wind Turbine

Vegard Milde



Master's thesis in Energy

UNIVERSITY OF BERGEN
GEOPHYSICAL INSTITUTE

November, 2021

Acknowledgements

This 60 ECT master thesis is written as a part of the Integrated Master's programme in Energy at the Geophysical Institute of the University of Bergen.

I would like to extend my gratitude to my main supervisor Marte Godvik. I greatly appreciate your patient guidance through a year of ups and downs, quarantines and online meetings. Thank you for always being helpful and supportive. I would also like to thank co-supervisor Astrid Nybø. I greatly appreciate our productive discussions, and all the feedback you have given me. I feel very lucky for having your support. Thank you, Professor Finn Gunnar Nielsen for sharing your great knowledge of the field of offshore wind, and for providing me with the fundamental theory that this thesis is built upon.

Thank you Ane Vatshelle for providing a method for modeling the tower of an offshore floating wind turbine in MATLAB.

Lastly, I want to thank Bendik Husa and Tarje Hillersøy for all your support and technical assistance throughout this year. Thank you for all the great memories we share from our time at the University. You made it fun.

Abstract

This thesis presents methods and theory for adjusting a floating spar wind turbine model in OpenFAST. This work is based on the WindCrete model created by the CoreWind project. The WindCrete model is adjusted to fit the environmental conditions of the Utsira site off the coast of south-western Norway. The work includes adjustments of the wind turbine tower, support platform, and mooring layout. The wind turbine tower is adjusted in both wall thickness and diameter to ensure structural integrity. The natural frequencies of the tower must lie outside the frequency of the rotating turbine blades. This prevents resonant oscillations that may cause structural fatigue and instability. Ballast is added to the support platform interior, to maintain the platform static equilibrium. The mooring layout is adjusted to fit a new water depth. The design process is iterative, resulting in an adjusted model that satisfies all predefined structural requirements. The final model is tested through simulation to investigate model characteristics under different load cases. Analysis of these simulations showed that the adjusted OpenFAST model behaves as expected. The characteristics of the final adjusted platform satisfy the same predesign basis and design limitations as the original WindCrete model is built upon.

Contents

| | | |
|----------|---|-----------|
| 1 | Introduction | 1 |
| 1.1 | Background and motivation | 1 |
| 1.2 | Objective | 3 |
| 2 | Theory | 4 |
| 2.1 | Definition of the spar floating wind turbine | 4 |
| 2.1.1 | Rotor Nacelle Assembly | 5 |
| 2.1.2 | Tower | 5 |
| 2.1.3 | Support platform | 6 |
| 2.1.4 | Mooring | 6 |
| 2.1.5 | Controller | 7 |
| 2.1.6 | Rigid body motions | 8 |
| 2.2 | Idealized Euler-Bernoulli beam | 9 |
| 2.3 | Floater theory and equations | 10 |
| 2.3.1 | Catenary equations | 10 |
| 2.3.2 | Moments of inertia | 10 |
| 2.3.3 | Metacentric height | 11 |
| 2.3.4 | Platform inertia matrix | 13 |
| 2.3.5 | Added mass matrix - strip theory | 13 |
| 2.3.6 | Hydrostatic stiffness matrix | 15 |
| 2.3.7 | Mooring stiffness matrix | 15 |
| 2.3.8 | Morison's equation | 16 |
| 2.4 | Wave and wind fields | 16 |
| 2.4.1 | JONSWAP spectrum | 16 |
| 2.4.2 | Turbulent wind field | 17 |
| 3 | Background, tools and site conditions | 19 |
| 3.1 | OpenFAST | 19 |
| 3.1.1 | Sub-modules | 20 |
| 3.2 | BModes | 23 |
| 3.2.1 | Basic principles | 23 |
| 3.3 | IEA 15-MW Reference | 24 |
| 3.4 | CoreWind WindCrete | 26 |
| 3.4.1 | The WindCrete model | 27 |
| 3.4.2 | The WindCrete support platform | 27 |
| 3.4.3 | WindCrete controller | 28 |
| 3.5 | Site descriptions | 29 |
| 3.5.1 | Environmental conditions in wind turbine design | 29 |
| 3.5.2 | Gran Canaria Island | 30 |
| 3.5.3 | Utsira | 30 |
| 4 | Utsira design | 31 |
| 4.1 | Motivation | 31 |
| 4.2 | Adjustment process | 31 |

| | | |
|----------|---|-----------|
| 4.2.1 | Structural requirements | 33 |
| 4.2.2 | Tower model | 34 |
| 4.2.3 | Support platform model | 36 |
| 4.3 | Additional requirements | 37 |
| 4.3.1 | Blade rotation frequencies | 38 |
| 4.3.2 | Blade tip clearance | 38 |
| 4.3.3 | Center of rotation | 39 |
| 4.4 | Adapting mooring to new depth | 42 |
| 4.4.1 | Deciding on a layout | 43 |
| 4.4.2 | Calculations of new mooring line dimensions | 43 |
| 4.4.3 | Static layout | 45 |
| 4.4.4 | Touchdown point | 47 |
| 4.5 | Finding new tower modes | 50 |
| 4.5.1 | BModes input data | 50 |
| 4.5.2 | Post-processing of BModes output data | 53 |
| 4.6 | New inputs | 56 |
| 5 | Simulation results | 57 |
| 5.1 | Platform equilibrium | 57 |
| 5.2 | Decay tests | 58 |
| 5.2.1 | Tower FA and SS frequencies through OpenFAST | 60 |
| 5.3 | Stability at different environmental conditions | 63 |
| 5.3.1 | Turbulent wind and waves | 64 |
| 6 | Summary and conclusion | 75 |
| 7 | Future work | 77 |
| | Appendices | 82 |
| A | OpenFAST input | 82 |
| B | OpenFAST output | 84 |

Acronyms

| | |
|----------|--|
| API | Application Programming Interface |
| CM | Center of Mass |
| CoG | Center of Gravity |
| CoB | Center of Buoyancy |
| COREWIND | COst REDuction and increase of performance of floating WIND technology |
| DNV | Det Norske Veritas |
| DoF(s) | Degree(s) of Freedom |
| DTU | Technical University of Denmark |
| HAWC2 | Horizontal Axis Wind turbine simulation Code (2nd generation) |
| IEA | International Energy Agency |
| IEC | International Electrotechnical Commission |
| JONSWAP | JOint North Sea WAve Project |
| MSL | Mean Sea Level |
| NREL | National Renewable Energy Laboratory |
| RNA | Rotor Nacelle Assembly |
| OC3 | Offshore Code Comparison Collaboration |
| ROSCO | Reference OpenSource COntroller |
| SWL | Still Water Level |
| TCP | Technology Collaboration Programme |
| UMaine | University of Maine |

1 INTRODUCTION

1.1 Background and motivation

Floating offshore wind is a rapidly growing emerging market, and northern Europe is leading this growth [Afewerki et al., 2019]. As offshore wind farms are deployed in deeper water, floating wind turbines are needed. The technology is maturing, and turbine capacities are increasing. The average rated capacity for installed turbines in Europe was 8.2 MW in 2020, with new projects trending towards turbines with capacity up to 13 MW [WindEurope, 2021]. There is a need for technological innovation for this trend to continue.

There exist several proven design concepts for multi-megawatt floating offshore wind turbines, each with its own strengths and limitations. Two commonly used support platform designs are the semi-submersible concept and the spar concept. In the semi-submersible concept, the tower is typically mounted on a three-legged pontoon. Each pontoon is connected to a vertical column. These columns contain ballast, and provide stability through buoyancy. Of course, there exist different geometries and designs of these support platforms, but the stability principle remains the same. Semi-submersible platforms are typically moored with catenary mooring lines. These platforms are well suited to be placed in shallower waters, as they have a relatively small draft. The first semi-submersible wind farm in operation is named Windfloat Atlantic, and has been operational since July, 2020 [Windfloat Atlantic, 2021].

For deeper waters, the spar concept is a well-proven design. A spar floating wind turbine is a single cylinder column support platform equipped with a wind turbine tower and rotor, see Figure 1. This concept relies on ballast in its deep draft to provide stability by gravity. It is a simple and cost-effective design that first was demonstrated by Equinor at a multi-megawatt scale in 2009 through the Hywind Demo project [Hywind Demo, 2009]. This demo proved successful, laying the foundation for the 30 MW Hywind Scotland pilot park [Hywind Scotland, 2017]. This is the world’s first floating wind farm, and has been producing electricity since October, 2017. It consists of five 6 MW turbines, with a rotor diameter of 154 m.

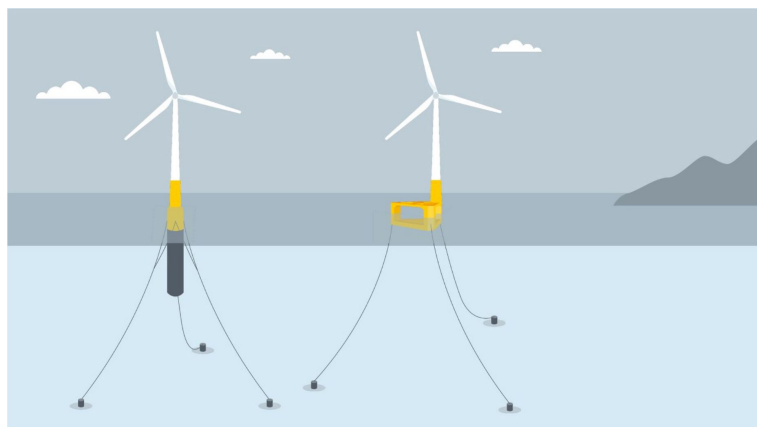


Figure 1: Two main design concepts for offshore wind, as designed by Equinor: the spar (left) and the semi-submersible (right). Figure from [Equinor2021]

The European Union is committed to becoming climate-neutral within 2050 [Green Deal, 2021]. Through the Green Deal, the European Commission outlines an ambitious vision of up to 450 GW installed capacity of offshore wind by 2050. Floating offshore wind is a key component to make this possible. A report written by BVG Associates for WindEurope outlines optimal areas for offshore wind to be deployed to achieve the goals set by the Green Deal [Freeman et al., 2019]. According to this report, approximately 380 GW of offshore wind is expected to be installed in the North Seas. This is equivalent to allocating approximately 2.8% of the total area of the North Seas to offshore wind installations. Though Norway is not a part of the EU, there is a huge potential for offshore wind energy within its North Sea territories. One such area well suited for offshore wind is Utsira Nord.

On June 12th, 2020, the Norwegian Ministry of Petroleum and Energy opened two areas dedicated to offshore renewables [Government, 2020]. Utsira Nord is one of these areas, and is well suited for floating wind turbines. The government is now in the process of adapting laws governing offshore energy production before concessions can be given. The site area is 1010 km², with an estimated floating wind turbine capacity of 1500 MW [Drivenes et al., 2010]. Water depths vary between 185-280 m, which makes it a well suited site for floating spar platforms.

This thesis investigates a spar floating wind turbine model, secured with three catenary mooring lines [Mahfouz et al., 2020]. The spar floater concept in focus is named WindCrete, developed by the "cost reduction and increase of performance of floating wind technology" project (COREWIND) [CoreWind, 2021]. The WindCrete model is designed to support the Rotor Nacelle Assembly (RNA) from the International Energy Agency (IEA) Wind 15 MW reference wind turbine [Gaertner et al., 2020b]. This reference turbine is originally designed for a monopile bottom-fixed foundation. In the WindCrete model, the support platform, and consequently the tower, is adapted to the floating concept. In addition, the WindCrete concept uses concrete in both support platform and tower, as opposed to the steel tower used in the reference model. This is done in an effort to lower the cost of construction, as cost reduction is one of the main goals for the COREWIND project. The WindCrete tower and support platform is designed to satisfy all structural requirements that follow from the environmental conditions of a Gran Canaria site. These structural requirements are based on the International Electrotechnical Commission (IEC) 61400-3-2 standard [IEC TS 61400-3-2:2019].

1.2 Objective

The objective of this thesis is to adjust the WindCrete model to the environmental conditions present at Utsira Nord offshore wind site. The adjustment is based on the WindCrete spar floater OpenFAST model, created by the CoreWind project [Molins et al., 2020]. I aim to adjust this model to withstand the more extreme environmental conditions of the Utsira Nord site. I will achieve this with three main adjustment steps.

The first step is to adjust the tower. In the WindCrete model, the tower structure is made of concrete. I choose to model the tower using steel, as used in the tower of the bottom-fixed IEA 15MW reference wind turbine model. Because of this design choice, I will increase tower height, to account for rougher seas and higher waves found off the coast of south-western Norway. The new tower must be strengthened to withstand the greater loads applied to the structure. I will use a combination of adjusting the tower radius as well as the wall thickness to ensure structural integrity. In general, I aim to adjust the tower following structural requirements from the IEC standard [IEC TS 61400-3-2:2019].

The second step is to adjust the internal ballast of the spar subplatform, to compensate for the new tower structure. The weight of the tower is significantly decreased when using steel instead of concrete. The main objective is to keep the platform position in equilibrium equal for the new design, with a special focus on vertical displacement. This requires ballast to be added to the subplatform, which alters subplatform properties. Updated values must be calculated, as they are required as input in the OpenFAST model.

The third step is to adjust the mooring layout to fit the increased depth of the Utsira Nord site. The new mooring layout will be based on the catenary design used in the WindCrete project. I will increase the anchoring radius and main chain length, to fit the layout to the new water depth. The main focus will be to avoid uplifting forces at the anchors under all conditions, as well as to maintain good stationkeeping capabilities.

Finally I will demonstrate the stability and performance of the adapted OpenFAST model. I will verify model properties through simulation, and discuss results. This thesis goes into detail on the procedure a wind turbine designer must follow when adjusting an existing design to a new location and a new tower material. This process is iterative, and I use simulation results to do readjustments to the model in all steps.

A significant part of my work will be to learn OpenFAST, with focus on how to use a model, and how to adjust this model to fit new structural requirements. This requires knowledge of several submodule input parameters, as both environmental conditions and structural properties are adjusted. I also aim to familiarize myself with available output options, and how to manipulate these outputs to investigate model properties. This includes post-processing output data in MATLAB.

This thesis aims to contribute to the development and optimization of floating wind turbines. Sustainable development of wind turbines will contribute to affordable and clean energy to more people (goal 7) and innovations relevant for the industry (goal 9). The deployment of floating wind turbines has a low impact on the life below water (goal 14) and may replace fossil energy sources, which is a positive climate act (goal 13).

2 THEORY

Central components of a spar floating wind turbine are defined in the following subsections. The rigid body motions of the floater are also defined. Finally, some theory on the wave and wind fields used in this thesis are presented.

2.1 Definition of the spar floating wind turbine

Figure 2 displays a typical design for a spar floating wind turbine. I use the WindCrete OpenFAST model as a base, and do adjustments to the tower, ballast and mooring to adapt the new model to the environmental conditions of the Utsira site. Because of the design choice of using steel as material in the tower, it is more natural to compare structural integrity with the steel tower from the bottom-fixed IEA 15MW reference turbine. For that reason, Section 2.1.2 describes the reference tower, and not the WindCrete model tower.

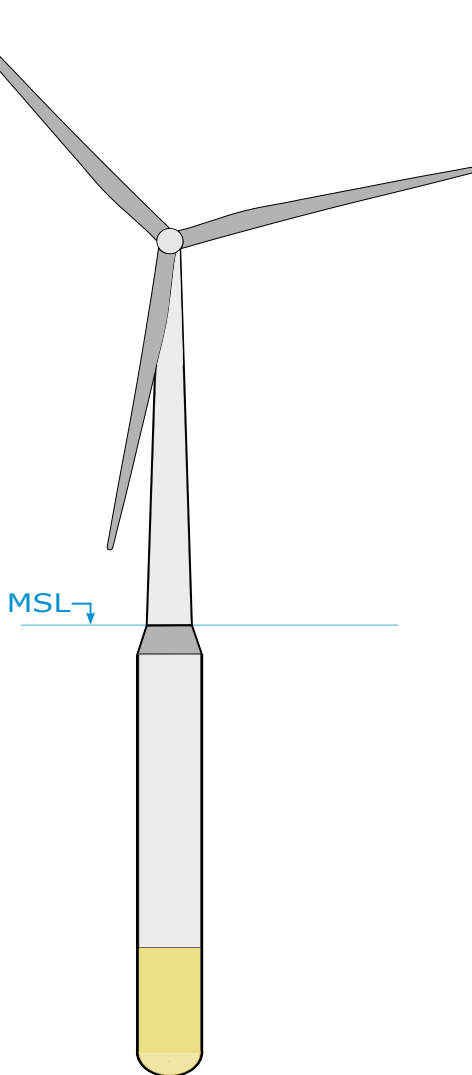


Figure 2: A typical spar floating wind turbine design. Adapted from [Mahfouz et al., 2020].

2.1.1 Rotor Nacelle Assembly

The rotor nacelle assembly (RNA) is the structure mounted on top of the tower of a wind turbine, see Figure 3. This structure houses the power-generating components. The turbine blades are connected to the hub which is placed at the top of the tower. These components make up the rotor. The wind exerts a force on the blades, causing the rotor to rotate. The rotor is connected to a generator through a driveshaft. The IEA 15-MW reference wind turbine is designed with a permanent-magnet generator, which is a simple design that allows a direct-drive layout. The whole structure rests on a bedplate, which transmits all loads and forces from the RNA to the tower. A yaw bearing allows the RNA to rotate, so that the rotor plane always faces the wind direction. The RNA center of mass (CM) is typically shifted off the central vertical tower axis, causing the floating wind turbine to have a rotational pitch displacement in its equilibrium position.

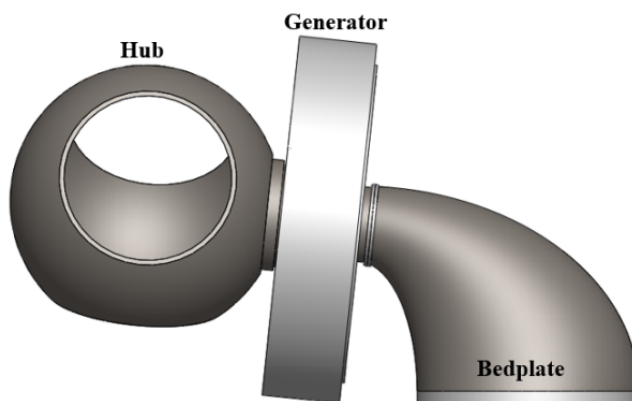


Figure 3: The IEA-15MW reference turbine RNA. [Gaertner et al., 2020b]

2.1.2 Tower

The tower is a cylindrical beam that connects the RNA to the support platform. The IEA 15-MW reference tower is a steel structure with a common design. It is a thin-walled cylinder with decreasing radius from the tower base to the tower top. This structure must be strong enough to carry the weight of the RNA, and withstand the loads and forces transmitted from the RNA. The tower is subjected to large bending stresses throughout its height, especially if mounted on a floating support platform that allows significant tilting. It must be designed with enough height to give good clearance between the blade tip and the water surface. The design must also consider interactions with the rotor. The frequencies of the tower structures natural vibrations must lie outside the frequencies induced by the rotor, to avoid resonance. Towers mounted on a floating subplatform is typically stiffer, which shifts the tower mode frequencies away from frequency range that causes resonance. This design consideration is further investigated in Chapter 3.2.

2.1.3 Support platform

The support structure of the WindCrete floating turbine is a spar cylinder. A spar is a slender, hollow column with a deep draft. The large ratio of draft over diameter is the central principle of stability for this design. The bottom part of the substructure is ballasted internally, to provide stability and to counteract the buoyancy force. This ballast may either be a solid aggregate such as concrete, or a liquid such as sea water. The spar support platform is a very simple geometry, which makes production relatively simple. The deep draft of the spar makes it well suited to be placed in deeper waters. However, the deep draft of the spar design also makes installation and transportation challenging. Installation of the subplatform, tower and RNA near land or in a port would require a passage of deep waters all the way from the port to the final wind turbine site.

2.1.4 Mooring

The platform mooring system is primarily designed for station-keeping, but it also provides stability. There are several different available mooring designs, divided into two main categories. The first category, which also is the most commonly used design, is catenary mooring. This model relies on the weight of the mooring line as the restoring force. Steel chains and wires are most commonly used as catenary mooring lines, as steel has a high material density. The anchors are placed at a large radius around the platform, which increases the mooring line length. This anchor is subjected to relatively small loads of horizontal tension, as a section of the mooring line is resting on the seabed. The length of this section varies with the loads subjected onto the floating turbine.

The second category is taut mooring. This design relies on the elasticity of the highly tensioned mooring lines to provide the restoring force. The anchor of a taut mooring line is subjected to both horizontal and vertical forces. This makes it a more complex and expensive setup. Although the anchoring is more costly, the taut model provides some important advantages. It allows for less horizontal and vertical platform translations. Also, the length of mooring line required is significantly reduced, as no section of the line is resting at the seafloor. This also reduces the impact on the seafloor, making the mooring footprint minimal.

2.1.5 Controller

A wind turbine controller is essential for achieving optimal power production over the entire operational spectre of wind speeds. The controller regulates the pitch of the blades. It ensures smooth transitions between increasing or decreasing wind speeds, which is key to maintain platform stability. This is especially important for the platform pitch stability of a floating spar. It also controls the maximum and minimum rotational speed of the rotor. The turbine controller properties of the IEA 15 MW reference turbine are defined in Gaertner et al. [Gaertner et al., 2020b]. This reference turbine is a bottom fixed monopile, which behaves differently compared to a floating structure when subjected to wind loads. Thus, some modifications are necessary when transitioning from a bottom fixed monopile to a floating spar. The modifications done by the WindCrete team is further detailed in subsection 3.4.3.

The controller behaves differently depending on which region of wind speeds the turbine is operating under. The blades are kept stationary for wind speeds less than a minimum value. This minimum wind speed is defined as the cut-in wind speed. Above the cut-in wind speed, the controller ensures maximum power production. The maximum rotational speed is reached at a wind speed defined as the rated wind speed. Optimally, the controller ensures a constant power output, or alternatively constant torque, from the turbine for above rated wind speeds. A constant torque setting is most common for floating wind turbines. This is achieved by the blade pitch controller, which is responsible for continuously regulating the pitch of the three turbine blades. Finally, the controller ensures that the turbine is set to an idling position, if the wind speeds pass a threshold defined as the cut-out wind speed. Turbine production must be stopped for wind speeds above cut-out wind speed, to prevent structural damage.

2.1.6 Rigid body motions

The cartesian global coordinate system for platform motions has its origin in the center of the spar, at the mean sea level (MSL), see Figure 4. The turbine rotor is oriented upwind, and the positive x-axis is pointing downwind. The six translational and rotational degrees of freedom (DoF) are defined along the global coordinate axes. These DoFs are presented in Table 1. The center of rotation does not lie in the global origin, which implies coupling between some translational and rotational motions. This is investigated in Subsection 5.2.

Table 1: Translational and rotational degrees of freedom

| DoF | Symbol | Description |
|-------|----------|------------------------------|
| Surge | η_1 | Translation along the x-axis |
| Sway | η_2 | Translation along the y-axis |
| Heave | η_3 | Translation along the z-axis |
| Roll | η_4 | Rotation around the x-axis |
| Pitch | η_5 | Rotation around the y-axis |
| Yaw | η_6 | Rotation around the z-axis |

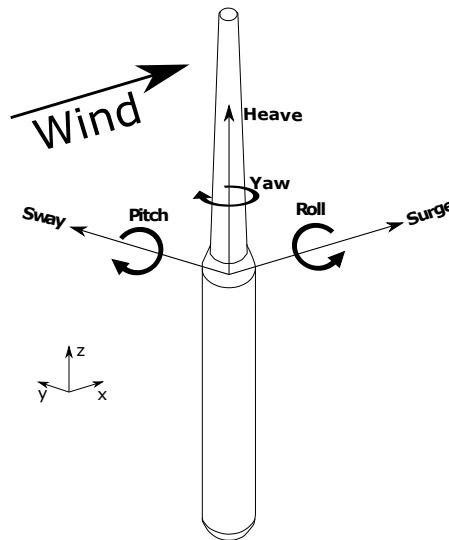


Figure 4: A floating spar platform. Figure adapted from [Mahfouz et al., 2020]

2.2 Idealized Euler-Bernoulli beam

OpenFAST requires tower modes as input. I will find the new tower modes for the adjusted tower using a tool named BModes [Jonkman, 2020]. This tool treats the tower as an idealized Euler-Bernoulli beam. This subsection provides a brief explanation of the underlying theory.

The Idealized Euler-Bernoulli beam model describes how a beam behaves when subjected to bending and axial forces. There are two main underlying assumptions for this model. First, we assume that there is no transverse shear deformation. That is, any straight line through the width of the beam will remain straight after deformation. Second, we assume that the deformation are limited to small angles, so that the slope remains small through the length of the beam. In addition, we assume that the flexural rigidity, EI remains constant through the beam. We may then write a forth-order differential equation for vibration of a uniform beam [Thomson and Dahleh, 2005]:

$$\frac{d^4 y}{dx^4} - \beta^4 y = 0 \quad (2.1)$$

Here, β^4 is defined as:

$$\beta^4 = \rho \frac{\omega^2}{EI} \quad (2.2)$$

where ω is the frequency of vibration and ρ is mass per unit length. Assume a solution on the form $y = e^{ax}$. The natural frequencies of vibration, ω_n are then found to be:

$$\omega_n = \beta_n^2 \sqrt{\frac{EI}{\rho}} \quad (2.3)$$

Where the value β_n is determined by the boundary conditions. BModes models the tower as an idealized Euler-Bernoulli beam cantilevered at its base, and with the RNA as a tip attachment at the free top end. The base is modelled as a rigid body moving according to the properties discussed in subsections 2.3.4 through 2.3.7. These properties set the boundary conditions for the vibrating beam.

2.3 Floater theory and equations

2.3.1 Catenary equations

I use a MATLAB routine created by F. G. Nielsen to approximate a static mooring layout as I do adjustments to the mooring model [Mat, 2021]. This process is further elaborated in section 4.4.3. The MATLAB routine uses elastic catenary equations to calculate positions of segments along a catenary line [Nielsen, 2021].

$$\frac{dx}{ds} = \frac{F_H}{\sqrt{F_H^2 + [F_V - w_0(L - s)]^2}} \quad (2.4a)$$

$$x = \frac{F_H}{w_0} \left\{ \sinh^{-1} \left[\frac{F_V - w_0(L - s)}{F_H} \right] - \sinh^{-1} \left[\frac{F_V - w_0L}{F_H} \right] \right\} + \frac{F_H}{EA} s \quad (2.4b)$$

$$z = \frac{F_H}{w_0} \left\{ \sqrt{1 + \left[\frac{F_V - w_0(L - s)}{F_H} \right]^2} - \sqrt{1 + \left[\frac{F_V}{F_H} \right]^2} \right\} + \frac{1}{EA} \left[F_V s - w_0 L s + \frac{w_0 s^2}{2} \right] \quad (2.4c)$$

Here, F_H is the horizontal force and F_V is the vertical force applied to the upper end. EA is the axial stiffness per unit length, and w_0 is the weight per unit length. The parameter s is the unstretched length coordinate along the line, where the (x, z) position and slope is calculated. L is the unstretched line length so that $s = L$ in the upper end. In the lower end, $s = 0$ and $(x, z) = (0, -D_W)$ where D_W is the water depth.

2.3.2 Moments of inertia

The ElastoDYN submodule (see Subchapter 3.1.1) requires both mass moment of inertia and area moment of inertia of different structure components as input, either directly or indirectly.

Mass moment of inertia

The mass moment of inertia around a rotational axis, I is given as:

$$I = \int_m r^2 dm \quad (2.5)$$

Here, m is mass and r is the polar coordinate of dm . Thus, r^2 would correspond to $(x^2 + y^2 + z^2)$ in the cartesian coordinate system. A significant amount of ballast is added to the subplatform in the reconstruction process. The original subplatform mass moment of inertia around the original subplatform center of mass (CM) is known [Mahfouz et al., 2020, p.17]. I use the parallel axis theorem to add mass moment of inertia contribution from the added ballast in the subplatform interior.

Parallel axis theorem

Suppose the cylinder body of the added ballast with mass m_b has its CM placed in (x_0, y_0, z_0) . The mass moment of inertia around the axes with origin in the added ballast CM is I_{CM} . The mass moment of inertia for this body around some other axes with origin in (x_1, y_1, z_1) , I is given as:

$$I = I_{CM} + m_b d^2 \quad (2.6)$$

where d is the distance along each axis from the added ballast CM to the new axis. In the current work, both the added ballast CM and the platform CM lies on the central z -axis. This means that d equals the vertical distance from the added ballast CM to the subplatform CM for mass moment of inertia around the x - and y -axis, and d equals zero for mass moment of inertia around the z axis (see Equation 2.12).

First moment of area

The first moments of area in cartesian coordinates (S_x, S_y) are defined as:

$$S_x = \int_S y dS \quad (2.7a)$$

$$S_y = \int_S x dS \quad (2.7b)$$

Here, S is a surface area, dS is an elemental surface area and (x, y) is the distance from a given (x, y) -axis to dS .

Second moment of area

The second moment of area (S_{ij}) , also called area moment of inertia, is defined as:

$$S_{ij} = \int_S x_j x_i dS \quad (2.8)$$

Here, subscript (i, j) refers to the cartesian (x, y) coordinates so that $(x_i, x_j) = (x, y)$.

2.3.3 Metacentric height

A floating body in equilibrium is balanced by the buoyancy force and the gravity force. If the body is shifted from its equilibrium, then its ability to restore equilibrium is depending on its stability. The metacentric height, \overline{GM}_c , is a measure of this stability:

$$\overline{GM}_c = \overline{KB} + \overline{BM}_c - \overline{KG} \quad (2.9)$$

where K is the keel, G is the center of gravity, B is the center of buoyancy and M_c is the metacenter. Stability requires a positive metacentric height, and higher metacentric height gives more stability. \overline{BM}_c can be found by the following formula:

$$\overline{BM}_c = \frac{S_{WP}}{V} \quad (2.10)$$

Here, S_{WP} is the second moment of area around the waterplane, see Equation (2.8). V is the displaced volume. A spar platform like the one in focus in this thesis, has a deep draft and relatively small radius. The spar has a low center of gravity due to the ballast contained in the bottom part of the platform. Figure 5 demonstrates how the spar is a very stable platform. This is mainly caused by two factors. The first factor is that the center of buoyancy is far above the center of gravity. The second factor is that the water plane area is relatively small compared to the displaced volume. This means that \overline{BM}_c is small, and the metacentric height is approximately equal to the vertical distance from the center of gravity to the center of buoyancy. This approximation is valid for small angles of rotation.

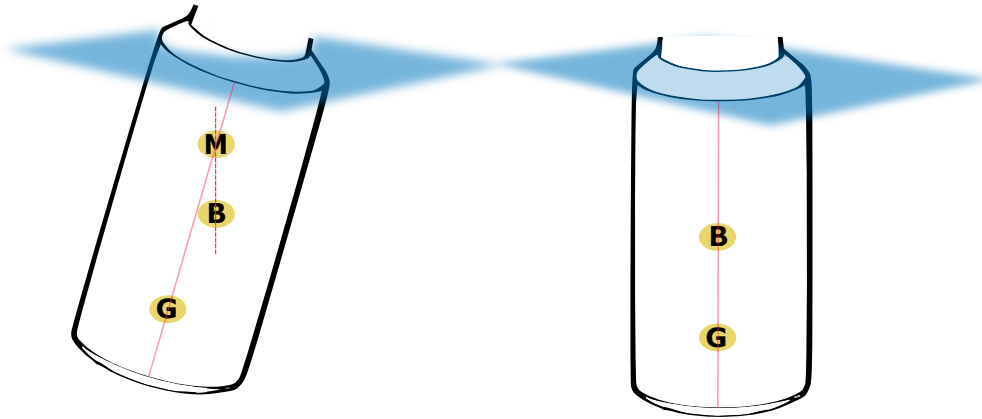


Figure 5: Metacenter of a spar platform. G is the center of gravity, B is the center of buoyancy and M is the metacenter which is referred to as M_c in the previous paragraphs. These models have reduced draft and increased radius, for demonstrational purposes.

2.3.4 Platform inertia matrix

This subsection together with the three following subsections describe matrices that are required as input in BModes. This is further elaborated in Section 3.2.

The equations for mass moments of inertia around each axis with origin in the cylinder-shaped added ballast center of mass (CM) is:

$$\begin{bmatrix} I_x \\ I_y \\ I_z \end{bmatrix} = \begin{bmatrix} \frac{1}{12}m_b(3r^2 + h^2) \\ \frac{1}{12}m_b(3r^2 + h^2) \\ \frac{1}{2}m_br^2 \end{bmatrix} \quad (2.11)$$

Here, m_b is the added ballast mass, and r and h is the radius and height of the cylinder respectively. The mass moment of inertia contribution from added ballast about each cartesian axis with origin in the platform CM becomes:

$$I_{added} = \begin{bmatrix} I_x + m_b d^2 & 0 & 0 \\ 0 & I_y + m_b d^2 & 0 \\ 0 & 0 & I_z \end{bmatrix} \quad (2.12)$$

where d is the distance from the added ballast CM to the platform CM. Finally we derive the new platform mass inertia matrix required as input in BModes:

$$I_{New} = I_{Original} + I_{added} \quad (2.13)$$

where $I_{Original}$ is the platform inertia about the platform CM.

2.3.5 Added mass matrix - strip theory

Consider the spar subplatform as a slender, vertical column of constant radius R . This is a simplification in the case of the WindCrete subplatform, as the subplatform shape is tapered at the top and domed at the bottom. These end effects are not accounted for in the following equations. Let z_t and z_b be the top and bottom extent of the column respectively, where $z_b < z_t \leq 0$. The equation for added mass of linear motion in horizontal direction, A_h is [Nielsen, 2021]:

$$A_h = A^{2D}(z_t - z_b) = \pi\rho_w R^2 C_{ah} L \quad (2.14)$$

Here, $L = z_t - z_b$ is the length of the column, C_{ah} is the two-dimensional added mass coefficient of the column, and ρ_w is sea water density. For oscillation in the vertical direction we get:

$$A_v = (C_{avb} + C_{avt})\pi\rho_w R^3 \quad (2.15)$$

where C_{avt} and C_{avb} is referring to added mass coefficients for the top and bottom of the column respectively. $C_{avt} = 0$ if the structure is piercing the free surface. The added mass matrix for linear motions, \mathbf{A}_c is then given as:

$$\mathbf{A}_c = \begin{bmatrix} A^{(2D)}L & 0 & 0 \\ 0 & A^{(2D)}L & 0 \\ 0 & 0 & A_v \end{bmatrix} \quad (2.16)$$

This matrix corresponds to the top left corner of the 6×6 added mass matrix. The lower left corner of the added mass matrix is the rotational terms, where the two non-zero terms of the sub-matrix \mathbf{I} are:

$$I_{11} = \int_L (y^2 + z^2) dm = y_c^2 A_v + \frac{1}{3} A^{(2D)} (z_t^3 - z_b^3) \quad (2.17)$$

$$I_{22} = \int_L (x^2 + z^2) dm = x_c^2 A_v + \frac{1}{3} A^{(2D)} (z_t^3 - z_b^3) \quad (2.18)$$

Here, (x_c, y_c) are the x and y coordinate respectively of the central axis of the column. If the equations are applied to a structure that is symmetric about the z-axis, we would have that $(x_c, y_c) = (0,0)$. Next, let \mathbf{S}_c be defined as:

$$\mathbf{S}_c = \begin{bmatrix} 0 & -\frac{1}{2}(z_b + z_t) & y_c \\ \frac{1}{2}(z_b + z_t) & 0 & -x_c \\ -y_c & x_c & 0 \end{bmatrix} \quad (2.19)$$

and let $\mathbf{S}_{Ac} = \mathbf{A}_c \mathbf{S}_c$. The full added mass matrix is then:

$$\mathbf{A}_{col} = \begin{bmatrix} \mathbf{A}_c & -\mathbf{S}_{Ac} \\ \mathbf{S}_{Ac} & \mathbf{I} \end{bmatrix} \quad (2.20)$$

2.3.6 Hydrostatic stiffness matrix

Assume that the hydrostatic forces are linear. The hydrostatic stiffness matrix for a floating body, \mathbf{C}_h is then given as [Veritas, 2010]:

$$\mathbf{C}_h = \begin{bmatrix} 0 & 0 & 0 & 0 & 0 & 0 \\ 0 & 0 & 0 & 0 & 0 & 0 \\ 0 & 0 & \rho_w g S & \rho_w g S_2 & -\rho_w g S_1 & 0 \\ 0 & 0 & \rho_w g S_2 & \rho_w g (S_{22} + V z_B) - M g z_G & -\rho_w g S_{12} & -\rho_w g V x_B + M g x_G \\ 0 & 0 & -\rho_w g S_1 & -\rho_w g S_{12} & \rho_w g (S_{11} + V z_B) - M g z_G & -\rho_w g V y_B + M g y_G \\ 0 & 0 & 0 & -\rho_w g V x_B + M g x_G & -\rho_w g V y_B + M g y_G & 0 \end{bmatrix} \quad (2.21)$$

Here, M is the total mass of the whole system. This includes the platform, ballast, tower and RNA. V is the submerged volume. The center of gravity is in (x_G, y_G, z_G) , and the center of buoyancy is in (x_B, y_B, z_B) . S is the water plane area. S_i and S_{ij} are the first and second moments of water plane area respectively. Finally, g is the gravitational constant.

2.3.7 Mooring stiffness matrix

Assume a catenary line stretching in the local (x,z) plane, with its origin in the upper end. The restoring coefficients, C_{ij} that make up the 3×3 restoring matrix for each catenary line, $\mathbf{C}^{(l)}$ are defined as [Nielsen, 2021]:

$$\mathbf{C}^{(l)} = C_{ij} = \frac{\partial F_i}{\partial j}, \quad i, j = [x, y, z] \quad (2.22)$$

The local plane is rotated around the vertical z -axis with an angle θ relative to the global coordinate system. The 3×3 restoring force matrix in the global coordinate system is then:

$$\mathbf{C} = \boldsymbol{\gamma}^T \mathbf{C}^{(l)} \boldsymbol{\gamma} \quad (2.23)$$

where the transformation matrix is:

$$\boldsymbol{\gamma} = \begin{bmatrix} \cos(\theta) & \sin(\theta) & 0 \\ -\sin(\theta) & \cos(\theta) & 0 \\ 0 & 0 & 1 \end{bmatrix} \quad (2.24)$$

If the catenary line is attached to the subplatform at (x_t, y_t, z_t) in the global coordinate system, the 6×6 mooring stiffness matrix can be written as:

$$\mathbf{C}^{(m)} = \begin{bmatrix} \mathbf{C} & \mathbf{C}\boldsymbol{\alpha} \\ \boldsymbol{\alpha}^T \mathbf{C} & \boldsymbol{\alpha}^T \mathbf{C}\boldsymbol{\alpha} \end{bmatrix} \quad (2.25)$$

where α is:

$$\alpha = \begin{bmatrix} 0 & z_t & -y_t \\ -z_t & 0 & x_t \\ y_t & -x_t & 0 \end{bmatrix} \quad (2.26)$$

2.3.8 Morison's equation

The Morison's equation gives the in-line hydrodynamic force acting on a cylinder as a sum of inertial and drag forces [Fredsoe and Sumer, 2006]. Assume that the cylinder diameter is less than 0.2 times the wave length, to ensure small variation in flow acceleration over the cross-section of the body. Assume that the ratio of wave height over wave length is less than 0.14, to avoid slamming from breaking waves. The total force, F_T , is given as:

$$F_T = F_D + F_I = \frac{1}{2}\rho_w D C_d |U|U + \rho_w C_M A \frac{dU}{dt} \quad (2.27)$$

The first term is the drag force, F_D . This is proportional to $|U|U$, which is the flow velocity squared. The second term is the inertia force, F_I . This force is in phase with flow acceleration, which is shifted 90° relative to the phase of the flow velocity and drag force. A is the cross-sectional area of the cylinder, and D is the cylinder diameter. C_d and C_M are the drag and mass coefficients respectively. C_M is equal to the added mass coefficient plus 1. U is the flow velocity.

2.4 Wave and wind fields

OpenFAST allows several types of user-defined wave- and wind fields as inputs. I perform simulations with both still water and with wave input. I also do simulations with both uniform and turbulent wind. The following paragraphs give a brief description of these inputs and how they are generated. I use turbulent wave and wind fields as means to test the model as I do adjustments.

2.4.1 JONSWAP spectrum

The JONSWAP spectrum, [Hasselmann et al., 1973], has its name from the Joint North Sea Wave Project. Analysis of the collected data found that the wave spectrum continues to develop over very long times and distances. This resulted in a proposed wave spectrum for a developing sea state, named the JONSWAP spectrum. The underlying equations can be found in DNV-RP-C205 [Veritas, 2010, p. 33]. However, these equations are an integrated part of the hydrodynamic submodule, and so I choose not to go into details in this thesis. Three input parameters are required when running simulations with a JONSWAP wave spectrum. The first required parameter is the significant wave height, H_s , which is defined as the mean of the one-third highest waves. The second required parameter is the peak period, T_p , which is the wave period corresponding to the peak frequency of the spectrum. The third required parameter is a peak-shape parameter, which is a non-dimensional value in the range of [1,5], and with an average value of 3.3. This parameter is set to "Default" in the hydrodynamic submodule.

2.4.2 Turbulent wind field

I use a tool developed by DTU Wind Energy named Mann 64bit turbulence generator to create three-dimensional boxes of turbulent fluctuations [HAWC2].

The Mann spectral tensor model

The Mann 64bit turbulence generator creates a 3D wind box by the use of the Mann spectral tensor model. This model is developed by Jacob Mann, and is a model for representing a turbulent wind field [Mann, 1994]. It is one of the turbulence models recommended to be used by the International Electrotechnical Commission (IEC) [IEC 61400-1]. Table 2 defines required input parameters. This includes three "Mann-parameters"; an eddy lengthscale (l), a constant connected to eddy lifetimes (Γ) and a parameter describing energy dissipation of eddies ($\epsilon\alpha^{\frac{2}{3}}$).

Table 2: Mann turbulent wind field simulation parameters

| Parameter description | Simulation parameter |
|--|--|
| Grid points in the x-direction | $N_x = 32768$ |
| Grid points in the y-direction | $N_y = 64$ |
| Grid points in the z-direction | $N_z = 64$ |
| Distance between grid points x-direction | D_x , Equation (2.28) |
| Distance between grid points y-direction | $D_y = 4.2$ |
| Distance between grid points z-direction | $D_z = 4.2$ |
| The length scale of the turbulent eddies (l) | 33.6 |
| Non-dimensional parameter for eddy lifetime (Γ) | 3.9 |
| Dissipation rate of eddies | $\epsilon\alpha^{\frac{2}{3}}$, Equation (2.29) |

The 3D box of turbulent fluctuations is advected past the turbine following the mean wind, assuming Taylors frozen turbulence, see the following paragraph. The distance between grid points in x-direction must be large enough to cover the whole time series. This distance is found by the following formula:

$$D_x = \frac{\overline{U_x} \cdot T}{N_x} \quad (2.28)$$

where $\overline{U_x}$ is the mean wind speed at hub height, and T is the simulation time. As both simulation time and number of grid points in the x-direction is kept constant for all simulations, the mean wind speed dictates the value of D_x .

$\epsilon\alpha^{\frac{2}{3}}$ is a parameter describing the energy dissipation of eddies. This dissipation rate is dependent on turbulence intensity, according to equation (2.29).

$$\epsilon\alpha^{\frac{2}{3}} = \frac{55}{18} \cdot 0.4754 \cdot \sigma_{iso}^2 \cdot l^{-\frac{2}{3}} \quad (2.29)$$

Here, σ_{iso} is given as:

$$\sigma_{iso} = 0.55\sigma_x \quad (2.30)$$

where σ_x is the standard deviation of the wind time series, or the root-mean-square of the turbulent fluctuations. Given a turbulence intensity (T_i), we have:

$$\sigma_x = T_i \overline{U_x} \quad (2.31)$$

Thus this parameter is also dependent on the wind speed used. The values of l and Γ are used according to the IEC standard [IEC 61400-1].

Taylor's Hypothesis

Observations show that turbulent eddies often evolves with a longer timescale compared to the time it takes to advect past a point in space. Taylor's hypothesis assumes that the turbulent structure is frozen as advection carries it past a reference point [Stull, 1988]:

$$\frac{D\xi}{Dt} = 0 \quad (2.32)$$

where ξ is any variable. We get the general form of Taylor's hypothesis by extending the material derivative above:

$$\frac{\partial \xi}{\partial t} = -U \frac{\partial \xi}{\partial x} - V \frac{\partial \xi}{\partial y} - W \frac{\partial \xi}{\partial z} \quad (2.33)$$

[U,V,W] are the mean wind components in the [x,y,z] direction. Taylor's hypothesis is applicable for situations where turbulence intensity is small compared to the mean wind speed.

3 BACKGROUND, TOOLS AND SITE CONDITIONS

In the following chapter, I introduce the simulation software used, as well as both the IEA reference turbine model and the CoreWind model. I also give brief descriptions of the sites in focus for this thesis. The introduction of the simulation software and its submodules introduces many new concepts that are not explained in detail. The objective of this thesis is partly to familiarize with OpenFAST from a user point of view. This requires some overall knowledge of the main components of the software, and detailed theory is not the priority. The focus of this chapter is to get an overview of the software, and the lessons learned in the process of using the software. The theory used in this thesis is presented in Chapter 2.

3.1 OpenFAST

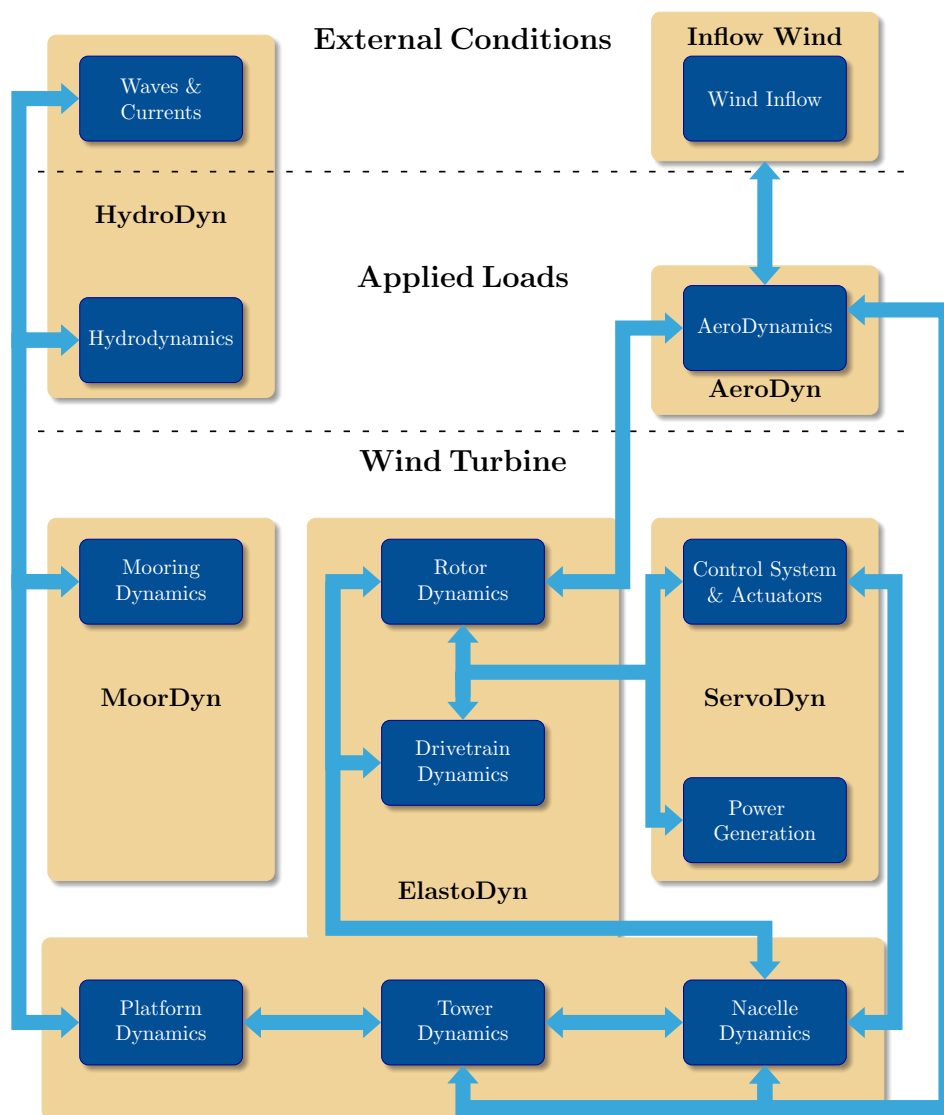


Figure 6: A flowchart of the OpenFAST structure, adapted from [NREL, 2020a, p.72]

OpenFAST is a powerful tool for simulating the dynamics of a wide range of wind turbine configurations [OpenFAST binaries]. Figure 6 shows a flowchart of the OpenFAST structure. The OpenFAST framework combines submodules for turbine aerodynamics, control systems, structural dynamics, and hydrodynamics. All submodules are highly adaptable through input selection, and the software is open-sourced. OpenFAST is developed and maintained by the National Renewable Energy Lab (NREL), which is a national laboratory of the U.S. Department of Energy.

OpenFAST is available on Windows, macOS and Linux. Personally, I use Windows. In this case, compiling from source is not necessary. All necessary complementary software and the WindCreate model used in this thesis are all freely available. Specifics are given in the list below:

- OpenFAST version 2.5.0 [OpenFAST binaries] including the ROSCO v2.0.1 controller [NREL, 2020b]
- Fortran compiler [Intel Fortran Compiler]
- WindCreate model input files [Molins et al., 2020]

Further, API changes between OpenFAST versions are described in [API changes]. I manually updated input files from OpenFAST version 2.4.0 to be compatible with OpenFAST 2.5.0, which is the version used in this thesis.

3.1.1 Sub-modules

Short descriptions of the sub-modules most relevant to this thesis follows below. More information is found in the OpenFAST documentation. [NREL, 2020a].

AeroDyn

AeroDyn is a time-domain module for simulating the aerodynamics of a horizontal-axis wind turbine [NREL, 2020a, Ch 4.3]. This submodule approximates aerodynamic loads on each blade and on the tower using an actuator line method. This method represents the blades and the tower using point nodes oriented along lines following the structures. The AeroDyn module receives the position, orientation, and velocity of each node continuously from the OpenFAST framework. The lift and drag forces, as well as the 2D distributed load is then calculated for each node in each time step. These distributed loads are integrated over the length of the structure to find the total 3D aerodynamic loads. AeroDyn can be split into four separate submodels. The first models rotor wake/induction. The second calculates blade airfoil aerodynamics. The third models the tower influence on the fluid local to the blade nodes. The fourth submodel calculates tower drag.

AeroDyn requires several input files. General environmental conditions including air density, kinematic air viscosity and the speed of sound is specified in the main input file. The tower radius and drag coefficient at each tower node height is also specified here. The blade geometry is defined separately. First, the local span of each blade node is defined, with increasing distance from the hub. Second, factors such as local out-of-plane offsets, twist angle and chord length are defined for each node along the local span. The next input file contains airfoil information. This includes airfoil angle of attack, lift, drag

and coefficients for moment and pressure.

BeamDyn

BeamDyn is a time-domain module that calculates structural dynamics of slender structures [NREL, 2020a, Ch 4.6]. This module is used in the OpenFAST framework to model blade structural dynamics. The root node of the blade receives input at each time step, governed by The OpenFAST driver. The inputs are the six translational and rotational displacements, six velocities and six accelerations. The outputs at the root node are six reaction loads, consisting of the moments and three translational forces. In addition, BeamDyn outputs blade velocities, accelerations, and displacements along the beam length. These outputs are then used by AeroDyn to calculate aerodynamic loads along the blade length, which again is used as input in BeamDyn for the next time step.

ElastoDyn

ElastoDyn is a structural-dynamic module for horizontal-axis wind turbines [NREL, 2020a, Ch 4.8]. ElastoDyn contains structural geometries and modelling options of the RNA, tower and subplatform. The primary input file allows the user to specify initial conditions for both platform displacements and blade orientations. This makes it possible to drastically reduce the start-up transients in simulations, which might reduce required simulation lengths. There are 17 degrees of freedom which can be enabled or disabled separately. This can be very convenient for debugging, or for testing specific model characteristics. The main input file also contains a turbine configuration input section, where the user can specify dimensions, number of blades, and mass centers of several geometry elements. Mass and inertias of the RNA and platform are also required as input. The second ElastoDyn input file contains distributed tower properties, as well as tower fore-aft and side-to-side mode shapes in forms of 6th order polynomials. These modes are found externally using BModes in this thesis, see Chapter 3.2.

ServoDyn

The ServoDyn submodule is responsible for the mechanical control of the system [NREL, 2020a, Ch 4.11]. Here you find input for controlling blade pitch, the generator and the nacelle-yaw control. This submodule requires two input files describing the wind turbine controller. These files are provided within the WindCrete model [Molins et al., 2020]. Here they have adapted a baseline ROSCO controller originally developed for an onshore wind turbine. The controller is crucial to ensure stability as the floating wind turbine is subjected to loads from waves and turbulent wind.

The WindCrete model provides a version of the first NREL Reference OpenSource Controller (ROSCO), which uses a Bladed-style DISCON interface. I was unable to run this setup, even after attempting installation on three separate hardware. Thus, I had to adapt the input files of another ROSCO version 2.0.1 controller to fit my purpose [NREL, 2020b]. This extra step should not be required for a standard installation. I verified the new controller by comparing outputs from WindCrete model simulations done by a colleague, with my own outputs. I was able to reproduce the same output using identical inputs.

HydroDyn

The HydroDyn submodule models the hydrodynamics of the system, and can be used as a standalone model [NREL, 2020a, Ch 4.9]. Here we specify the hydrodynamic model parameters together with substructure geometry and properties. HydroDyn supports several incident wave kinematics models, including JONSWAP/Pierson-Moskowitz spectrum and externally generated wave-elevation time series.

The submodule supports a potential flow model to calculate hydrodynamic forces. This requires potential-flow solutions generated externally by programs such as ANSYS-AQWA [Ansys 2021] or WAMIT [WAMIT 2021]. HydroDyn requires input files following the WAMIT output format. HydroDyn also supports a strip-theory-only approach. This approach uses Morison's equation, and it requires definition of one or more strip-theory members in the input file. The strip-theory approach gives the possibility to include contributions from current-induced water velocity, as the current only induce hydrodynamic loads through the viscous drag terms of strip-theory members. Each strip-theory member can be flagged to determine if the potential-flow model or Morison's equation should be applied. This gives the possibility for a hybrid approach.

MoorDyn

The MoorDyn submodule is the mooring line model connected to OpenFAST [MoorDyn 2021]. It uses a lumped-mass approach to calculate cable dynamics. The cable is modelled as nodes with evenly spaced line segments between them. Hydrodynamic loads are calculated at each node point. The node positions and node types are specified in the main input file. There are three different kinds of node types. A fixed node is not allowed to move in space, which accurately represents an anchor point. A vessel node is attached to the platform substructure, and the node movements are governed by subplatform motions. The connect nodes move in space governed by the forces acting on them. A connect node might join two line segments with different structural properties, allowing for hybrid mooring lines that combines elastic and inelastic lines.

Inflow Wind

The Inflow Wind submodule handles the input wind field, and can be used as a standalone model [NREL, 2020a, Ch 4.10]. Parameters for steady wind conditions are specified in the main input file. The submodule also allows externally generated synthetic wind fields of different formats. I use binary HAWC-format files created by an external pre-processing tool developed for the HAWC2 code by DTU Wind Energy [HAWC2]. This tool is named the Mann turbulence generator, see Section 2.4.2. This tool gives three output files containing grids of turbulent fluctuations in [u,v,w] directions separately. The grid translates with the mean wind along the x-axis during simulation. Taylor's hypothesis is assumed applicable. The grid numbers and distances between grid points are also specified in the Inflow Wind input file, to match the grid of the wind files from the Mann turbulence generator.

3.2 BModes

OpenFAST requires fore-aft and side-to-side tower modes as input. Due to the tower modifications performed in the current work, these tower modes have changed, and so they must be recalculated. Also, the tower mode natural frequencies are of interest, as the rotating blades interact with the tower. A software named BModes was developed primarily to find these modes, and their associated natural frequencies. The software is developed by Gunjit S. Bir of the National Renewable Energy Laboratory (NREL) [Bir, 2007]. BModes calculates coupled modes for a beam using a finite-element method (FEM). The software was originally developed for fixed foundations. I use a version that can be used for floating wind turbines [Jonkman, 2020]. This version was never completed, as the developer Gunjit Bir left NREL. Thus, this version is not well documented, and has never been officially released.

3.2.1 Basic principles

The tower is modelled as a Euler-Bernoulli beam divided into finite elements. BModes uses Hamilton's principle to derive PDEs of motion for the modelled tower. These equations are discretized through finite element analysis to give us solvable ODEs in time. Eigenanalysis of these equations produces the coupled modes of the tower, together with the mode frequencies. A coupled mode implies presence of coupled flexural, axial, and torsion motions in a natural mode of vibration. The code allows for tip attachments. The tower is cantilevered at its base, connected to a rigid body, which represents the floating platform. This rigid body is associated with mass moment of inertia, added mass, hydrostatic stiffness, and mooring stiffness matrices, which are required as input. These inputs are investigated in Section 4.5.1.

3.3 IEA 15-MW offshore reference wind turbine

The IEA 15-MW offshore reference wind turbine is described in IEA Wind Technology Collaboration Programme (TCP) Task 37 [Gaertner et al., 2020b]. The development of this project is a collaboration involving the National Renewable Energy Laboratory (NREL), the Technical University of Denmark (DTU) and the University of Maine (UMaine). This is a bottom-fixed design with a monopole base. It is a conventional three-bladed wind turbine, with the rotor plane facing in the upwind direction. The hub height is set to 150 m above MSL, with the rotor spanning a diameter of 240 m. The baseline model presented here is a steel structure, designed to be placed offshore at water depths of 30 m. The diameter of the tower foundation is 10 m, which is pushing the current manufacturing and installation abilities. Pushing the boundaries of the current wind turbine technology is one of the important roles of reference wind turbines. The RNA design is standard and highly adaptable, while the tower and support platform require a more site specific design. Key parameters of the reference turbine RNA are presented in Table 3.

Further, a reference wind turbine is an open-sourced benchmark with a realistic, but not optimized design. This makes it a great platform for students that wish to enter and explore the world of wind turbine technology. The model is made available through provided input files for a range of analysis tools, hosted at the IEA Wind Task 37 GitHub repository [IEA, 2020]. These are provided with the motivation of facilitating further collaboration in the wind energy community. One such collaboration is the EU-funded CoreWind project. This project is investigated in the next section.

Table 3: **Key parameters, Reference Turbine RNA**
Adapted from [Gaertner et al., 2020b]

| Parameter | Units | Value |
|-----------------------------|-------|--------------|
| Power rating | MW | 15 |
| Rated thrust | MN | 2.4 |
| Turbine class | - | IEC Class 1B |
| Cut-in wind speed | m/s | 3 |
| Rated wind speed | m/s | 10.59 |
| Cut-out wind speed | m/s | 25 |
| Rotor diameter | m | 240 |
| Hub height | m | 150 |
| Hub overhang | m | 11.35 |
| Rotor precone angle | deg | -4.0 |
| Blade prebend | m | 4 |
| Blade mass | t | 65 |
| Shaft tilt angle | deg | 6 |
| Rotor nacelle assembly mass | t | 1017 |

Table 3 lists some key parameters of the IEA 15MW reference turbine RNA. All parameters presented here remains unaltered in both the WindCrete model and the adjusted model.

3.4 CoreWind WindCrete Floating Wind Turbine

The CoreWind project aims to reduce the Levelized Cost of Energy (LCOE) for offshore wind turbines, with a special focus on floating technologies [CoreWind, 2021]. CoreWind has developed two floating turbine platforms designed to support the IEA 15 MW reference wind turbine, one of which is a spar design. A floating substructure will significantly alter the accelerations experienced by the tower, and the natural frequencies of the tower. Therefore, the tower structure is also optimized by CoreWind, with a stiffer design. CoreWind achieves this by both increasing the tower radius and decreasing the tower height, compared to the reference tower. I will focus on the spar platform project, which is named WindCrete [Mahfouz et al., 2020]. Figure 7 illustrates the WindCrete tower and substructure, with dimensions.

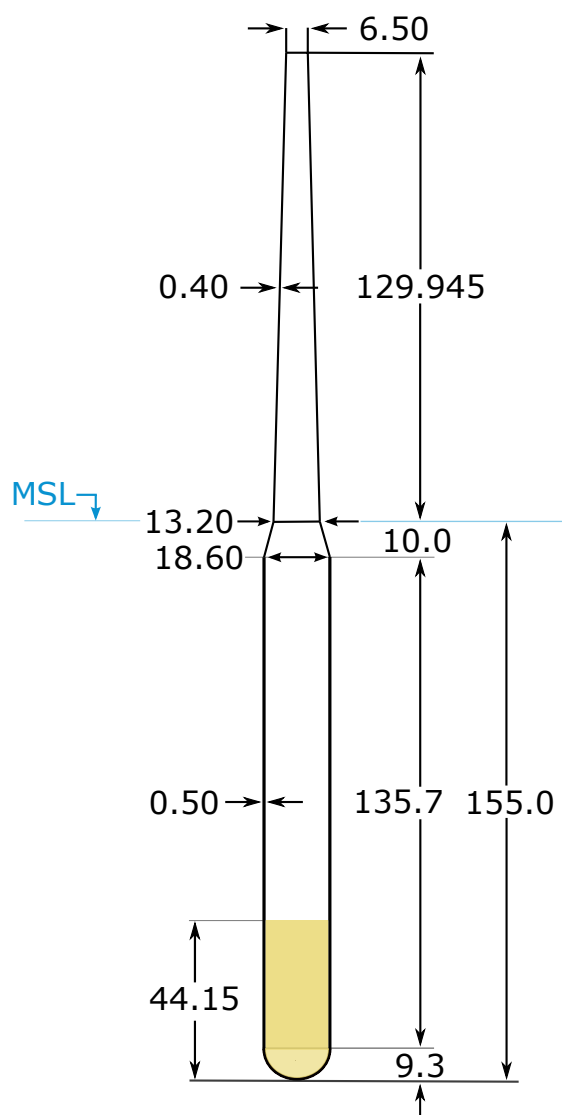


Figure 7: The WindCrete spar floater. Adapted from [Mahfouz et al., 2020]

3.4.1 The WindCrete model

The WindCrete model is a spar platform made of concrete [Mahfouz et al., 2020]. The model is designed to fit the environmental conditions of a Gran Canaria site. The tapered tower has a constant wall thickness of 0.4 m. The design choice of a concrete tower is an effort to reduce cost, compared to the steel tower used in the IEA reference turbine [Gaertner et al., 2020b]. In the OpenFAST model, the tower base is set to 15 m even though the design report states that the tower base is defined at the MSL [Mahfouz et al., 2020, p.13]. This is done in order to preserve the base height as it is defined in the IEA 15MW reference wind turbine OpenFAST model. When doing adjustments, I will keep the same definition as both mentioned models, for the sake of consistency. Some key properties of the WindCrete model are presented in Table 4.

The design basis for the WindCrete model specifies that applying maximum thrust force on the turbine should give a static platform pitch of less than four degrees. Further, the natural periods of oscillation for platform heave, pitch, and roll should be kept above 30 s. I keep these characteristics as a design basis when adjusting the WindCrete model. Natural periods of rotational and translational platform DoFs are discussed in Section 5.2.

Table 4: WindCrete Properties

| Property | Unit | Value |
|----------------------------|---------------------|------------|
| Total mass | [kg] | 3.9805e+07 |
| Tower mass | [kg] | 3.2550e+06 |
| Draft | [m] | -155.00 |
| Center of Mass (CM) Height | [m] | -98.41 |
| Ixx from CM | [kgm ²] | 1.5536e+11 |
| Iyy from CM | [kgm ²] | 1.5536e+11 |
| Izz from CM | [kgm ²] | 1.9025e+09 |
| Displacement | [m ³] | 4.054e+04 |
| Center of Buoyancy Height | [m] | -77.29 |

3.4.2 The WindCrete support platform

The subplatform has a draft of 155 m, with a tapered top and a domed bottom. The main cylinder structure has a radius of 9.3 m, with 0.5 m thick concrete walls. Solid aggregate ballast with a density of 2500 kg/m³ is housed in the lower part of the cylinder interior. The mooring fairleads are located at a depth of 90 m. Some key properties of the WindCrete subplatform model are presented in Table 5. Note that as the tower base is defined at a height of 15 m, the total mass of the substructure includes the tower section from the MSL to 15 m.

Table 5: WindCrete substructure properties

| Property | Unit | Value |
|----------------------------|---------------------|-----------|
| Total mass | [kg] | 3.655e+07 |
| Concrete mass | [kg] | 1.148e+07 |
| Ballast mass | [kg] | 2.507e+07 |
| Center of Mass (CM) Height | [m] | -113.08 |
| Ixx from WindCrete | | |
| substructure CM | [kgm ²] | 5.590e+10 |
| Iyy from WindCrete | | |
| substructure CM | [kgm ²] | 5.590e+10 |
| Izz from WindCrete | | |
| substructure CM | [kgm ²] | 1.828e+09 |

3.4.3 WindCrete controller

The WindCrete design utilizes a controller developed for the NREL 5MW and the DTU 10 MW reference wind turbines [NREL, 2021] (v1.0.0). This controller is then tuned to achieve stability at above-rated wind speeds for the 15 MW WindCrete version. The rotational speed is controlled to be a minimum of 5 rpm at the cut-in wind speed of 3m/s, and a maximum of 7.56 rpm at the rated wind speed of 10.59 m/s. For wind speeds within these limits, variable-speed torque control is used to get maximum power output. There is no blade pitch regulation involved until the rated wind speed is reached. Constant torque control is used between rated wind speed and the cut-out wind speed of 25.0 m/s. A consequence of this is some variation in the power output, especially when the wind speed is decreasing. In this region of wind speeds, all three turbine blades are uniformly pitched, with no individual variation. This is known as collective pitch control.

The rotational speeds under production imply a 1P frequency range of [0.0833 to 0.126] Hz and a 3P frequency of [0.25 to 0.378] Hz. This is the frequency of the blades passing a point in their rotational plane. As an example, the blades will pass the tower at frequencies within the ranges defined above. It is important to consider the 1P and 3P frequency when designing the tower, to avoid unwanted resonance. The 1P and 3P frequency ranges are discussed further in Section 4.3.1.

3.5 Site descriptions

The following paragraphs provides a short description of the sites in focus of this thesis.

3.5.1 Environmental conditions in wind turbine design

The RNAs of wind turbines are not only designed for specific power outputs, but also for specific environmental conditions. Wind turbines are classified after basic parameters such as average wind speeds, maximum wind speeds, and turbulence intensity. The offshore wind industry may then buy an RNA that has a classification that suits the site and project in question. For example, if a wind turbine is to be placed in a wind park near other wind turbines, one would expect the neighboring wind turbines to generate turbulence that affects the incoming wind field. Thus, one would need to use an RNA with a higher turbulence category than if the wind turbine was placed without surrounding wind turbines. Though the RNA follows a standard, the tower, support platform, and mooring or foundation is designed for specific sites.

The WindCrete concept has a design based on the IEA 15 MW reference turbine, with some identical structures, mainly the RNA. This wind turbine is classified as IEC Class 1B, after guidelines provided in the IEC standard [IEC TS 61400-3-2:2019]. In this classification, the number 1 refers to high winds, and the letter B refers to medium turbulence intensity. I do no changes to the RNA when adjusting the WindCrete model.

Though the WindCrete RNA is similar to the IEA 15 MW reference turbine, the tower and support platform have to be adapted to account for the floating spar design. Recall, the reference design defines a bottom-fixed monopile platform. We have to consider the change of dynamic loads experienced by the tower and support platform when transitioning to a floating design. Both normal and extreme environmental conditions must be considered. Important factors to consider are both the normal and extreme 10-minute average wind speeds, as well as the significant wave heights (H_s). These considerations must also be done when adjusting the WindCrete model to fit new environmental conditions, as done in the current work.

3.5.2 Gran Canaria Island

The WindCrete project places a floating spar wind turbine off the southeast coast of Gran Canaria Island. The site information presented here is obtained from the Design Basis report by COREWIND [Vigara et al., 2020]. The water depth is set to 200 m. The 10-minute mean wind speed at a height of 100 m is 11.98 m/s. This value is found by using the logarithmic law to extrapolate from the measurement height of 10 m. The 10-minute mean extreme wind speed profile with a 50 years return period (TR_{50}) gives a wind speed of 27.35 m/s at a height of 100 m. The site has winds coming predominantly from the north-northeast.

The most probable H_s is 1.5 m. For a 50-year return period, the H_s increases to 5.11 m, with a frequency of 9.0-11.0 s. The dominant wave direction is from the north-northeast, following the dominant direction of the wind. There is a vertical difference of 3.32 m between the highest and lowest still water levels.

3.5.3 Utsira

As mentioned in the introduction of this thesis, the Utsira site has an area of 1010 km², with an estimated floating wind turbine capacity of up to 1500 MW [Drivenes et al., 2010]. Water depths vary between 185-280 m, with an average depth of 267 m within the site. The average H_s is 2.2 m. The 50-year return period H_s is 13.8 m, which is drastically larger compared to the Gran Canaria site. The average wind speed at a height of 100 m above MSL is 10.2 m/s [Skeie et al., 2012]. The 10-minute 50-year return rate (TR_{50}) wind speed is 42.1 m/s at the same height above MSL. The dominant wind direction follows the coast from north to south or from south to north.

4 UTSIRA DESIGN

This chapter describes the iterative process of adjusting the WindCrete OpenFAST model to the Utsira site. I discuss structural requirements, and present new input parameters.

4.1 Motivation

I aim to model a spar floating wind turbine to fit the environmental conditions of the Utsira site, using the WindCrete model as a baseline. The turbine must be designed to withstand the harsher conditions off the western coast of Norway. For this reason, the hub height must be increased. This process must be done according to a range of structural requirements, to ensure integrity. This process will be discussed in the following subchapters.

4.2 Adjustment process

The adjustment process can be viewed as four main steps. The first step is to restructure the tower, to account for more extreme environmental conditions. The second step is to adjust the ballast in the support structure, with the aim of keeping the displaced volume of the platform close to the original. The third step is to adjust the mooring layout to a new water depth, which again will require some adjustment of the subplatform ballast. The fourth step is to calculate the tower modes, to ensure that these natural frequencies lie outside the 3P frequency range, with a certain margin. Figure 8 shows a flowchart of the adjustment process. All the steps are iterative, and I have done several iterations of the whole process in this work. The following sections elaborate on the adjustment process.

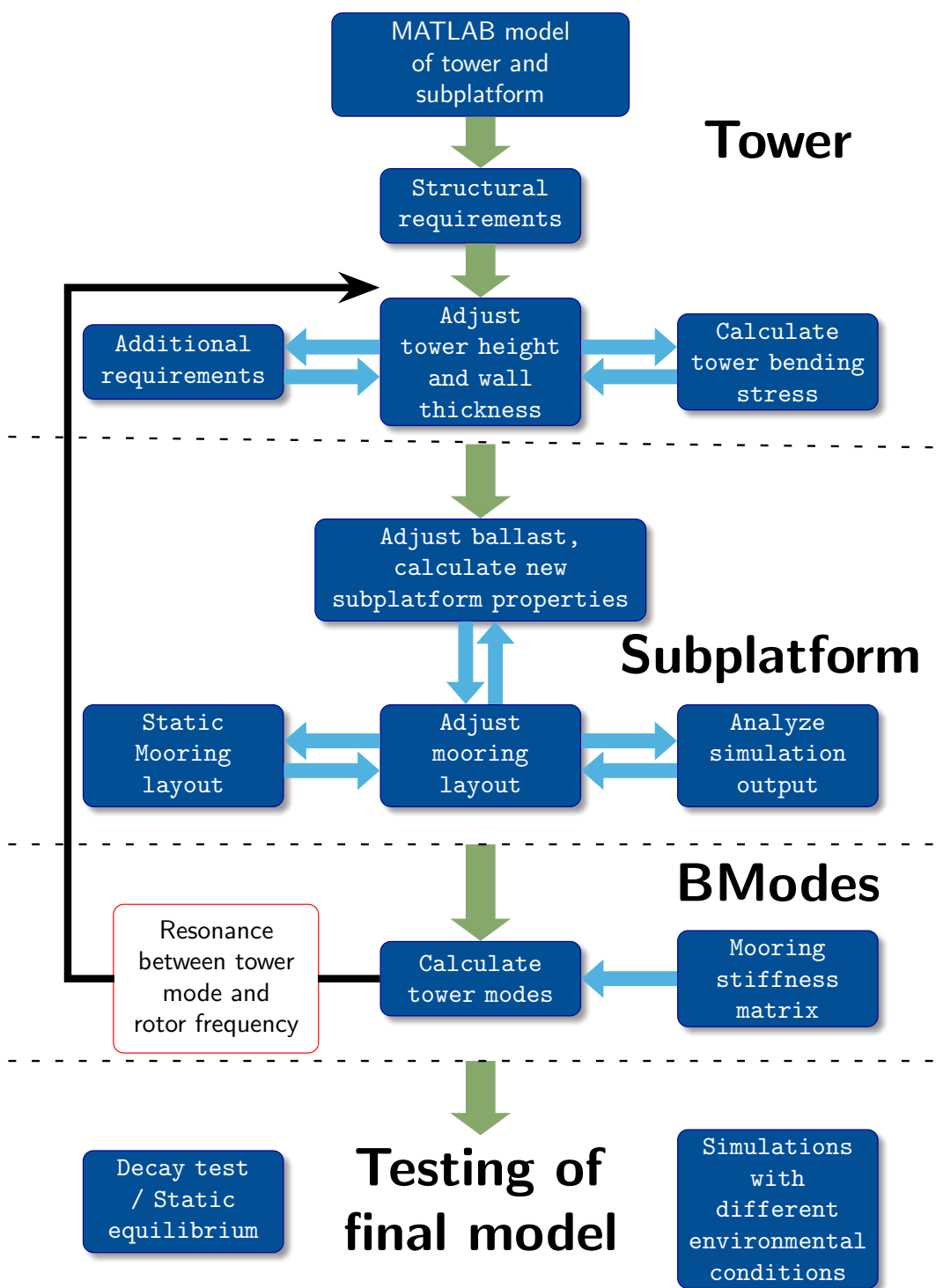


Figure 8: A flowchart of the main steps in adjusting the WindCrete OpenFAST model to fit the Utsira site.

4.2.1 Structural requirements

The Utsira structure must satisfy the structural requirements given by the IEC TS 61400-3-2:2019 standard [IEC TS 61400-3-2:2019]. The standard specifies that:

1. Access platform to be out of the reach of the 50-years wave crest
2. Minimum air gap of 20% of H_s or 1.50 meters, whichever is larger
3. Hub height to be 6 meters plus the semi-rotor diameter. The 6 meters allowance is for an operating crane located at the access platform.

The 50-years significant wave height ($H_{s,50}$) for the Utsira site is reported to lie between 13.8 m and 12.8 m depending on source [Skeie et al., 2012] [Drivenes et al., 2010], with the highest values measured at the western border of the site. H_{\max} is derived from the significant wave height ($H_{s,50}$), which again is a statistical property of a wave data time series. Given the Rayleigh density distribution of the wave data, H_{\max} can be calculated. H_{\max} is interpreted as the most probable largest wave height for the given $H_{s,50}$. Assume a typical wave period of 10 seconds. Also assume that the wave spectrum does not contain breaking waves, which limits the maximum wave height to 0.78 times the water depth. This is no issue for the Utsira site, as water depths exceeds 200 meters. Equation (4.1) then gives the most probable largest wave height given a H_s [Bai and Bai, 2014]:

$$H_{\max} \cong 1.86H_{s,50} \quad (4.1)$$

I will use the most extreme value of ($H_{s,50} = 13.8$ m) in my calculations. This is the height between the wave crest and the wave trough. H_{\max} is multiplied by a factor of 0.6 to find the wave crest height (H_{crest}) above the MSL, as shown in [Petrova and Guedes Soares, 2008]. The two remaining structural requirements given above are straight forward to calculate. The minimum air gap is measured from H_{crest} to the access platform height. I assume the access platform height for the WindCrete model to be 9 m, though this is not stated. This assumption is based on the known WindCrete hub height of 135 m, and the known semi-rotor diameter, which is half the rotor diameter, of 120 m. The highest access platform height that still would satisfy the third requirement listed above is then 9 m. The actual air gap in the WindCrete model is then found by subtracting H_{\max} from the access platform height.

Table 6 shows a comparison between the structural requirements for the Utsira and the Gran Canaria sites. The minimum hub height for the WindCrete model is determined by the third requirement listed above, as the access platform is both out of the reach of $H_{s,50}$, and the air gap is over double of the minimum requirement. For the Utsira tower, second requirement listed above would place the access platform at a height of 16.9 m, which is over the tower base height. Alternatively, the access platform must be designed to be exposed to the hydrodynamic forces from large waves. I choose to determine the hub height by placing the access platform at the height of H_{crest} , which is closer to the tower base height. As a consequence, the actual hub height of the Utsira model is 1.5 m lower than the calculated minimum hub height given by the requirements listed above. The argument behind this choice is that I wish to increase tower height as little as possible. The added cost of designing a stronger access platform is counteracted by the saved cost of a lower tower.

Table 6: Structural requirements with input data

| | | Gran Canaria | Utsira |
|--------------------|-----|--------------|--------|
| H_s | [m] | 1.5 | 2.2 |
| $H_{s,50}$ | [m] | 5.1 | 13.8 |
| H_{\max} | [m] | 9.5 | 25.7 |
| H_{crest} | [m] | 5.7 | 15.4 |
| Minimum air gap | [m] | 1.5 | 1.5 |
| Actual air gap | [m] | 3.3 | 0.0 |
| Minimum hub height | [m] | 135.0 | 142.9 |
| Actual hub height | [m] | 135.0 | 141.4 |

4.2.2 Tower model

I design the Utsira tower using steel instead of concrete. I choose this approach because steel is a more commonly used material for wind turbine towers. This causes significant changes of the tower properties. These changes are tested against some benchmark values to verify the structural integrity of the tower. The IEA 15 MW offshore reference turbine has a much more similar design, as it is a steel construction. For this reason, I choose to use the reference tower described in [Gaertner et al., 2020b] as a base case. I calculate the static bending stress throughout the height of the reference tower. This is compared to the static bending stress of the adjusted tower, with a heeling angle of six degrees. I then increase the wall thickness (th) of the Utsira tower until the bending stiffness does not exceed the reference tower values. This method follows the work of Ane Vatshelle in her master's thesis [Vatshelle, 2020].

For the reference tower, the bending moment is mainly a result of a thrust force from the wind applied to the rotor, and the center of mass offset by the RNA. Following the global coordinate system, this offset has a negative value, and will counteract the contribution from thrust force. Equation (4.2) gives the bending moment, M through the height of the tower. The first subequation gives the bending moment for a tower with no angle of heel, so that the tower is symmetric around the global z axis. I use this equation to calculate bending moments for the IEA reference bottom-fixed wind turbine tower. For the Utsira floating wind turbine tower, the calculation must include the contribution from the weight of the heeling tower. This is included in the second subequation.

$$M_0 = T_{\max} z_{\text{rna}} + m_{\text{rna}} x_{\text{rna}} g \quad (4.2a)$$

$$M_{\text{Utsira}} = M_0 + (m_{\text{rna}} z_{\text{rna}} + m_{\text{tower}} z_{\text{tower}}) g \eta_5 \quad (4.2b)$$

Here, M_0 is the bending moment for each tower section, with no angle of heel. T_{\max} is the rated thrust of the turbine, which is 2.4 MN, see Table 3. The vertical distance from each tower section to the RNA center of gravity is z_{rna} . Further, x_{rna} is the horizontal offset of the RNA center of gravity. M_{Utsira} is the bending moment, including contributions as a consequence of a heeling angle. I choose a static heeling angle of six degrees for the bending stress calculations. This may be a conservative approach, as the predesign basis of the WindCrete spar support platform was to keep the static pitch of the platform due to maximum thrust force within four degrees [Mahfouz et al., 2020, p.13]. Moments are calculated from sections along the height of the tower, and so m_{tower} and z_{tower} is the total mass and center of gravity respectively of the tower between a specific section and the tower top. The results are plotted in Figure 9.

I then adjust the wall thickness of the tower, as previously explained. I use a 4th order polynomial fitting to smooth the step-like shape of the original wall thickness. This polynomial is in turn multiplied by a linear function $f(z) = az + b$:

$$\text{th}_{\text{Utsira}} = \text{th}_{\text{ref}} (az + b) \quad (4.3)$$

where z is the height from the tower base. The coefficients a and b of the linear function are found iteratively. Figure 9 compares the bending stress throughout the two towers. Notice how the bending stiffness for the reference tower increases close to the base, while the value for Utsira decreases. This is caused by the outer diameter of the reference tower being constant at 10 m close to the base, while the Utsira tower increases in width to meet the support structure at a diameter of 12.42 m. Also, notice how the bending stress changes sign near the tower top. This is caused by the 1017 t RNA with a CoG offset in the direction of the incoming wind. The mass contribution from the RNA CoG is larger than the thrust force contribution near the tower top.

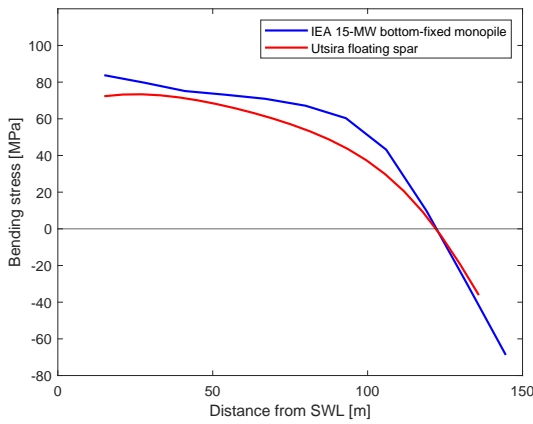


Figure 9: Bending stress throughout the height of the tower.

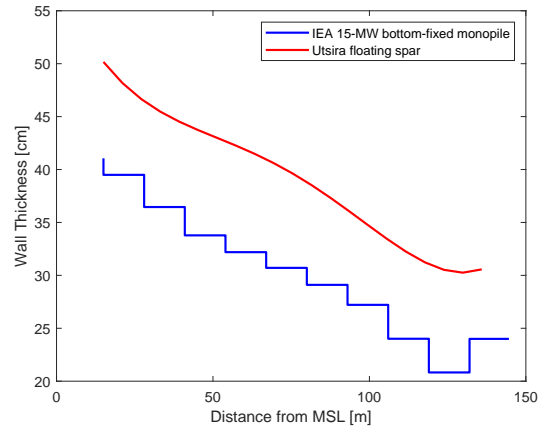


Figure 10: Wall thickness throughout the height of the tower.

Figure 10 shows how a significant increase in wall thickness is required to not exceed the values of the IEA reference wind turbine tower. The tower walls are increased in thickness inwards, and so the outer diameters are not affected when adjusting wall thickness. To re-iterate, I do adjustments of the WindCrete OpenFAST model to create

the Utsira model, but compare bending stress and wall thickness with the IEA reference wind turbine model. Thus, I chose both the tower top diameter and the tower base diameter to equal the WindCrete values in the first iteration of tower adjustment. After some iterations, I found it necessary to increase the tower top diameter from 6.5 m to 7.5 m, in order to avoid tower mode natural frequencies close to the 3P frequency range. Figure 11 shows the final outer diameters of the Utsira model after all adjustments. The initial tower diameter for the first iteration is marked in red.

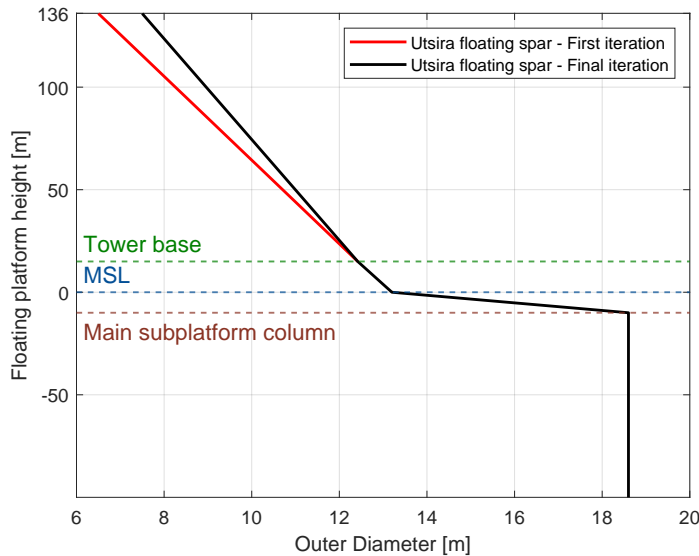


Figure 11: Outer diameter of the adjusted Utsira tower.

4.2.3 Support platform model

I will use the exact same support platform as used in the WindCrete model, only adding some ballast to the interior of the structure, to compensate for adjustments done to the tower and mooring lines. The platform is connected to the tower base at 15 m above the MSL, and stretches down to -155 m. The two main parts of the platform is the outer shell structure with concrete walls, and the internal solid aggregate ballast. The top of the shell structure consists of a truncated cone with a diameter of 12.42 m at the tower base, expanding to 13.2 m at the MSL. Then follows a truncated cone reaching a diameter of 18.6 m at a depth of 10 m below the MSL. This section connects to a 135.7 m long hollow cylinder. The bottom of the platform is a half dome shape with a radius of 9.3 m.

I have written a MATLAB routine to model the WindCrete support platform, with each of its geometric shapes. Using this routine, I calculate the resulting dimensions of the added ballast, together with new subplatform properties such as center of gravity, displacement, and mass moment of inertias. The added ballast calculation consists of two operations. The first operation is adding the weight difference between the concrete CoreWind model tower and the Utsira steel tower. The second operation is subtracting the weight corresponding to the increased vertical forces from the mooring lines. The process of finding a new mooring layout is described in Section 4.4. This process is iterative, as visualised in the flowchart in Figure 8. The solid aggregate ballast fills the interior of the half dome, and the bottom part of the main cylinder. Figure 12 shows the

dimensions of the new Utsira support platform after the final iteration, with the added ballast marked in red. The total weight of added ballast to the spar interior after the final iteration is $1.8948\text{E}+06$ kg. As a result, the equilibrium heave position is kept close to the original value.

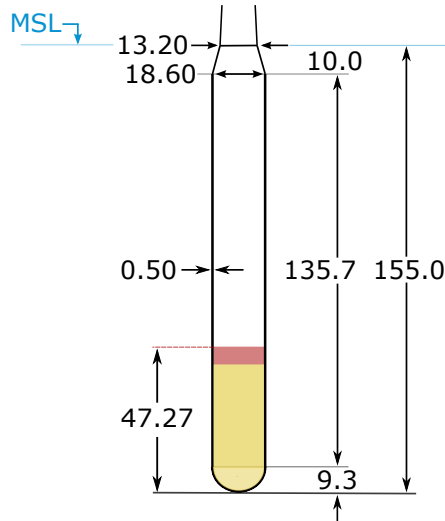


Figure 12: Utsira support platform (values in meters). Adapted from [Mahfouz et al., 2020]

As discussed above, I only do adjustments to the interior ballast of the WindCrete spar support platform. This means that the total submerged displacement is kept close to the original volume of $4.054\text{e}+04$ m³. As a consequence, the changes in buoyancy force acting on the adjusted support platform remains small. An alternative method for restoring the equilibrium heave position could be to reduce support platform volume. Reducing the draft of the spar, or even reducing the spar cylinder radius, could have production cost benefits. However, this would reduce the metacentric height, leading to less platform stability. Support platform optimization for the Utsira model could be the basis of future work.

4.3 Additional requirements

After constructing a model that complies with the structural requirements given by the standards, The tower is tested for stability and structural integrity. The main challenge is to ensure that the natural frequencies of the tower does not resonate with the 1P and 3P frequencies of blade rotation. This is done by using the BModes software. I also compare the blade tip clearance and the center of rotation with the WindCrete model. These elements are important for the structural integrity and stability of the system. I further discuss this in the following sections.

4.3.1 Blade rotation frequencies

The range of rotor rotational speeds ranges from 5 rpm at cut-in and 7.56 rpm at rated wind speed. This range defines a 1P frequency range of [0.0833 to 0.126] Hz and a 3P frequency of [0.25 to 0.378] Hz. The 3P frequency corresponds to the frequency when any of the three blades pass the wind turbine tower. If the tower vibrates with a natural frequency near the 3P frequency range, then resonance will occur. This resonance would create instability, which increases wear and might cause damage to the construction. The natural frequencies of the tower are higher than the 3P frequency. I choose a safety margin of 20% above the 3P frequency at rated wind speed, and adjust the tower properties until the natural frequencies are outside this margin. I did several iterations of adjustments to achieve this. In addition to increasing the thickness of the tower walls, I also increased the radius of the tower cylinder. This causes some challenges regarding the rotating blades, which will be discussed in the next paragraphs.

4.3.2 Blade tip clearance

Increasing the tower radius is a viable method for increasing the tower's natural frequencies, as discussed previously. I choose to keep the diameter at the tower base constant, and then gradually increase the tower top diameter until acceptable natural frequencies are achieved. This does assume that the RNA bedplate is adaptable to account for the increased diameter. The radii throughout the tower height follow linearly between the top and bottom diameter. In doing this, it is necessary to consider the blade tip clearance as it rotates across the tower, pointing downwards along the z-axis. To determine this blade tip clearance, a closer look at the turbine geometry is needed.

Consider a side-view of the turbine, with the rotor pointing leftwards, see Figure 13. First, the rotor shaft is tilted six degrees clockwise around the y-axis. Let the rotor plane be defined as the plane orthogonal to the rotor shaft. This creates a six degrees angle between the rotor plane and the yaw axis through the tower center. Second, we have a rotor precone angle of four degrees, which further extends the clearance. Finally, the blades have a prebend away from the tower, with a horizontal distance of 4 m separating the root and the tip chord line. This again extends the blade tip clearance. This is a conservative design, as stated in the definition of the IEA 15 MW reference wind turbine. According to this definition, the out-of-plane tip deflection remains below 22.8 m even under worst-case loading on the blades [Gaertner et al., 2020b, p.vii]. In the IEA reference model, the unbent blade tip has a clearing of 30 m to the tower. As a simple estimation, assume that the blade tip is rotating in the rotor plane at a radius of 120 m. This is of course an approximation, as the blade bends in a curve when sufficiently loaded. The blade tip passes the tower at an approximate distance of $120m * \cos(6) = 119.34m$ from the rotor apex height. Let the height of these two points be defined as the critical height, see Figure 13. I will compare the horizontal clearance between the two points for the reference turbine, the WindCrete turbine, and the Utsira turbine.

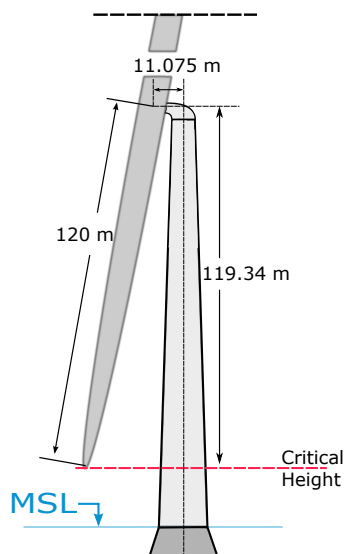


Figure 13: Side view of wind turbine with its rotor plane. The critical plane marks an estimation of where the blade tip passes the tower. Dimensions are not accurate.

The next step is to find the tower radius in the critical height of each tower model. The individual critical heights are found by simply subtracting 119.34 m from each individual hub height. Let the tower radius at the critical height be defined as the critical radius. We then have the following clearances between the blade tip with maximum out-of-plane deflection, and the outer wall of the tower:

Table 7: Critical radii and blade tip clearance for IEA Reference, WindCrete and Utsira structures. Clearance refers to the horizontal distance from the blade tip to the tower wall.

| | IEA Reference | WindCrete | Utsira |
|---------------------|---------------|-----------|--------|
| Critical radius [m] | 4.99 | 6.19 | 6.07 |
| Clearance [m] | 7.2 | 6.0 | 6.12 |

The calculated clearances for both WindCrete and Utsira structures are significantly smaller than in the reference model, as expected. This issue is not addressed in the WindCrete report. Nevertheless, the reference design is specified as being conservative. It is also reasonable to assume that the WindCrete structure satisfies this structural requirement. I will accept the clearance in the Utsira design as sufficiently large.

4.3.3 Center of rotation

I seek to estimate the center of rotation for the new model, and then compare this to the center of rotation in the WindCrete model. This comparison is useful for stability considerations. I have added a considerable amount of ballast below the original center of rotation to compensate for the reduced tower weight in the Utsira-model compared to the concrete WindCrete model. I expect the depth of the center of rotation to increase below the SWL (Still Water Level). I need to consider adjusting the locations of the connection

between the mooring lines and the spar if there is a significant change of the center of rotation.

I initialize a pitch decay test, and look at the relation between the pitch and the surge motion. The platform is placed in a neutral initial position for all degrees of freedom except pitch and surge. I choose the initial pitch rotation to be five degrees. There are no waves or wind acting on the turbine.

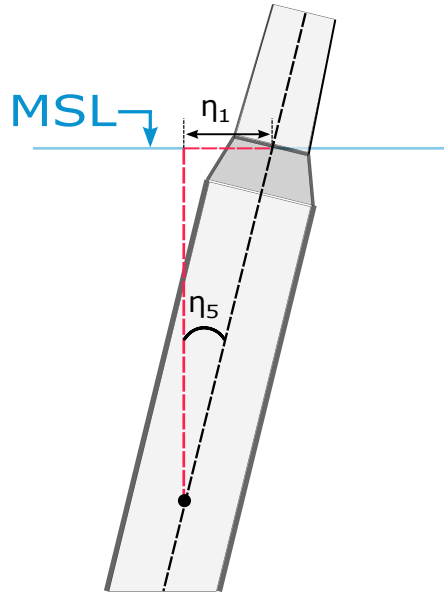


Figure 14: The geometric approach of finding the platform center of rotation. The illustration shows a greatly exaggerated pitch angle. Surge translation is η_1 and pitch rotation is η_5 .

Note also that platform motions in pitch and surge are coupled. The coordinate system for platform translation and rotation has its origin at the SWL, while the center of rotation is located far below this point. This is what causes the coupling. In the ideal case of no surge translation in the center of rotation, the wave form of the surge output will mirror the pitch oscillations perfectly. I expect the center of rotation to lie close to the connection point of the delta lines to the platform. For this reason, I choose the initial surge displacement so that the mooring connection points are close to the global z-axis. The calculation is as follows:

$$\eta_1 = 90m * \sin(5) = 7.8m \quad (4.4)$$

where η_1 is the initial surge displacement. I use the geometric approach visualized in Figure 14 to approximate the center of rotation, using a MATLAB routine. I view the surge translation as the shortest leg of a right-angled triangle. This leg is also the opposite side of the five-degree pitch angle. I then seek to find the adjacent side of this triangle. This leg of unknown length will approximate the depth of the center of rotation. It is more accurate to say that I seek the vertical position where the horizontal displacements are minimal throughout the time series.

The pitch decay output has a length of 3800 seconds. First, I subtract the mean value from each data point of the surge translation and pitch rotation respectively. I do this to account for the fact that the platform has a small displacement in both surge and pitch when it is in equilibrium. Note that this operation makes our geometric approximation somewhat less accurate, as the axis of surge translation along the SWL no longer is orthogonal to the vertical axis of the platform in equilibrium position. Second, I divide the surge translation by the tangent of the pitch rotation for each time step. Let the tangent of the pitch rotation be denoted as ϵ . I set a threshold of $\epsilon = 0.01$. All timesteps with $\epsilon < 0.01$ will be excluded from the calculation to avoid values close to zero in the denominator. Figure 15 shows the approximate depth of the center of rotation for the pitch decay test.

Finally, I take the mean of all the calculated adjacent legs. This gives the approximate vertical center of rotation of 89 m below SWL. For the WindCrete structure, the exact same approach gives a center of rotation of 82 m below SWL. The restructure process has brought the center of rotation closer to the fairlead, as expected. Considering this, I choose to keep the fairleads at their original placement.

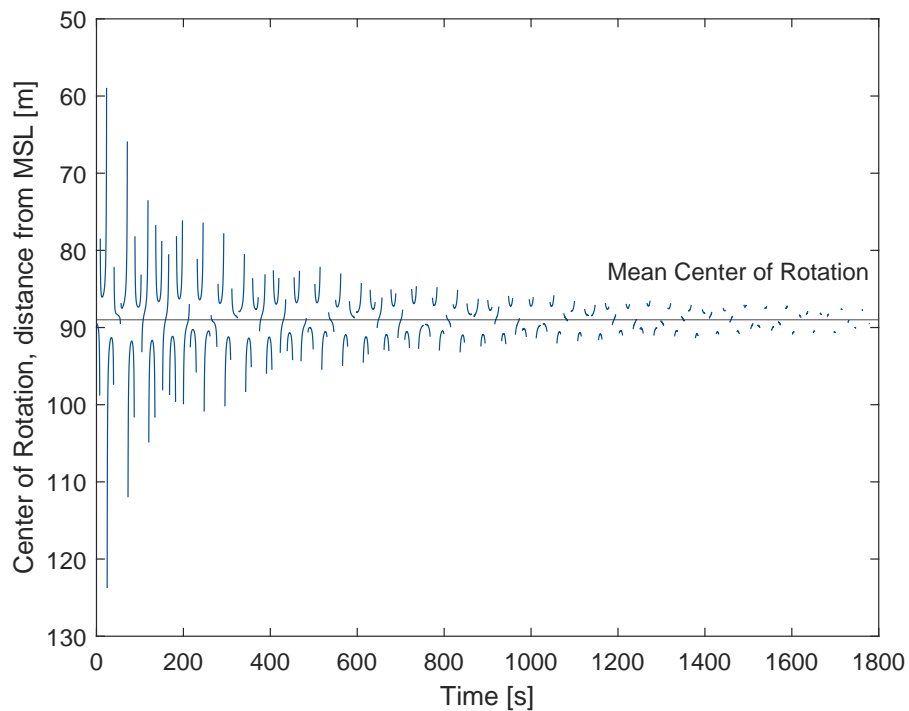


Figure 15: Center of rotation of the new Utsira floating wind turbine model

4.4 Adapting mooring to new depth

Figure 16 demonstrates a typical catenary mooring layout with three anchor points. The WindCrete OpenFAST model has mooring lines divided into two main sections. The first section is the main line, which is connected to the anchor points. These anchor points are placed at a radius of 600 m from the center of the spar in the WindCrete model. The main line accounts for the most part of the total mooring line length, and for the WindCrete model, this section consists of a 565 m long chain. The second section of the mooring line is the delta line, which connects the mooring line to the subplatform fairleads in a crowfoot pattern. This gives the mooring system additional stiffness in yaw, which contributes to platform stability. In the WindCrete model, each delta line is 50 m long.

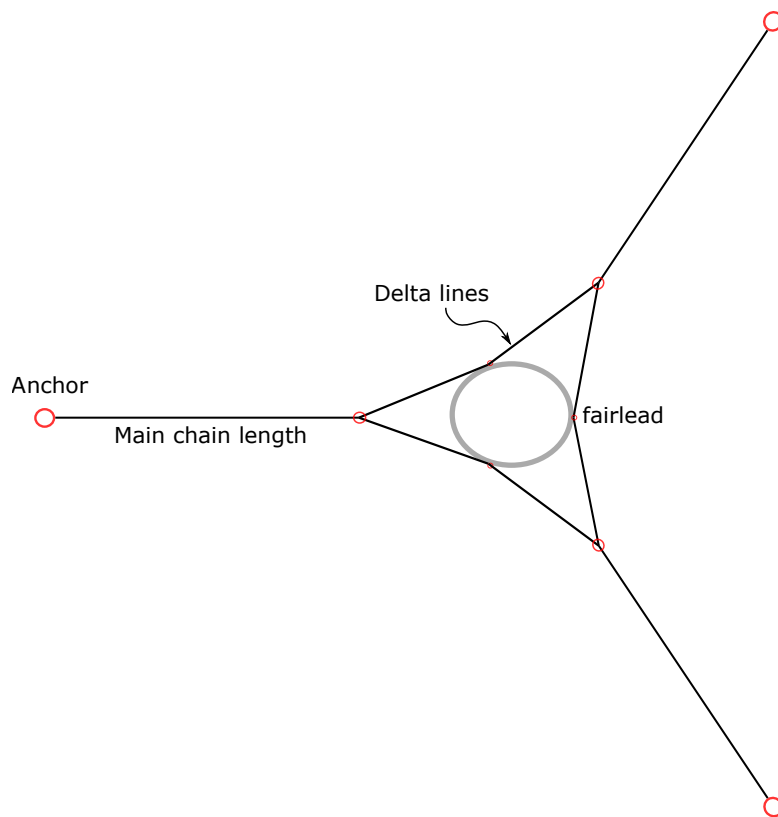


Figure 16: A typical catenary mooring layout, with delta lines. The figure is not to scale, for demonstrational purposes.

The Utsira site has an area of 1010km² with depths ranging from 185 m to 280 m [Drivenes et al., 2010]. The average depth is 267 m, which is significantly higher than the 200 m depth of the Gran Canaria site. I seek to adapt the layout of the three catenary mooring lines, to fit the new water depth. Realistically, the mooring lines should be optimized for each specific location, as the range of water depth within the site is broad. However, the adaptation in this thesis is done for one specific depth, 250 m. I do not aim to optimize the mooring system. I choose to keep the catenary chain as used in the WindCrete system. The adaptation is done by increasing both the length of the main line sections and the radius of the anchoring points. I keep the delta line geometry used in the WindCrete model.

4.4.1 Deciding on a layout

There are several considerations that must be done when choosing the new mooring layout, some of which is discussed here. First, I want the forces applied to the anchor to act in the horizontal direction. I assume the anchors to be strong in the horizontal direction, and weaker in the vertical. For this reason, I want to avoid any uplifting forces in the anchor points. To ensure this, I require a safety margin between the touchdown point of the line and the anchoring point. I choose a safety margin of 10% of the anchor point radius to rest on the seabed, even under extreme environmental conditions. This is visualized in Figure 17.

Second, a new mooring layout may cause changes to the stationkeeping abilities of the system. Some changes are expected, such as decreased natural frequency and increased displacement in surge. Also, the delta lines provide the main restoring forces in yaw rotation, and so a new layout will influence yaw characteristics. However, platform heave requires special attention. Increasing water depth causes the length of line between the fairlead and touchdown at the ocean floor to increase. The weight of this extra line segment is added to the platform weight, causing the platform equilibrium position to shift downwards. This reduces the air gap between the blade tips and the MSL. I remove some internal ballast, so that heave displacement remains small in equilibrium. This requires a new iteration of calculating subplatform properties, as seen in the flowchart in Figure 8.

Third, I consider the length of mooring lines in the new layout. Mooring lines can be expensive and challenging to install. An important part of optimizing the mooring layout is to reduce costs. As mentioned before, I will use a simple approach, as optimization is not in focus for my thesis. Still, I aim to do a reasonable estimation of the layout dimensions.

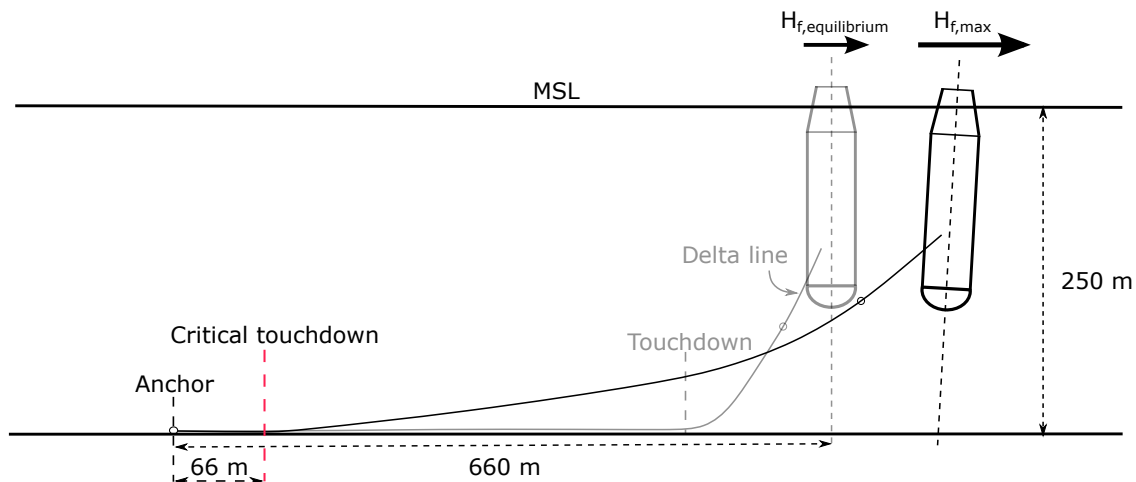


Figure 17: The catenary mooring line. The chain must not be lifted vertically past the critical touchdown point when the platform is loaded with maximum horizontal force ($H_{f, \text{max}}$).

4.4.2 Calculations of new mooring line dimensions

I determine both the radius of the anchor points and the length of the catenary lines using a combination of OpenFAST simulation and a MATLAB routine written by F.G.

Nielsen [Nielsen, 2021]. The MATLAB routine computes mooring line geometry and restoring characteristics using the elastic catenary Equations (2.4). It gives the static geometries of a single catenary line, given a range of horizontal forces applied to the fairlead. In this routine, the catenary line is modelled as two segments. The first segment is from the anchor point to the delta line. The second segment is the delta line, which is connected in two fairlead points. The delta line is simplified to one single line connected to the subplatform in $[x,y,z] = [-9.3, 0, -90]$. I double both the weight per unit length and the axial stiffness per unit length for this segment, to approximate the delta line as two parallel line segments. I then set the water depth to 250 m, and guess values for both the anchor point radius and the line length before computation.

The MoorDyn submodule calculates the position of each segment between all nodes in the predefined lumped-mass model. These positions can be included in the output files. The model allows user-defined segment lengths between the anchor node and the connection node where the main line meets the delta line. I set the number of line segments between these nodes so that each segment has a length of approximately 10 m. I am then able to get a rough estimation of the touchdown point throughout the simulation. MoorDyn also calculates the horizontal forces in the fairlead nodes. I will analyze these horizontal forces to define a range of applied loads. The maximum applied load must not cause the line to lift up past the critical touchdown point.

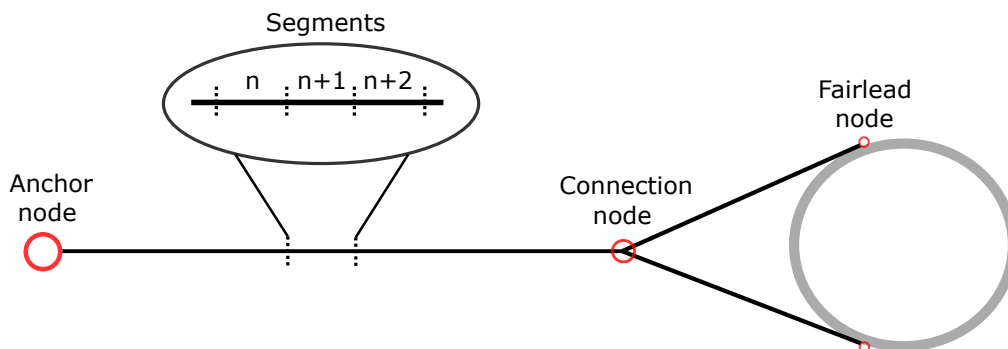


Figure 18: Each separate mooring line is defined in four nodes. The user may specify the number of segments between each node point.

I start the iterative process of finding the new mooring layout. First, I define an initial guess of the new mooring configuration in the MoorDyn input file. I then do an OpenFAST simulation with no wind or waves, to find the new system equilibrium. I sum the averaged horizontal forces in the two fairlead nodes associated with line number one. This line stretches in the xz -plane. The calculation gives an approximate average horizontal force of 3.3 MN. This gives the lower boundary for the range of horizontal forces that I wish to investigate in the MATLAB routine. Recall, this routine calculates one anchored line with a horizontal force applied to the top end, see figure 17. When I apply the lower boundary horizontal force, I want the horizontal coordinate of the fairlead in equilibrium position to match the anchor point radius. I risk vertical forces in the anchor point if the line is too short. The stationkeeping abilities of the mooring system are reduced if the line is too long. The platform must not drift too far from equilibrium at any applied loads. If the fairlead coordinate in the static case matches the equilibrium simulation, then the ratio between anchor radius and line length is good.

I then do a simple estimation of the maximum horizontal forces applied to the platform. I apply the rated thrust force of 2.4 MN, and then add a small extra margin of 0.3 MN to the horizontal forces at the top end of the mooring line. This sums up to a horizontal force of 6.0 MN, which is just an arbitrary guess of an upper bound on the range of applied horizontal forces. I apply 6 MN of force to the static line configuration, and require that this does not cause the touchdown point to exceed the critical touchdown. I then run simulations with different environmental conditions, as presented in Chapter 5. I apply the same output analysis as used to find the horizontal forces in equilibrium position, and find that the horizontal forces stay well below the guessed maximum. Therefore, the mooring layout I find by using 6.0 MN as an upper limit is likely an overestimation, but I find it sufficient for this analysis.

I analyze the output segment positions, to find the closest segment to the anchor that does not experience any significant vertical displacement. This segment should be close to the touchdown point of the line as found in the MATLAB computation. I do not expect the touchdown point to coincide accurately. This is because MoorDyn simulates a dynamic system, and the line is not static. I then compare the touchdown points of the static mooring line geometry with the OpenFAST output. I repeat this process until I find a balanced layout, where the touchdown point is close to, but not exceeding the critical value under extreme conditions. I found that small changes in main line length or anchor radius give large changes in touchdown point. Thus, this process required many iterations.

4.4.3 Static layout

Properties of the Utsira mooring layout are presented in Table 8. These properties describe node positions of the mooring layout with the platform placed in static equilibrium in the global origin. These node positions are required as input in MoorDyn, and will give the initial positions of the mooring layout. Upon initialization, MoorDyn will perform a dynamic relaxation routine to get an initial position that is closer to a static case. This reduces mooring line contributions to startup transients.

Table 8: Static properties of the Utsira mooring layout.

| Node type | x | y | z |
|-------------------|--------|---------|--------|
| (-) | (m) | (m) | (m) |
| | Line 1 | | |
| Anchor | -660.0 | 0.0 | -250.0 |
| Delta connection | -44.1 | 0.0 | -119.9 |
| First fairlead | -4.65 | 8.05 | -90.0 |
| Second fairlead | -4.65 | -8.05 | -90.0 |
| | Line 2 | | |
| Anchor | 330.0 | 571.58 | -250.0 |
| Delta connection | 22.05 | 38.19 | -119.9 |
| First fairlead | 9.3 | 0.0 | -90.0 |
| Second fairlead | -4.65 | 8.05 | -90.0 |
| | Line 3 | | |
| Anchor | 330.0 | -571.58 | -250.0 |
| Delta connection | 22.05 | -38.19 | -119.9 |
| First fairlead | 9.3 | 0.0 | -90.0 |
| Second fairlead | -4.65 | -8.05 | -90.0 |
| Delta line length | 50 m | | |
| Main line length | 642 m | | |

Figure 19 shows the static layout for a range of horizontal forces applied to the top end of the line. The lower boundary corresponds to the horizontal force in equilibrium position. This layout is as described in Table 8, which is the final mooring layout. Here it is clearly demonstrated how a small displacement at the top end causes a large translation in the mooring touchdown point. With maximum horizontal force applied to the static configuration, the touchdown point is at a distance of 81 m from the anchor point in this static configuration. This is comfortably above the required 10% clearance from touchdown to anchor point.

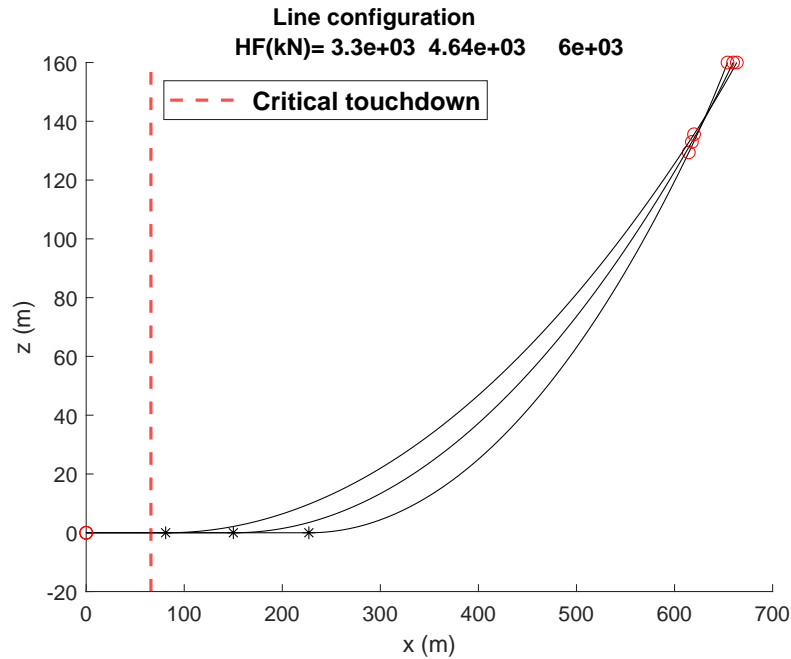


Figure 19: Plot of catenary lines for 3 cases: $H_{f,\text{equilibrium}}=3300\text{kN}$, $H_f = 4640\text{kN}$ and $(H_{f,\text{max}}) = 6000\text{kN}$. Here, the origin is in the anchor point at the sea floor. Created with MATLAB routine from [Mat, 2021].

Figure 20 shows the touchdown point of a static catenary line for a range of horizontal forces applied to the top end. The slight flattening of the curve demonstrates how the restoring stiffness increases as a greater length of the chain is lifted off the seafloor. The critical touchdown line corresponds to a distance of 60 m from the anchor point.

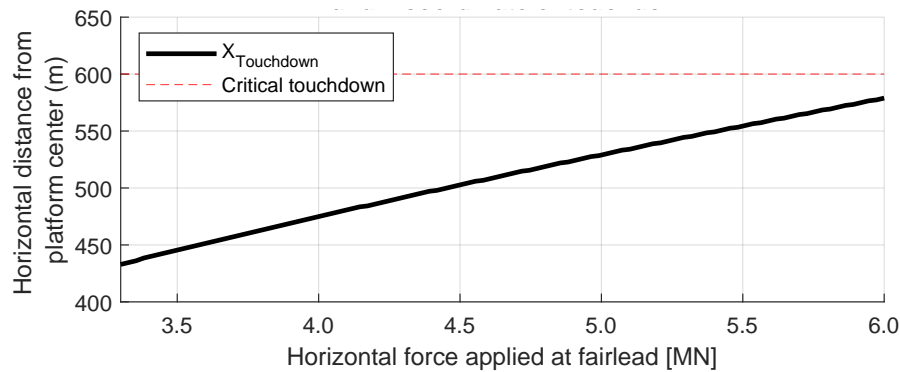


Figure 20: Horizontal distance from the touchdown point to the fairlead position, against force applied to the fairlead. Created with MATLAB routine from [Mat, 2021].

4.4.4 Touchdown point

Figure 21 shows the output z -position of a line segment at a distance of 139.4 m from the anchor. This is the closest section to the anchor point that experiences significant displacements in the z -direction. Figure 22 shows the corresponding horizontal forces applied to the top end of this line, through the two fairleads. These outputs are from the simulation with 13 m/s turbulent wind and waves, see Section 5.3.1. The average horizontal force applied in the x -direction for this simulation is approximately 4230 kN.

As we can see, the line segment is just barely lifted from the seafloor periodically. For example, the line is lifted periodically from the seafloor between 1000 s and 1500 s in the time series. In this period, horizontal forces reach over 5 MN. Looking at Figure 20, we see that for an applied horizontal force of 5 MN, the static line would touch down at approximately 525 m from the origin. This corresponds to 135 m from the anchor. Thus, the static case agrees with what we see from the OpenFAST output in this situation. Similarly, between 1500 s and 2000 s, Figure 21 shows that the line rests at the seafloor, thus the touchdown point is at a greater distance than 139.4 m from the anchor. In the same time period, the applied horizontal forces reaches a maximum of approximately 4.7-4.8 MN. In this case Figure 20 gives a touchdown point at a distance of approximately 145-150 m from the anchor point. Thus, the static case also agrees with what we see from OpenFAST output for this time period.

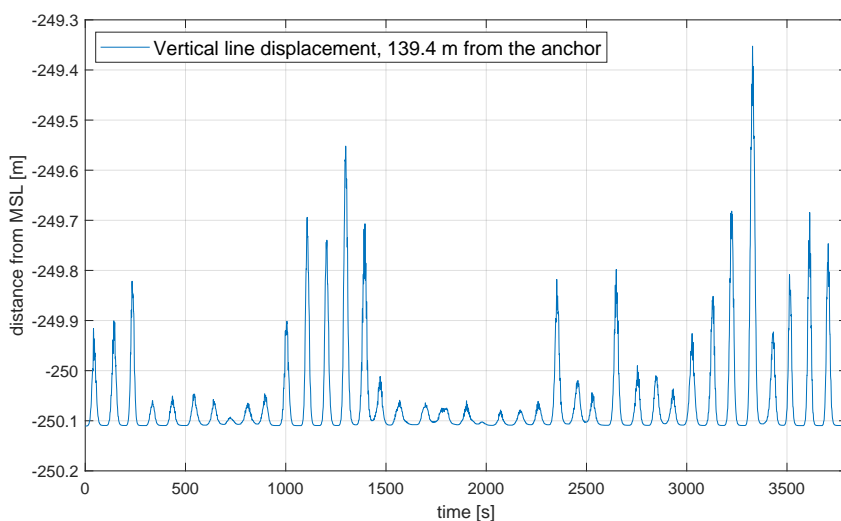


Figure 21: Z-coordinate of line segment at a distance of 139.4 m from the anchor in line 1. Here we see that the line is lifted from the seafloor periodically, but also experiences some periods with no vertical displacement.

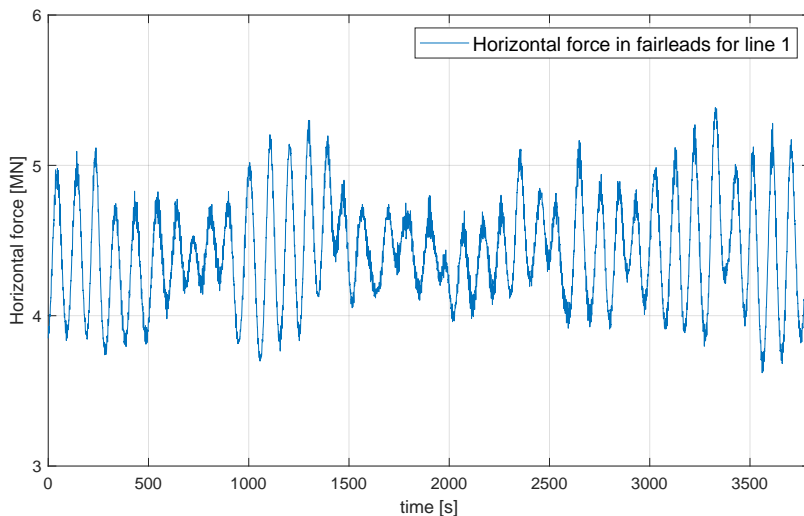


Figure 22: Horizontal forces in the two fairleads associated with line 1.

The discussion in the paragraphs above shows that the final mooring layout is conservative, as the touchdown point stays at a distance of more than 20% of the mooring line length, even for simulations with wind speeds around the rated wind speed. Figure 5-13 in the WindCrete report shows that maximum surge displacement is reached when applied thrust force is greatest, which is at rated wind speed [Mahfouz et al., 2020, p.27]. Thus I find it reasonable to believe that the touchdown point does not cross the critical touchdown point at any realistic range of environmental conditions. However, I have not done simulations with a producing wind turbine and with extreme waves. I expect that large loads from waves would affect the touchdown location. Optimizing the mooring layout would require simulation of many more load cases, but that is outside the scope of this thesis.

Mooring stiffness

The stiffness in surge is stated as $5.0523e+05$ N/m for the WindCrete model [Mahfouz et al., 2020, p.22]. I expect the surge stiffness to somewhat decrease, as I extend both the anchor radius and the line length when fitting the mooring layout to the increased depth of the Utsira site. I aim to approximate $\mathbf{C}^{(m)}$ from Equation (2.25) by using OpenFAST simulations, following a procedure outlined in a NREL forum discussion [Jonkman, 2005]. I start by running three separate simulations with all platform DoFs disabled. In the first simulation, I lock the platform in $(x,y,z)=(0,0,0)$, and let the mooring lines stabilize over a period of 600 seconds. In the second and third simulation I impose 1 m surge and heave displacements respectively.

The $\mathbf{C}^{(m)}_{11}$ element is approximated as the difference in horizontal force in the 6 fairlead nodes by displacing the platform by one unit length in surge. The $\mathbf{C}^{(m)}_{33}$ element is approximated as the difference in vertical force in the six fairlead nodes by displacing the platform by one unit length in heave. I apply Equation (2.22), but in this case, $\frac{\partial F_i}{\partial j}$ approximates $\mathbf{C}^{(m)}_{11}$ and not $\mathbf{C}^{(l)}_{11}$. This is because contributions from all three mooring lines are included in MoorDyn. The remaining elements follow from the theory as explained in Section 2.3.7, but without summing over the rotated lines.

I wish to investigate the impact of the mooring stiffness when it comes to tower modes. The reason for this is that though I expect the mooring stiffness to have a great impact on the translational and rotational movements of the floating platform and thus the tower, I do not expect it to have any major impact on the tower fore-aft and side-to-side displacements. This is investigated in Section 4.5. I choose to do this comparison with data from the OC3Hywind project [Jonkman, 2010, p.18]. The Offshore Code Comparison Collaboration (OC3) project is an effort by the IEA to validate and verify a range of aero-hydro-servo-elastic codes or simulation tools [Jonkman and Musial, 2010]. This work involves a slight modification of the Hywind spar model, to make the spar support platform appropriate for supporting the NREL 5-MW reference wind turbine [Jonkman et al., 2009]. The OC3Hywind model is a well-documented spar design with openly available input files. It has a similar design to the Utsira model, but the mooring stiffness matrix is different.

The mooring stiffness matrix for the OC3Hywind tower mode calculations is found in the main BModes input file [Jonkman, 2020]. This is identical to the linearized restoring matrix given for the OC3Hywind project [Jonkman, 2010, p.18], except for elements (4,4)

and (5,5). These elements have been augmented to include the contribution of the gravitational terms. I include the same augmentation in the new mooring stiffness matrix. The augmentation is adding $-z_{COG}Mg$ to terms (4,4) and (5,5), where z_{COG} is the vertical distance from MSL to the center of gravity, and M is the total system mass. This matrix also contains an additional yaw stiffness term in element (6,6), to account for the restoring properties of the delta lines. I find this by manually adjusting the additional yaw stiffness term until the BModes output frequency matches the natural frequency found in the yaw decay simulation.

4.5 Finding new tower modes

I have adjusted the tower, the support platform, and the mooring layout from the WindCrete OpenFAST model to fit the environmental conditions of the Utsira site. I then must calculate tower modes, to ensure that the natural frequencies of the tower modes lie outside the 3P frequency range, as discussed in Section 4.3.1. In the following paragraphs, I discuss the input data required for running the BModes program, and I also discuss necessary post-processing of the output data in order to find the tower modes to be input in the Utsira OpenFAST model.

4.5.1 BModes input data

The BModes executable requires two input files. The first input file contains properties for distributed sections of the tower. True values of the tower properties may need to be modified to fit the OpenFAST tower model. In OpenFAST, only the fore-aft and side-to-side bending is accounted for. This means that the tower model is a straight beam of isotropic material with no elastic offsets and no axial, torsional, or shear DOFs. The torsional and axial stiffness inputs for each section should be set high enough so that it does not impact the output fore-aft and side-to-side modes that we are interested in.

The second input file contains all the main inputs such as general parameters, tower-top mass properties, finite element discretization, and tower support subsystem properties. For this thesis, the main input file is based on the input files provided by the IEA 15-Megawatt Offshore Reference Wind Turbine project [Gaertner et al., 2020a]. The IEA project uses the same RNA and blades as used in this thesis, thus the tower-top mass properties can be found directly. The code allows tip attachments for both blade and turbine mode calculations. For the tower mode calculations, the RNA is assumed to be a rigid body mass with six moments of inertia. The center of mass for this tower tip attachment is not required to lie on the central vertical tower axis. The potential offsets are specified in the main input file. The inertia contribution from the RNA can substantially influence the coupled modes of the tower.

The section containing the properties of the tower support subsystem requires some calculations. This part of the floating turbine structure is simply referred to as the platform. The platform includes the transition piece below the tower base, starting at 15 meters above SWL. It is considered as a rigid body, with a cantilevered tower at the top. The model needs the platform center of mass location, as well as the total platform mass. Further, four matrices are required. These matrices sets the boundary conditions when solving Equation (2.3).

Platform mass inertia

The platform mass inertia matrix elements are provided in the CoreWind report for the WindCrete platform [Mahfouz et al., 2020, p. 17]. The support platform used in this thesis is structurally identical, except for the ballast added to account for the reduced weight of the new tower. This added ballast is placed on top of the existing ballast, with the same solid-cylindrical shape. The parallel axis theorem relates the mass moment of inertia of the added ballast about its local center of mass, relative to its mass moment of inertia about the platform center of mass. Following the theory presented in section 2.3.4, the new platform mass inertia matrix given as input, I_{new} becomes:

$$I_{new} = \begin{bmatrix} 5.5970e + 10 & 0 & 0 \\ 0 & 5.5970e + 10 & 0 \\ 0 & 0 & 0.1901e + 10 \end{bmatrix} \quad (4.5)$$

Added mass matrix

The second matrix required as input in BModes is the platform-reference-point-referred hydrodynamic 6X6 matrix. This matrix can be generated by external programmes such as ANSYS-AQWA [Ansys 2021]. However, I will use a simplified method, following the strip theory as explained in Section 2.3.5. To verify the method used in this work, I calculated the added mass matrix for the OC3Hywind platform using strip theory as presented in Section 2.3.5. The result added mass matrix is found to be reasonably similar to the given input for OC3Hywind [Jonkman, 2020]. I therefore consider this approach as reasonable for this thesis.

The added mass matrix at infinite frequency is given in the WindCrete report, [Mahfouz et al., 2020, p. 18]. The two-dimensional added mass coefficient for horizontal movement, C_{ah} is unknown. I assume the value of C_{ah} to be similar to the coefficient used in the OC3Hywind model, $C_{ah} = 0.969954$. I then use Equation (2.14) to find the constant radius R of the vertical column. The value of R is found to be approximately 8.8 m, and follows from the added mass coefficient assumption. This radius is a bit smaller than the 9.3 m radius of the main subplatform column. Recall that the subplatform is tapered at the top and domed at the bottom. Considering this, I accept an approximate radius of 8.8 m as reasonable. The full added mass matrix for the vertical column is then:

$$\mathbf{A}_{col} = \begin{bmatrix} 3.7354e + 07 & 0 & 0 & 0 & -2.8949e + 09 & 0 \\ 0 & 3.7354e + 07 & 0 & 2.8949e + 09 & 0 & 0 \\ 0 & 0 & 1.2657e + 06 & 0 & 0 & 0 \\ 0 & 2.8949e + 09 & 0 & 2.9914e + 11 & 0 & 0 \\ -2.8949e + 09 & 0 & 0 & 0 & 2.9914e + 11 & 0 \\ 0 & 0 & 0 & 0 & 0 & 0 \end{bmatrix} \quad (4.6)$$

The units are [kg] for the $ij = \{11, 22 \text{ and } 33 \text{ terms}\}$, [kgm] for the $ij = \{15, 24 \text{ and } 51\}$

and $[\text{kgm}^2]$ for the $ij = \{44 \text{ and } 55\}$ terms.

Hydrostatic stiffness matrix

The third matrix required as input in BModes is the hydrostatic stiffness matrix. I find this using Equation (2.21), but with one augmentation. The gravitational restoring terms are not included in these calculations, as they are accounted for in the mooring stiffness matrix. BModes takes the sum of the hydrostatic and the mooring stiffness matrices internally, which means that the gravitational terms must only be included in one of these matrices. The calculated hydrostatic stiffness matrix, \mathbf{C}_h is:

$$\mathbf{C}_h = \begin{bmatrix} 0 & 0 & 0 & 0 & 0 & 0 \\ 0 & 0 & 0 & 0 & 0 & 0 \\ 0 & 0 & 1.375555e + 06 & 0 & 0 & 0 \\ 0 & 0 & 0 & -3.148042e + 10 & 0 & 0 \\ 0 & 0 & 0 & 0 & -3.148042e + 10 & 0 \\ 0 & 0 & 0 & 0 & 0 & 0 \end{bmatrix} \quad (4.7)$$

The units are $[\text{N/m}]$ for C_{33} and $[\text{Nm/rad}]$ for C_{44} and C_{55} .

Mooring stiffness matrix

The fourth and final matrix required as input in BModes is the mooring stiffness matrix, $\mathbf{C}^{(m)}$, from Equation (2.25). As discussed towards the end of Section 4.4.4, I wish to investigate the effect of mooring stiffness on the first tower modes. To do this, I run BModes with two different mooring stiffness matrices. The first simulation is done with a stiffness matrix from the OC3Hywind model [Jonkman, 2020]. The second simulation is done following the method described in Section 4.4.4, which gives a mooring stiffness matrix based on the Utsira model:

$$\mathbf{C}^{(m)} = \begin{bmatrix} 2.8142e + 05 & 0 & 0 & 0 & -2.5328e + 07 & 0 \\ 0 & 2.8142e + 05 & 0 & 2.5328e + 07 & 0 & 0 \\ 0 & 0 & 8.6620e + 04 & 0 & 0 & 0 \\ 0 & 2.5328e + 07 & 0 & 4.4035e + 10 & 0 & 0 \\ -2.5328e + 07 & 0 & 0 & 0 & 4.4035e + 10 & 0 \\ 0 & 0 & 0 & 0 & 0 & 0 \end{bmatrix} \quad (4.8)$$

Here, the units of each 3x3 section of $\mathbf{C}^{(m)}$ are:

$$\mathbf{C}^{(m)} = \begin{bmatrix} [N/m] & [N] \\ [N] & [Nm/rad] \end{bmatrix} \quad (4.9)$$

Comparing the two BModes outputs, I find that the mooring stiffness matrix has a significant effect on the mode frequencies of surge, sway and yaw, as expected. However, there are much smaller variations in the first and second tower mode frequencies. This implies that the mooring has a limited impact on the fore-aft and side-to-side tower modes. Table 9 compares BModes output tower mode frequencies using OC3Hywind and Utsira mooring stiffness matrices respectively.

Table 9: Fore-Aft and Side-to-Side mode frequency comparison

| | Description | Frequency with OC3Hywind mooring [Hz] | Frequency with Utsira mooring [Hz] |
|---------|------------------------------|--|---------------------------------------|
| Mode 7 | 1 st Side-to-Side | 0.459217E+00 | 0.461300E+00 |
| Mode 8 | 1 st Fore-Aft | 0.459984E+00 | 0.462007E+00 |
| Mode 10 | 2 nd Side-to-Side | 1.996044E+01 | 1.99611E+01 |
| Mode 11 | 2 nd Fore-Aft | 2.206985E+01 | 2.207037E+01 |

Based on these findings, I conclude that the mooring stiffness has a limited impact on the tower modes of interest. Thus, I accept some inaccuracy in the natural frequencies of the first 6 output modes from BModes, which corresponds to translational and rotational displacements. I proceed using Equation (4.8) as input in BModes.

4.5.2 Post-processing of BModes output data

BModes gives the first 20 tower modes as output. The first mode is the lowest frequency mode, and the subsequent modes are of increasing frequency. The first six modes correspond to the translational and rotational eigenfrequencies of the platform. I seek only the first two fore-aft and side-to-side tower modes for input in OpenFAST. These must be recognized from their modal frequencies. The relevant modes are modes 7, 8, 9, and 10 for the restructured tower. The lowest frequency for the modes of interest is mode 7. This mode frequency must be outside the 3P frequency range, to prevent resonant vibrations between the tower and the blades. This outlines the iterative design process of the tower, see also the flowchart in Figure 8. The first iterations gave tower mode frequencies within the 3P range. I then use a combination of increasing tower radius and increasing wall thickness until the tower mode frequencies exceed the 3P frequency at rated wind speed, with a safety margin of 20%. This is likely a conservative approach, which means that I may have increased tower top radius and wall thickness more than necessary.

Table 10: Final natural frequencies for the first 10 modes, after the last iteration. The maximum 3P frequency is 0.378 Hz, which makes mode 7 the closest in natural frequency, but still outside the safety margin of 20%.

| | | Frequency (Hz) |
|-------------|-----------|----------------|
| Mode Number | Mode Type | Utsira Tower |
| 1 | Surge | 0.0952 |
| 2 | Sway | 0.0952 |
| 3 | Heave | 0.0296 |
| 4 | Roll | 0.0307 |
| 5 | Pitch | 0.0308 |
| 6 | Yaw | 0.0760 |
| 7 | 1st SS | 0.4613 |
| 8 | 1st FA | 0.4620 |
| 9 | 2nd SS | 1.9961 |
| 10 | 2nd FA | 2.2070 |

I have done preliminary decay tests of the new Utsira model to check if both OpenFAST simulation and BModes gives similar natural frequencies in the translational and rotational DoFs. These OpenFAST decay tests are done by posing initial displacements in each respective DoF, with no input wave or wind fields. The mode frequencies for translational and rotational DoFs matches the decay tests well. This indicates that the four matrices specified in the BModes input file are fairly accurate. The small variations could be caused by several factors. The added mass matrix might be inaccurate, as it is frequency dependent. The simplified method used to find added mass is also based on assumptions that might not be accurate. For example, the two-dimensional added mass is assumed equal through the height of the substructure. This means that the end effects of the truncated top and domed bottom are not accounted for in the transverse added mass.

Each output mode from BModes contains displacements, slopes and twist for each specified span location of the tower. The span location is normalized by the beam length, and is defined in the main BModes input file. Figure 23 shows a plot of the modal displacements.

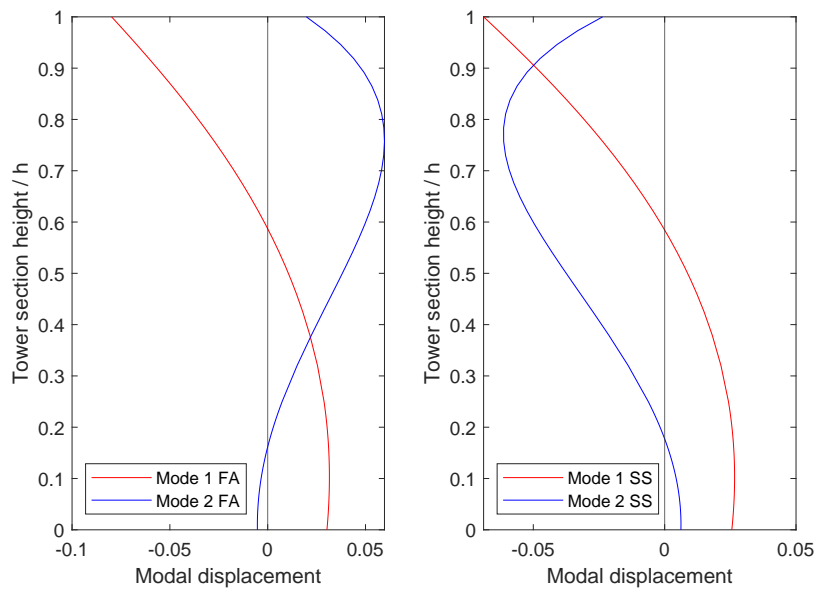


Figure 23: Modal displacements for the new tower.

OpenFAST requires that the 6th order polynomials describing the modal shapes sums to unity. To achieve this, the displacement values must be normalized by the tower top displacement. This must be done before using one of the provided routines for finding OpenFAST-style polynomials. I choose to use a MATLAB function named `GetFastStylePoly` [Prowell, 2017]. This function uses the improved direct method from the Excel spreadsheet provided in [Jonkman, 2020]. Figure 24 shows a plot of the polynomials found from `BModes`.

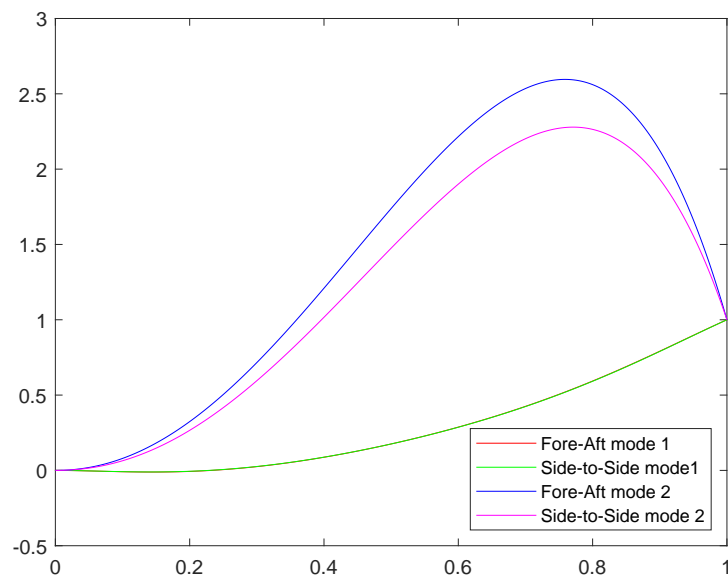


Figure 24: Normalized tower mode polynomials for the new tower. The fore-aft mode 1 has a very similar polynomial as the side-to-side mode 1, thus it is hidden behind the green line in the plot.

Table 11 shows the polynomial coefficients describing the tower mode shapes as seen in Figure 24. The coefficients for each mode sums to unity, as required by OpenFAST.

Table 11: Coefficients of the 6th order polynomials describing tower mode shapes.

| Coefficient x^n term | Fore-Aft mode 1 | Fore-Aft mode 2 | Side-side mode 1 | Side-side mode 2 |
|---------------------------|--------------------|--------------------|---------------------|---------------------|
| $n = 2$ | -1.953 | 7.452 | -1.879 | 5.8085 |
| $n = 3$ | 12.959 | 7.022 | 12.580 | 7.949 |
| $n = 4$ | -24.117 | -21.354 | -23.396 | -21.468 |
| $n = 5$ | 21.167 | 13.382 | 20.538 | 15.052 |
| $n = 6$ | -7.057 | -5.503 | -6.844 | -6.342 |

4.6 New inputs

Most input changes are done to set the conditions for each separate simulation case. Other changes are done permanently, specifically structural parameters. Some of these input changes are included in Table 12. Some others are included in Appendix A.

ElastoDyn

Table 12: ElastoDyn input changes

| Parameter | unit | Old value | New value |
|-------------------------------------|---------------------|---|-----------|
| Height of tower above MSL | [m] | 129.495 | 135.896 |
| Subplatform Center of mass | [m] | -113.08 | -112.87 |
| Subplatform mass including ballast | [kg] | 3.655e+07 | 3.845e+07 |
| Subplatform Ixx about CoG | [kgm ²] | 5.590e+10 | 5.597e+10 |
| Subplatform Iyy about CoG | [kgm ²] | 5.590e+10 | 5.597e+10 |
| Subplatform Izz about CoG | [kgm ²] | 1.828e+09 | 1.905e+09 |
| Initial conditions & displacements: | | Change to reduce startup transients and to avoid emergency shutdown at startup. | |

5 SIMULATION RESULTS

The characteristics of the Utsira model is shown by analysis of OpenFAST simulation results. The following simulations are performed:

1. No external forcing - equilibrium
2. Decay tests - natural frequencies
3. Uniform wind and stochastic waves
4. Turbulent wind and stochastic waves

The first two listed above are run with the original mooring layout of WindCrete at a 200 m depth with updated tower and ballast, as well as with the complete new design. This is done to see if the system properties change as expected in relation to the model adjustments. The last two listed above is done to check model characteristics and stability for wind speeds below rated, close to rated and above rated.

5.1 Platform equilibrium

Mooring layout from WindCrete

Static equilibrium for the Utsira tower is simulated in a 1500 second time series with initial conditions of zero in all six translational and rotational degrees of freedom. The position of the platform at equilibrium is calculated as the mean of the time series, starting at 200 seconds. The results are presented in Table 13.

The new static equilibrium changes as expected, considering the alterations of the tower. The weight of the tower is reduced by approximately 2/3, and this weight is added as ballast in the support structure, just a few meters above the center of gravity. The platform pitch is thus reduced, as expected. Consequently, the horizontal offset at the MSL is reduced, as the new platform follows the global vertical z-axis closer compared to the WindCrete model. This results in a reduced surge displacement. A similar geometrical argument can be made to explain the change of heave. As platform pitch is reduced, heave consequently increases.

New mooring layout

Static equilibrium with the new mooring layout implemented is simulated in the same fashion as described in the paragraphs above. The results are presented in Table 13.

Table 13: Static equilibrium - WindCrete mooring layout

| Surge [m] | Sway [m] | Heave [m] | Roll [deg] | Pitch [deg] | Yaw [deg] |
|-----------------------------------|----------|-----------|------------|-------------|-----------|
| WindCrete | | | | | |
| -1.01 | 0.0 | -0.16 | 0.0 | -0.64 | 0.0 |
| Utsira - WindCrete mooring layout | | | | | |
| -0.66 | 0.0 | 0.01 | 0.0 | -0.42 | 0.0 |
| Utsira - New mooring layout | | | | | |
| -0.69 | 0.0 | -0.10 | 0.0 | -0.42 | 0.0 |

The new mooring layout has a limited impact on the static equilibrium. It has the same symmetry as the WindCrete layout, and so the changes should be small. Some minor differences are expected, as the fairlead tensions increase with the new water depth. I have removed some ballast to compensate for the fairlead tensions. I did not calculate this mass with high accuracy, and so the removed mass is not accurately proportional to the increased vertical load. I made a rough estimation of the added weight of chain carried by the platform when increasing depth by 50 m, considering the static layout in Figure 19. The lower bound of applied horizontal force in this plot relates to platform equilibrium, and so I find an approximate length of the catenary line in the bottom 50 m visually. Thus, the greatest difference is found in heave. Small changes in vertical load causes great changes in heave, as the water plane area of the spar design is small. Still, I find the new heave displacement in static equilibrium acceptable.

5.2 Decay tests

The next step of verifying the Utsira platform is to recreate the decay tests presented in the WindCrete report [Mahfouz et al., 2020]. I have done separate decay tests for surge, heave, pitch and yaw, with the goal of finding the natural frequencies of these motions for the Utsira tower. Each test is initiated by offsetting only one translational or rotational degree of freedom. Surge and heave have an initial offset of 5 m respectively for their separate decay test. Pitch and yaw have an initial offset of 5 degrees for their separate simulation. The oscillation frequencies are determined visually from plots of the Fast Fourier transforms of the time series. I then determine the oscillation frequencies visually. The simulation duration is set to 500 s, which is adequate to find accurate frequencies, with exception of the surge frequency, which is very low. For this reason, I use a 3800 s surge decay simulation. These decay simulations are done for both the WindCrete and the Utsira mooring layout. Natural frequencies are then compared to the WindCrete spar in Table 14. The natural frequencies of the WindCrete model is stated in Table 5-9 in the COREWIND report [Mahfouz et al., 2020, p.26].

Table 14: Decay Simulations

| Model | Natural Frequency [Hz] | | | Natural Period [s] | | |
|-------|------------------------|-----------|--------|--------------------|-----------|--------|
| | WindCrete | Utsira | | WindCrete | Utsira | |
| | | WindCrete | Utsira | | WindCrete | Utsira |
| Surge | 0.01221 | 0.0126 | 0.0092 | 81.90 | 79.37 | 108.70 |
| Heave | 0.03052 | 0.0300 | 0.0300 | 32.77 | 33.33 | 33.33 |
| Pitch | 0.02441 | 0.0320 | 0.0316 | 40.97 | 31.25 | 31.65 |
| Yaw | 0.09155 | 0.0900 | 0.0760 | 10.92 | 11.11 | 13.16 |

The tower reconstruction has a relatively small impact on natural frequencies of the translational and rotational DoFs, except for pitch. The natural period of pitch is reduced by almost 25%. This reduction is as expected, as mass has been shifted from the tower to the internal of the support platform. Lowering the global center of gravity further increases the metacentric height, resulting in a more stable platform. The pitch decay test clearly demonstrates how platform motions are coupled, see Figure 25. The main peak is the surge natural frequency. The second peak matches the pitch frequency of 0.0320 Hz. This is caused by the center of rotation being vertically offset from the global origin.

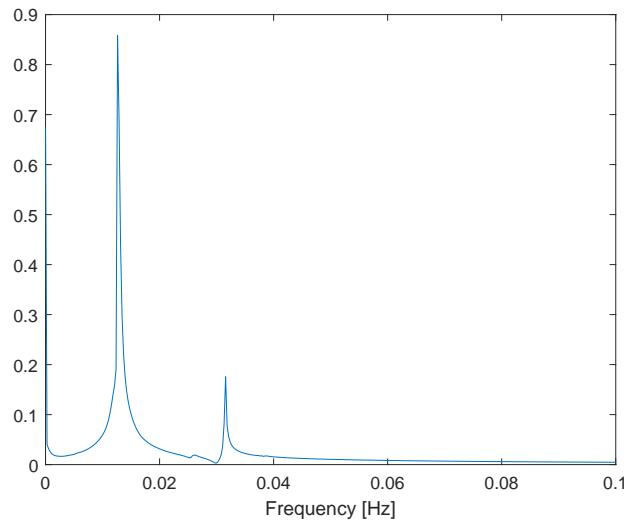


Figure 25: Natural frequency of surge, with coupled pitch frequency. This data is from a surge decay test, using the Utsira tower and support platform, with the WindCrete mooring layout.

The transition to a new mooring layout causes some changes to the natural frequencies. First, the surge frequency is lowered. This is expected, as the surge stiffness is reduced when extending the length of the mooring line. To check this transition, we can look at the relation between the square root of the old surge stiffness divided by the new surge stiffness:

$$\sqrt{\frac{5.0523e + 05}{2.8142e + 05}} = 1.34 \quad (5.1)$$

This value is reflected in the ratio between the new and the old natural periods:

$$\frac{108.70}{79.37} = 1.37 \quad (5.2)$$

This shows that the change in surge natural frequency is proportional to the change in surge stiffness of the mooring system. The natural frequency of yaw is also decreased when altering the mooring layout. The restoring force in yaw is mainly provided by the mooring line through the delta line. I have kept the delta line as is when transitioning to the new layout, extending only the main chain section. Thus, the yaw stiffness is affected by the change in surge stiffness. As the platform yaws, a greater part of the tension from the main chain length is channelled through one of the delta lines, which then provides the restoring force. In this fashion, yaw stiffness is an extension of the surge stiffness, thus I expect yaw stiffness to be affected similarly to surge stiffness when adjusting mooring properties without any changes to the delta lines. All considered, I expect the changes in platform stability in production under various environmental conditions to be relatively small. This is further investigated in Section 5.3.

5.2.1 Tower FA and SS frequencies through OpenFAST

The objective of this thesis is partly to get familiarized with the OpenFAST tool. OpenFAST allows the user to input a wide range of parameters, including restricting specific DoFs. This section is included as a small example of something that can be investigated by manipulating the model input.

I wish to investigate the Fore-Aft and Side-to-Side tower displacements as output from OpenFAST and see if the output coincides with the expected tower mode frequencies found using BModes. I run 500 s simulations with no translational and rotational degrees of freedom on the new design. I set the initial displacement of the tower top Fore-Aft and the Side-to-Side displacements to 5 m respectively. I then use an FFT function on the output in MATLAB to find the natural frequencies of the first tower modes, as described in Section 5.2. Each time step in the OpenFAST simulation is 0.01 s, though the output frequency of the simulation is 10 Hz. These are compared to the natural frequencies found in BModes in Table 15.

Table 15: Tower natural frequencies of the first mode. Comparison between BModes and OpenFAST output.

| Description | Frequency with OpenFAST output [Hz] | Frequency with BModes output [Hz] |
|------------------------------|-------------------------------------|-----------------------------------|
| 1 st Side-to-Side | 0.47 | 0.46 |
| 1 st Fore-Aft | 0.46 | 0.46 |

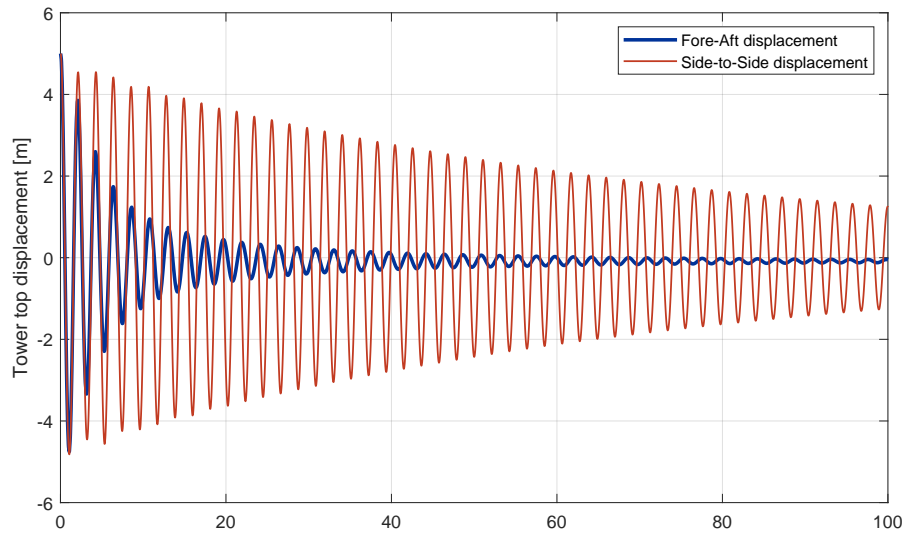


Figure 26: Tower top displacements

Figure 26 shows how the vibrations are dampened much faster in the Fore-Aft direction than the Side-to-Side direction. The following discussion is an effort to understand why this damping occurs in the Fore-Aft direction. In these simulations, the flapwise and edgewise blade mode DoFs are free to move, and the blade pitch angle is 0 degrees. I repeat the simulation while restricting flapwise and edgewise blade DoFs and pitching the blades 90 degrees. I then investigate the impact each parameter has on the Fore-Aft displacement damping.

First, I run simulations with flapwise and edgewise blade mode DoFs disabled. This means that the blades stay rigid throughout the simulation, thus we have no out-of-plane displacements or in-plane displacements for the blades. This has a significant effect on the damping of the tower Fore-Aft displacements, as shown in Figure 27. The output now resembles the Side-to-Side displacement time series, but not exactly. This indicates that there are several parameters that affect the damping rate.

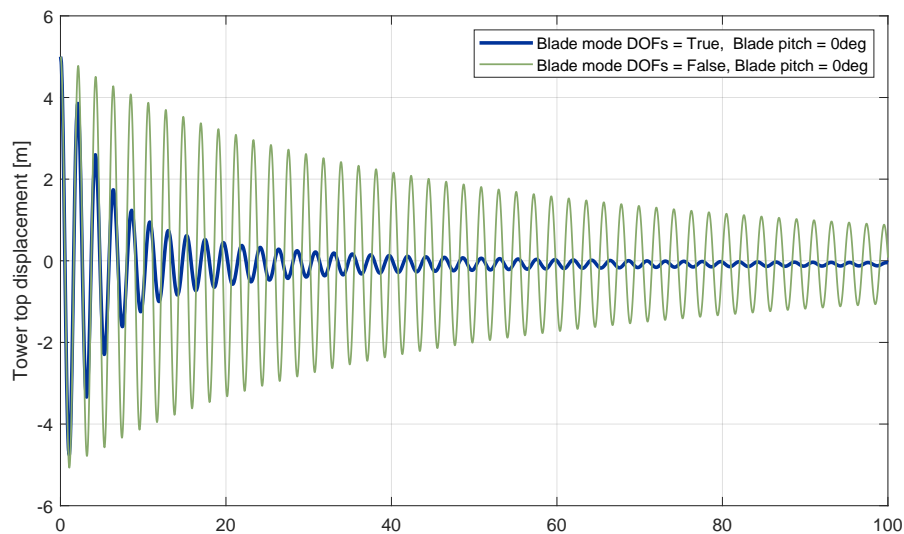


Figure 27: Tower top fore-aft displacements. This graph demonstrates the damping impact of allowing flapwise and edgewise DoFs for the blades.

Second, I run simulations with an initial blade pitch of 90 degrees. I allow flapwise and edgewise blade DoFs. The blade pitch is locked at a constant 90 degrees, which also is called feathered position. This is controlled by the ServoDyn submodule, where the final pitch of the blades is set to 0 degrees originally. This simulation requires changing the final pitch angle to 90 degrees. Intuitively, the drag from the blades moving through air will have a dampening effect on the system. Feathering the blades minimizes this drag, allowing the tower to vibrate with less resistance from the air. Figure 28 shows how the blade pitch affects the damping rate of tower top displacements. The effect of blade pitching is significant, though the total damping rate seems to be affected by both bending and pitch of the blades.

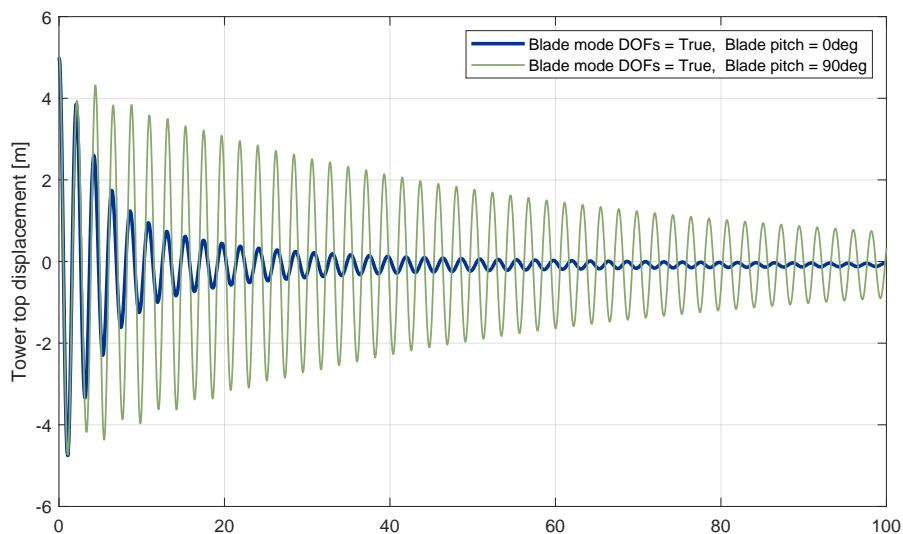


Figure 28: Tower top fore-aft displacements. This graph demonstrates the damping impact of blade pitch.

5.3 Stability at different environmental conditions

The next step is to see if the new model behaves as expected when the wind turbine is operating. Simulations are performed both with steady wind and with more realistic conditions with turbulent wind. Waves are modelled by the JONSWAP spectrum in both mentioned simulations. I will examine the impact of the adjustments I have done, and try to discover any challenges with the new design. The controller is crucial for platform stability. The WindCrete team has adapted the controller from the bottom-fixed IEA reference turbine, but they have not optimized this new controller for the whole power production spectre. In addition, I have done further adjustments to tower, subplatform and mooring lines. I will investigate if the controller is able to handle these changes, or if controller optimization is required.

I choose to run simulations for four wind speeds. First, I run simulations with 8 m/s wind, as this is below rated wind speeds. I include this to see how variable-speed torque control affects system stability. Second, I run simulations with wind speeds of 13 m/s. This wind speed is above the rated wind speed of 10.59 m/s, but in the case of turbulent wind, I expect to see some fluctuations where the wind speed drops below rated. This gives insight into how the system behaves around the rated wind speed. I give special attention to the output of these simulations in Section 5.3.1. Third, I run simulations with 18 m/s wind. This is well above rated wind speed, and I include this to see how the wind turbine behaves under high environmental loads. Fourth, I run simulations with 35 m/s wind as an extreme case. For this simulation, the rotor blades are feathered, and the wind turbine generator is turned off. Here I investigate how the model behaves in high winds and extreme waves, in an idling state. I run all simulations for both steady and turbulent wind, with the exception of 35 m/s, where I only use turbulent wind. The steady wind simulations are mostly included in Appendix B, with the exception of 13 m/s steady wind. This steady wind case is discussed in Section 5.3.1.

I find realistic wave input for each wind speed, which is based on a Norwegian 10 km Reanalysis Archive (NORA10) dataset [Reistad et al., 2011]. This dataset contains measurements of wind and waves at a station with latitude-longitude coordinates of [59.27N, 04.39E]. This location is approximately 25 km west of Utsira island. The dataset contains measurements every three hours from 1957 to 2020. It gives wind speeds from a height of 10 m and up to a height of 150 m [Furevik and Haakenstad, 2012]. I search the database for all measurements of 8, 13 and 18 m/s wind speed respectively at approximately the hub height. I then find the average wind sea H_s for each wind speed, together with an associated average T_p . This gives a simple, yet somewhat realistic average wave spectre for each wind speed when using the JONSWAP spectrum, see section 2.4.1. For the extreme case, I search the dataset for the maximum wind sea H_s , and use the associated value for T_p and wind speed.

5.3.1 Turbulent wind and waves

In this section, I discuss some of the simulations done with different environmental conditions. All mean and max values of simulation parameters presented in the following sections are found from the last 1800 s of the time series, to avoid the effect of transients. This is further discussed in the paragraph about 13 m/s steady wind.

8 m/s turbulent wind

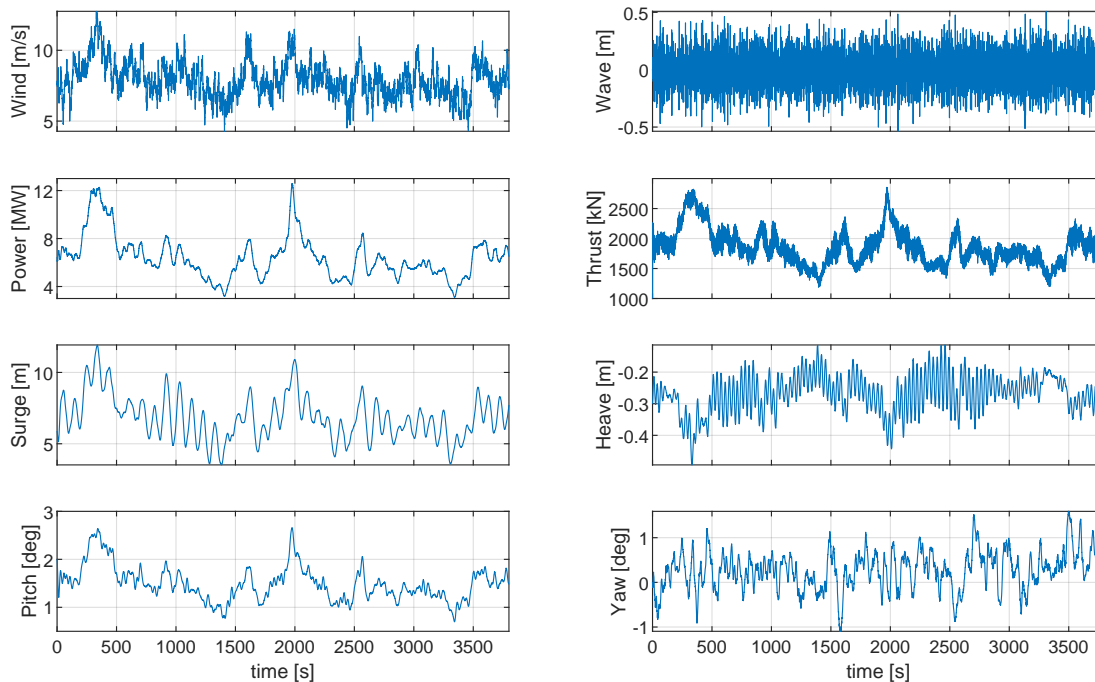


Figure 29: OpenFAST simulation for 8 m/s turbulent wind, with inputs as described in Table 16.

Figure 29 shows some characteristics of the Utsira model under wind speeds below rated. Here, the wind turbine controller operates with a variable speed torque control, to maximize power output. Because of this, The blades have a constant pitch of zero degrees. As a consequence, the variations in platform pitch, surge, and power output mirrors the variations in thrust applied to the rotor. At approximately 2000 s there is a spike in the thrust curve. At this moment, the wind speed is above the rated wind speed, but the blades stay at a constant pitch of zero degrees. This causes a spike in thrust reaching values above the rated thrust value of 2.4 MN. Considering this, I expect the platform pitch to reach an extreme value, but it still does not exceed three degrees. This further indicates that the platform stability is increased beyond necessary. Of course, this simulation is done with a JONSWAP spectrum of waves with a H_s of 0.6 m. Running this simulation with more extreme waves would likely result in higher pitch values.

Table 16: Some input parameters and initial values for 8 m/s Turbulent wind.

| Parameter | Initial/input value | Unit |
|----------------------|---------------------|-------|
| Mean wind | 8.0 | [m/s] |
| Turbulence intensity | 0.15 | (-) |
| Power Law exponent | 0.2 | (-) |
| Rotor speed | 5.7 | [rpm] |
| Blade pitch | 0.0 | [deg] |
| Wave H_s | 0.6 | [m] |
| Wave T_p | 4.2 | [s] |
| Surge | 5.9 | [m] |
| Pitch | 2.0 | [deg] |
| Heave | -0.3 | [deg] |
| Yaw | 0.0 | [deg] |

Table 17: Means and ranges of motions for the 8 m/s turbulent wind simulation.

| Surge maximum [m] | Surge average [m] | Pitch maximum [deg] | Pitch average [deg] | Yaw maximum [deg] | Yaw average [deg] |
|-------------------|-------------------|---------------------|---------------------|-------------------|-------------------|
| 10.92 | 6.63 | 2.80 | 1.44 | 1.61 | 0.33 |

13 m/s steady wind

The steady wind simulation is not a realistic case, but is included here to investigate the effect of initial values on start-up transients. Also, this simulation gives an indication of power output stability, and the extent of translational and rotational movements. Step wind simulations are available for the WindCrete model in the CoreWind report [Mahfouz et al., 2020, p.27], and so I can compare the Utsira model with these simulations. Table 18 describes some input parameters for this simulation.

Table 18: Some input parameters and initial values for 13 m/s steady wind.

| Parameter | Initial/input value | Unit |
|--------------------|---------------------|-------|
| Mean wind | 13.0 | [m/s] |
| Power Law exponent | 0.06 | (-) |
| Rotor speed | 7.54 | [rpm] |
| Blade pitch | 8.38 | [deg] |
| Wave H_s | 1.86 | [m] |
| Wave T_p | 6.97 | [s] |
| Surge | 6.5 | [m] |
| Pitch | 2.5 | [deg] |
| Heave | -0.3 | [deg] |
| Yaw | -0.2 | [deg] |

Figure 30 visualizes the start-up transients that occur when initial values do not match mean values for the particular load case. This effect is especially prominent in surge. I used initial values found from simulation of the WindCrete model, and so I would expect pronounced start-up transients. I run a new simulation for 13 m/s steady wind, to demonstrate the impact of initial values on transients. I use values provided in Table 19 as new initial values. I also calculate mean blade pitch and rotor rpm, together with sway, heave and roll displacements.

Though Figure 30 shows shorter start-up transients when applying more appropriate initial values, we still see the effect in surge, especially in the first 1000 s of simulation. Also, the new initial yaw rotation has suppressed almost all start-up transients, though the extent of yaw rotation is small already in the original simulation shown in Figure 30. I calculate the range of motions for the simulation that has appropriate initial values, while still suppressing the first 1800 s. The changes of mean values are insignificant, compared to Table 19. This indicates that it is sufficient to ignore the first 1800 s of the time series to account for start-up transients.

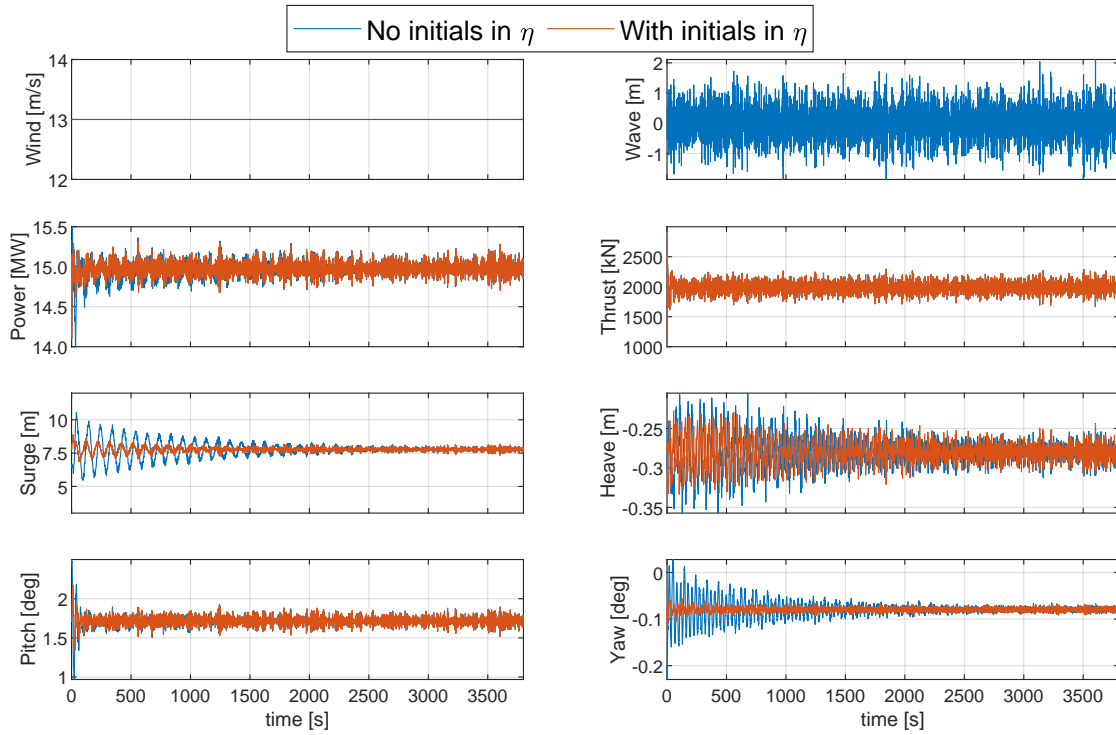


Figure 30: OpenFAST simulations with the initial values as described in Table 18, compared with initial values for rotational and translational DoFs set to zero.

Table 19: Means and ranges of motions for the 13 m/s steady wind simulation.

| Surge maximum [m] | Surge average [m] | Pitch maximum [deg] | Pitch average [deg] | Yaw maximum [deg] | Yaw average [deg] |
|-------------------|-------------------|---------------------|---------------------|-------------------|-------------------|
| 8.29 | 7.78 | 1.90 | 1.72 | -0.10 | -0.08 |

13 m/s turbulent wind

Table 20: Some input parameters and initial values for 13 m/s turbulent wind.

| Parameter | Initial/input value | Unit |
|----------------------|---------------------|-------|
| Mean wind | 13.0 | [m/s] |
| Turbulence intensity | 0.12 | (-) |
| Power Law exponent | 0.2 | (-) |
| Rotor speed | 7.54 | [rpm] |
| Blade pitch | 8.38 | [deg] |
| Wave H_s | 1.86 | [m] |
| Wave T_p | 6.97 | [s] |
| Surge | 6.5 | [m] |
| Pitch | 2.5 | [deg] |
| Heave | -0.3 | [deg] |
| Yaw | -0.2 | [deg] |

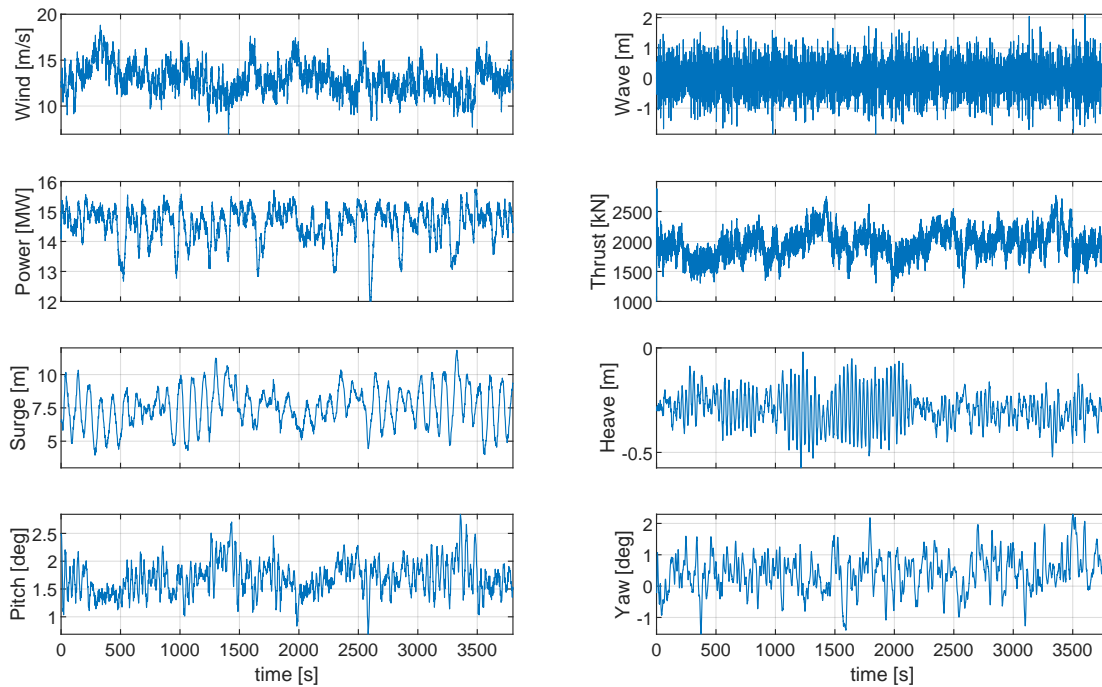


Figure 31

Table 21: Means and ranges of motions for the 13 m/s turbulent wind simulation.

| Surge maximum [m] | Surge average [m] | Pitch maximum [deg] | Pitch average [deg] | Yaw maximum [deg] | Yaw average [deg] |
|-------------------|-------------------|---------------------|---------------------|-------------------|-------------------|
| 11.83 | 7.63 | 2.84 | 1.71 | 2.29 | 0.49 |

We see large variations in power output in Figure 31. This is expected as the model uses a constant torque controller at above rated wind speeds. Figure 32 shows how the generator torque is limited at an upper bound of approximately 19.62×10^4 Nm. This limit is defined in the torque control input section of the DISCON.IN file, which is a required input file for the ServoDyn submodule. Figure 32 shows how the dips in generator torque is correlated with spikes in rotor rpm. Power, P is the product of torque, τ and angular velocity, ω :

$$P = \tau\omega \quad (5.3)$$

This relation is evident in Figure 32. At around 2000 s there is a peak in rotor rpm. At the same time, there is a dip in torque, τ , which allows the power output to remain relatively constant. Also, at around 500 s there is a dip in rotor rpm. We then see a dip in power, as the controller does not allow torque to increase past the upper limit. As a consequence of this constant torque controller type, the power output fluctuates more around the rated value of 15 MW.

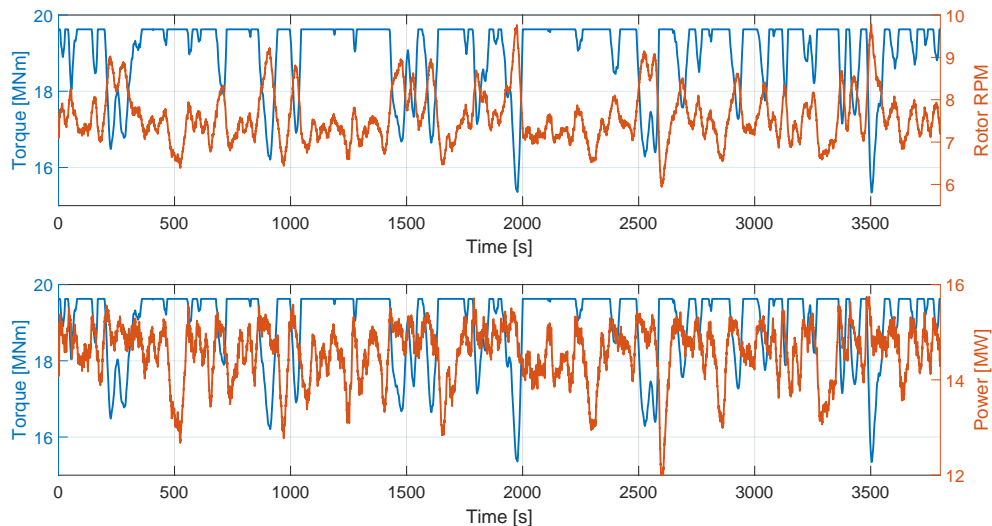


Figure 32: Torque output for the 13 m/s turbulent wind simulation.

The rotor rpm fluctuates much, with sharp peaks whenever the torque is reduced. During these peaks, the rotor rpm reaches speeds far higher than the rated rotational frequency of 7.56 rpm. The reason for this becomes evident when taking a closer look at output data during a dip in torque, as seen at around 2000 s in Figure 32. Around this point in

the time series, there is a sharp spike in rotor rpm. Figure 33 shows how there is an increase in wind speed from approximately 1900 s to 1950 s. Before this increase starts, the rotor rpm is approximately the rated value of 7.56 rpm. As the wind picks up in speed, the rotor rpm increases to approximately 9.5 rpm. This indicates that the blades have a too small pitch angle, and that the blade pitch angle changes too slowly to counteract the sharp increase in wind speed. The blade pitch angle, shown as a solid red line in Figure 33, has a maximum pitch rate of 0.0349 rad/s, or approximately 2 deg/s. This limit is also user-specified in the DISCON.IN file corresponding to the ServoDyn submodule. However, Figure 33 shows that the blade pitch angle changes at a maximum of approximately 0.07 deg/s, which is nowhere near the 2 deg/s limit. Of course, there may be good reasons for keeping the pitch rate lower than 2 deg/s, but the theory behind the pitch controller is beyond the scope of this thesis. This indicates that the controller might need some optimization. CoreWind states that controller optimization is scheduled as a future project [Mahfouz et al., 2020, p.24]. In fact, output from the WindCrete model show the same characteristics as discussed here, e.g. in Figure 5-16 in the WindCrete report [Mahfouz et al., 2020, p.30].

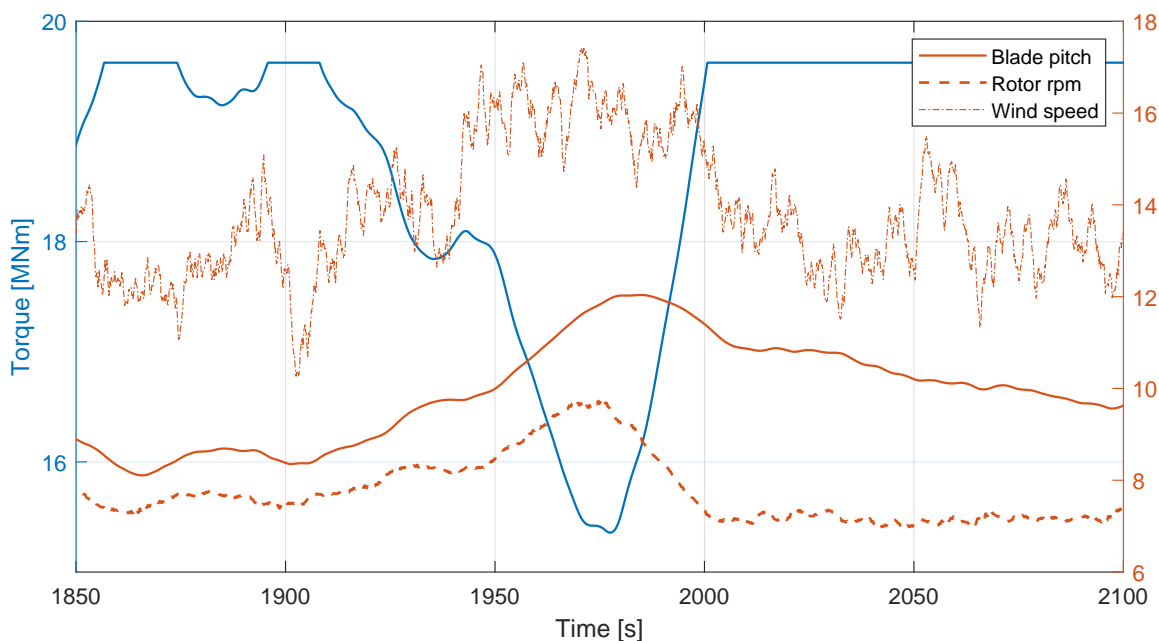


Figure 33: A closer look at the relation between wind speed [m/s], blade pitch [deg], rotor rpm [-] and torque. This figure is a close-up around 2000 s of the time series shown in Figure 32.

One of the design criteria to achieve structural integrity of the tower was to ensure that the bending stress throughout the tower did not exceed values from the bottom fixed reference tower. To ensure this, I applied the rated thrust of 2.4 MN to the tower top, with a pitch angle of six degrees, see Section 4.2.2. From the 13 m/s turbulent wind simulation, I find the mean thrust to be approximately 1.98 MN. This fits well what I expect from the trust curve provided in the definition of the IEA reference turbine, seen in Figure 34. Here it is important to note that the WindCrete controller is modified, and so the rotor thrust curve for the controller I use is not necessarily identical to the one

presented here. Nevertheless, this figure gives a good indication of expected behaviour. The maximum platform pitch angle through the time series is approximately 2.84 degrees, see Table 21. The wind speeds of this simulation are relatively close to the rated wind speed of 10.59 m/s. The thrust is approximately 2770 kN around the time step of maximum platform pitch angle. Figure 34 also shows how rotor thrust decreases as wind speeds increase past rated wind speed.

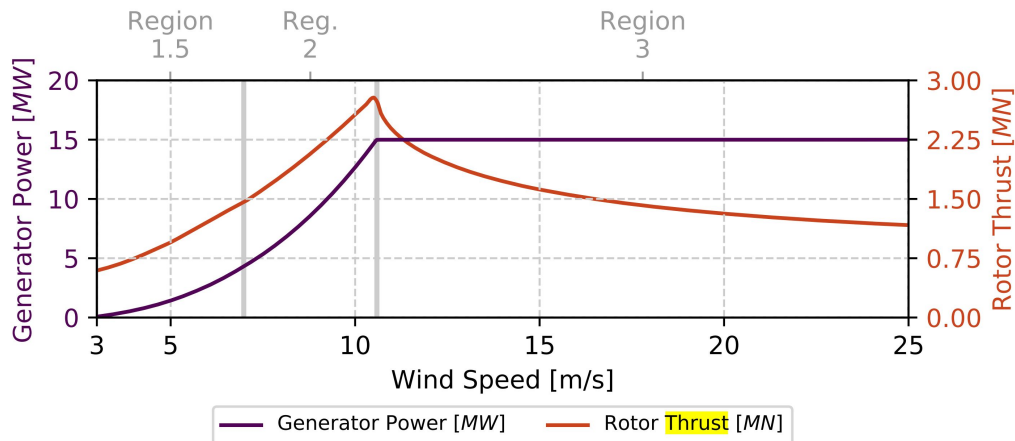


Figure 34: Rotor thrust curve for the IEA 15 MW reference turbine, from [Gaertner et al., 2020b, p.19].

Analysis of output data indicates that using bending stress from six degrees static platform pitch gives a conservative design. Table 21 shows a maximum platform pitch value of 2.84, which is very similar to the 8 m/s turbulent wind simulation, see Table 17. However, some considerations must be done. The wave input for this simulation is a JONSWAP spectre using an H_s of 1.86 m. The site will experience much larger waves, also for a relatively low wind speed of 13 m/s. Further work would be required to investigate how rougher seas would affect platform characteristics. Even though there might be some challenges when it comes to the controller, the overall stability of the model seems to be adequate, considering the few load cases done in this work.

18 m/s turbulent wind

Table 22: Some input parameters and initial values for 18 m/s turbulent wind.

| Parameter | Initial/input value | Unit |
|----------------------|---------------------|-------|
| Mean wind | 18.0 | [m/s] |
| Turbulence intensity | 0.11 | (-) |
| Power Law exponent | 0.2 | (-) |
| Rotor speed | 7.54 | [rpm] |
| Blade pitch | 15.56 | [deg] |
| Wave H_s | 3.43 | [m] |
| Wave T_p | 8.62 | [s] |
| Surge | 4.6 | [m] |
| Pitch | 1.7 | [deg] |
| Heave | -0.3 | [deg] |
| Yaw | -0.4 | [deg] |

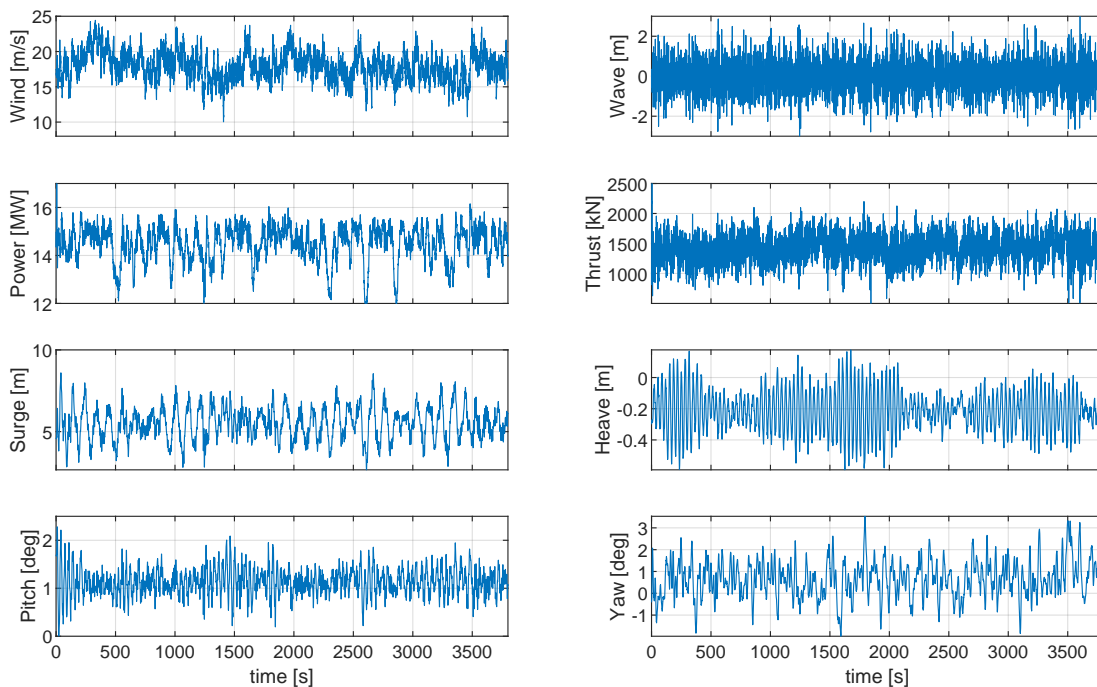


Figure 35: OpenFAST simulation output with input as described in Table 22.

The output from simulation with 18 m/s turbulent wind in Figure 35 shows similar characteristics as the 13 m/s turbulent wind simulations. The power output fluctuates

around 15 MW, showing the same sharp dips periodically. However, both average and maximum values of platform surge and pitch are reduced, see Table 23. This can be explained by the reduced thrust force. The average thrust force is 500 kN below the value from the 13 m/s turbulent wind simulation. Also, the Hs in this simulation is 3.43 (see Table 22), which is almost double the value from the 13 m/s simulations. This indicates that the response to wave loads is small compared to the response induced by the wind, at least for relatively small wave heights. The effect of extreme waves is discussed in the next section.

Table 23: Means and ranges of motions for the 18 m/s turbulent wind simulation.

| Surge maximum [m] | Surge average [m] | Pitch maximum [deg] | Pitch average [deg] | Yaw maximum [deg] | Yaw average [deg] |
|-------------------|-------------------|---------------------|---------------------|-------------------|-------------------|
| 8.55 | 5.53 | 1.95 | 1.14 | 3.32 | 0.72 |

35 m/s turbulent wind

I include a simulation with 35 m/s turbulent wind and extreme waves to investigate how wave loads affect the model characteristics. I found the wind and wave parameters by searching the NORA10 dataset for the highest wind sea Hs, and used the associated Tp.

Table 24: Some input parameters and initial values for 35 m/s turbulent wind.

| Parameter | Initial/input value | Unit |
|----------------------|---------------------|-------|
| Mean wind | 35.0 | [m/s] |
| Turbulence intensity | 0.10 | (-) |
| Power Law exponent | 0.2 | (-) |
| Rotor speed | 0.0 | [rpm] |
| Blade pitch | 90.0 | [deg] |
| Wave H _s | 14.2 | [m] |
| Wave T _p | 14.9 | [s] |
| Surge | 4.6 | [m] |
| Pitch | 1.7 | [deg] |
| Heave | -0.3 | [deg] |
| Yaw | -0.4 | [deg] |

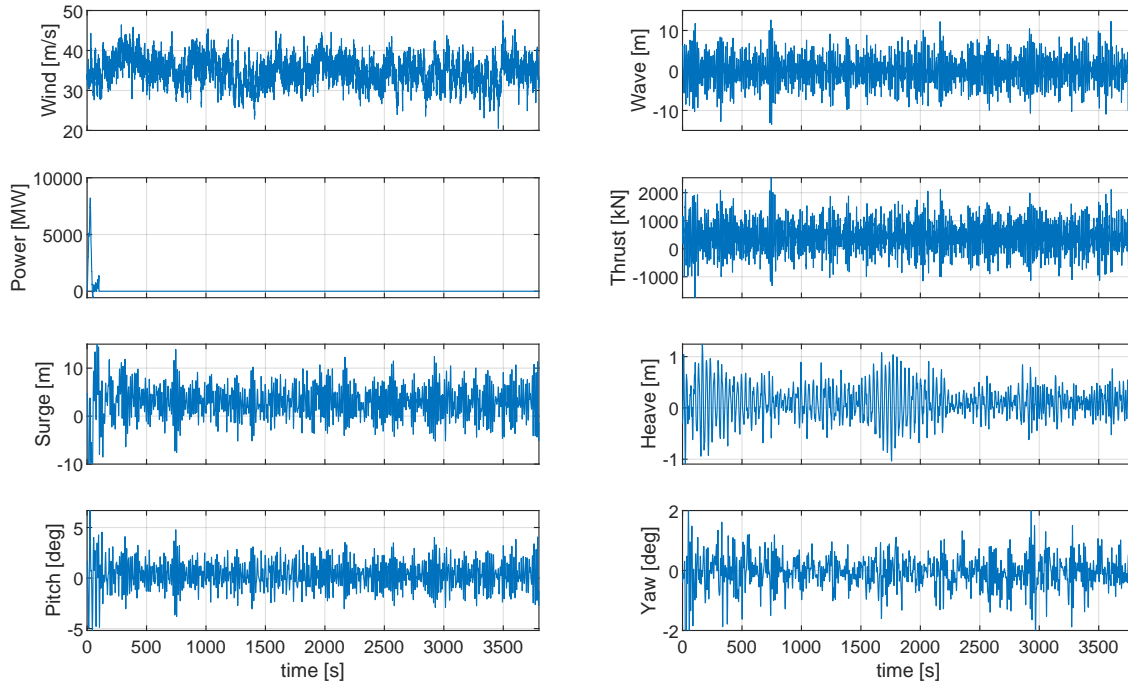


Figure 36: OpenFAST simulation output with input as described in Table 24. The wind turbine is in an idling state in this simulation.

Figure 24 shows that while idling, the platform pitch range of motion is much larger. The average platform pitch is now 0.33 deg, with a maximum value of 4.07 deg. Platform surge reaches a maximum of 12.39 m, which is more than in any other simulation done with the Utsira model. This shows that the wave loads can cause significant platform displacements. The maximum platform pitch is still well under the six degrees static pitch used for bending stress calculations in Section 4.2.2.

Table 25: Means and ranges of motions for the 35 m/s turbulent wind simulation.

| Surge maximum [m] | Surge average [m] | Pitch maximum [deg] | Pitch average [deg] | Yaw maximum [deg] | Yaw average [deg] |
|-------------------|-------------------|---------------------|---------------------|-------------------|-------------------|
| 12.39 | 2.94 | 4.07 | 0.33 | 2.09 | 0.07 |

6 SUMMARY AND CONCLUSION

The objective of this thesis was to adapt an OpenFAST model named WindCrete, created by CoreWind. The aim of model adaptations was to create an offshore wind turbine model in OpenFAST, designed for the more extreme environmental conditions of the Utsira site.

The adaptation work was an iterative process, starting with modifications to the tower structure. To comply with structural requirements given by the IEC standards, I increased the tower height to 135.869 m. I chose to model the tower as a steel structure, thus making it more structurally similar to the tower used in the IEA reference wind turbine model. I used this reference wind turbine tower as a benchmark, and required the bending stress throughout the adapted tower not to exceed the benchmark values. This bending stress is a result of both a thrust force applied to the wind turbine blades, and the offset weight of the RNA from the central axis of the tower. In addition, the adapted tower was statically pitched at an angle of six degrees, to include the weight of the heeling tower in bending stress calculations. This appears to be a somewhat conservative approach, as discussed in Section 5.3.1. Here, simulation outputs show that the maximum platform pitch is kept below three degrees, even for peaks in the thrust force above the rated value. However, I later found it necessary to increase the stiffness of the tower even further, to avoid unwanted resonance between tower vibration and the rotating frequency of the rotor.

The adjustments done to the tower and mooring system causes significant changes to the equilibrium heave position of the floating platform. The mass of the internal ballast in the spar support platform was adjusted to compensate for the reduced weight of the tower and increased vertical forces from the new mooring layout. The equilibrium heave position was restored by adding approximately 1894.8 tonnes of ballast just below the global center of mass of the floating platform. This causes the global center of mass to shift downwards, which again leads to a higher metacentric height. The metacentric height is a measure of spar platform stability, and simulations show that platform stability is increased, as expected.

The mooring layout was adjusted to fit a new water depth of 250 m, which is within the range of depths found within the Utsira site. I chose a combination of extending the main mooring length and extending the anchor radius to compensate for the increased water depth. I required a safety margin of at least 10% of the mooring line length between the anchor and the touchdown point where the mooring line meets the seafloor. Simulations indicate that the final mooring layout presented in Table 8 is sufficient to avoid uplifting forces in the anchor points.

I calculated the tower modes of the adjusted tower using BModes. This tool models the tower as an Euler-Bernoulli beam, with the RNA and the spar support platform as end attachments. The support platform is modelled as a rigid body, with the tower cantilevered at the top. Thus, BModes requires support platform properties as input, including an added mass matrix, a hydrostatic stiffness matrix and a mooring stiffness matrix. The first iteration gave tower mode natural frequencies too close to the rotational frequencies of the blades, which required a new iteration of adjustments, as

described in the flowchart in Figure 8. In fact, I conducted several iterations of the adjustment process to arrive at a final model design.

After the final iteration of adjustments, I did a range of simulations to investigate model characteristics and stability. This included decay tests for each separate translational or rotational DoF, and static equilibrium simulations. The equilibrium simulation gave expected results, showing relatively small differences in equilibrium position, compared to the WindCrete model. I see a slight decrease in equilibrium pitch angle caused by the increased metacentric height. From the decay simulations, I saw a significant reduction in the natural period of pitch, which also agrees with expectations. The greatest change in natural period is found in surge, with an increase of well over 30%. Further investigation showed that this is as expected considering the relation between the old and new surge stiffness values. Even though the adjustments caused some significant changes to the natural periods, the predesign basis from the WindCrete project is still fulfilled.

I then investigated model characteristics under four environmental scenarios. The first scenario was using a below rated wind speed of 8 m/s. Here I see a large variation in power output. Due to turbulence, the wind speed periodically increases past the rated wind speed, causing peaks in thrust force applied to the rotor. The simulation showed how the turbine reacts to the applied thrust, and I recognize the shape of the thrust curve especially well in pitch, surge and power.

The second scenario was using a wind speed of 13 m/s, which is just above rated wind speed. The steady wind scenario highlighted the effect of start-up transients. Choosing appropriate initial conditions greatly reduced both the magnitude and duration of these transients. Special focus was given to the simulation with 13 m/s turbulent wind, a characteristic wave height of 1.86 m, and a peak return period of 6.97 s. Here I investigated the effect of using constant torque control, and highlighted issues with sharp spikes in rotor rpm. The highly turbulent wind just over rated wind speed causes thrust forces well above rated value, but the overall stability of the floating wind turbine is not compromised.

The third and fourth environmental scenario was using 18 m/s and 35 m/s turbulent wind, both with stochastic waves. The 35 m/s scenario was included as an extreme case with stochastic waves with a H_s of 14.2 m. The overall stability of the Utsira model seems adequate when considering the output of these simulation cases.

Overall, I have created an OpenFAST model of a floating spar wind turbine, by making adjustments to the WindCrete project by CoreWind. The final Utsira model complies with the structural requirements that the adjustments are based upon. The model holds up well in the range of simulations done to test the stability and investigate model characteristics. However, most of the adjusted model components could be optimized, as I have chosen quite large safety margins for most of the design requirements. Also, the model should be tested much more thoroughly to get a more complete design analysis for all realistic load cases. This could be done following the procedures used in the WindCrete project.

7 FUTURE WORK

- Optimization of the platform tower and substructure
- Optimization of the mooring layout, including site-specific anchor positioning
- Optimization of the wind turbine controller
- A complete, site-specific load analysis with accurate wave- and wind data
- Further exploring the OpenFAST tool and the possibilities it presents, such as wind farm simulation

References

- Iea 15mw github repository. Git repository at <https://github.com/IEAWindTask37/IEA-15-240-RWT>, 2020. This repository contains the model data for the 15-MW offshore reference turbine developed within IEA Wind Task 37.
- Mooring line computation programme. Personal correspondence with author F. G. Nielsen, 2021. MatLab routine for computing mooring line geometry and restoring characteristics for single lines and a system of lines. Several segments with different weight and length may be connected.
- S. Afewerki, A. Aspelund, Ø. Bjørgum, J. Hanson, A. Karlsen, A. Kenzhagaliyeva, H. E. Normann, M. Steen, and E. A. Sæther. *Conditions for Growth in the Norwegian Offshore*. 2019. ISBN 9788293198307.
- Ansys 2021. Ansys student. <https://www.ansys.com/academic/students/ansys-student>, 2021. Free workbench-based bundle for students. The workbench includes the Aqwa application, which can generate potential-flow solutions. Accessed 2021-11-11.
- API changes. Api changes for updating openfast. https://openfast.readthedocs.io/en/main/source/user/api_change.html, 2021. Check for changes to input file needed for updating to a newer version of OpenFAST.
- Q. Bai and Y. Bai. Hydrodynamics around Pipes. In *Subsea Pipeline Design, Analysis, and Installation*, pages 153–170. 2014. ISBN 9780123868886. doi: 10.1016/b978-0-12-386888-6.00007-9. URL <https://www.sciencedirect.com/science/article/pii/B9780123868886000079>.
- G. S. Bir. User’s guide to BModes. *National Renewable Energy Laboratory*, (September), 2007. URL <https://nwtc.nrel.gov/system/files/BModes.pdf>.
- CoreWind, 2021. CoreWind about the corewind project. <http://corewind.eu/about/>, 2021. Accessed: 2021-10-26.
- A. Drivenes, T. Eirum, N. H. Johnson, S. K. Mindeberg, S. Lunde, L. S. Udem, K. Veggeland, B. Veie-Rosvoll, and A. Voksø. Forslag til utredningsområder. Technical report, 2010. URL https://www.regjeringen.no/globalassets/upload/oed/rapporter/havvind_{_}ver02.pdf.
- Equinor2021. Equinor - what we do. <https://www.equinor.com/en/what-we-do/floating-wind.html>, 2021.
- J. Fredsoe and B. M. Sumer. *Hydrodynamics Around Cylindrical Structures (Revised Edition)*, volume 26, chapter 4, pages 123–209. World Scientific Publishing Company, Singapore, 2006. ebook isbn: 9789812772770.
- K. Freeman, C. Frost, G. Hundleby, A. Roberts, B. Valpy, H. Holttinen, L. Ramírez, and I. Pineda. Our Energy Our Future. page 78, 2019.
- B. R. Furevik and H. Haakenstad. Near-surface marine wind profiles from rawinsonde and nora10 hindcast. *Journal of Geophysical Research: Atmospheres*, 117(D23), 2012.

- doi: <https://doi.org/10.1029/2012JD018523>. URL
<https://agupubs.onlinelibrary.wiley.com/doi/abs/10.1029/2012JD018523>.
- E. Gaertner, J. Rinker, L. Sethuraman, F. Zahle, B. Anderson, G. Barter, N. Abbas, F. Meng, P. Bortolotti, W. Skrzypinski, G. Scott, R. Feil, H. Bredmose, K. Dykes, M. Sheilds, C. Allen, and A. Viselli. Definition of the IEA 15-Megawatt Offshore Reference Wind Turbine, BModes input. NREL/TP-75698, 2020a. URL
https://github.com/IEAWindTask37/IEA-15-240-RWT/blob/master/OpenFAST/IEA-15-240-RWT/BModes/IEA-15-240-RWT_BModes_tower.bmi. Accessed: 2021-09-29.
- E. Gaertner, J. Rinker, L. Sethuraman, F. Zahle, B. Anderson, G. E. Barter, N. J. Abbas, F. Meng, P. Bortolotti, W. Skrzypinski, G. N. Scott, R. Feil, H. Bredmose, K. Dykes, M. Shields, C. Allen, and A. Viselli. IEA Wind TCP Task 37: Definition of the IEA 15-Megawatt Offshore Reference Wind Turbine. pages 1–44, 2020b. URL
<https://www.nrel.gov/docs/fy20osti/75698.pdf>.
- N. Government. Regjeringen 2020. 2020. The Norwegian government: Utsira Nord and Sørlige Nordsjø II are open for concession applications. URL:
<https://www.regjeringen.no/en/topics/energy/vindkraft-til-havs-tidslinje/id2873850/> ,
Accessed 2021-11-11.
- Green Deal, 2021. European commission green deal, 2020. URL https://ec.europa.eu/info/strategy/priorities-2019-2024/european-green-deal_en.
The European Green Deal, by the European Commission. Accessed 21.11.2021.
- K. F. Hasselmann, T. P. Barnett, E. Bouws, H. Carlson, D. E. Cartwright, K. Eake, J. Euring, A. Gicnapp, D. Hasselmann, P. Kruseman, et al. Measurements of wind-wave growth and swell decay during the joint north sea wave project (jonswap). *Ergaenzungsheft zur Deutschen Hydrographischen Zeitschrift, Reihe A*, 1973.
- HAWC2. Mann Turbulence Generator the mann 64bit turbulence generator, developed by hawc2. <https://www.hawc2.dk/download/pre-processing-tools>. Accessed: 2021-03-12.
- Hywind Demo, 2009. The hywind demo project, 2009.
<https://www.equinor.com/no/what-we-do/floating-wind/hywind-demo.html>, 2021.
Description of the Hywind Demo project. This is the first installed multi-megawatt floating wind turbine using the spar concept. Accessed 21.11.2021.
- Hywind Scotland, 2017. Equinor - the future of offshore wind is afloat.
<https://www.equinor.com/no/what-we-do/floating-wind.html>, 2021. Description of the Hywind Scotland offshore floating wind farm. Accessed 09.11.2021.
- IEC 61400-1. Iec 61400-1:2019. <https://webstore.iec.ch/publication/26423>, 2019.
International Electrotechnical Commission. IEC 61400-1:2019 Wind energy generation systems - Part 1: Design requirements.
- IEC TS 61400-3-2:2019. Wind energy generation systems - Part 3-2: Design requirements for floating offshore wind turbines. Standard, International Electrotechnical Commission, May 2019.
- Intel Fortran Compiler. Intel fortran compiler. Downloaded at
<https://www.intel.com/content/www/us/en/developer/articles/tool/redistributable->

- libraries-for-intel-c-and-fortran-2020-compilers-for-windows.html, 2020. Download date: 02/02/2021.
- J. Jonkman. An online discussion about force-displacement relationship of oc4 deepcwind mooring sys, Nov. 2005. URL <https://wind.nrel.gov/forum/wind/viewtopic.php?f=4&t=1123&p=10717>. Posted Nov 03, 2005, 4:38 pm.
- J. Jonkman. Definition of the floating system for phase iv of oc3. 5 2010. doi: 10.2172/979456. URL <https://www.osti.gov/biblio/979456>.
- J. Jonkman. BModes Source the google drive containing bmodes .exe files, user's guide, and input files for oc3hywind and cs_monopile projects. <https://drive.google.com/drive/folders/1FMtJ7BbTR03hme0wsrXxHezksGRnrqxJ>, 2020. Accessed: 2021-09-20.
- J. Jonkman and W. Musial. Offshore code comparison collaboration (oc3) for iea wind task 23 offshore wind technology and deployment. 12 2010. doi: 10.2172/1004009. URL <https://www.osti.gov/biblio/1004009>.
- J. Jonkman, S. Butterfield, W. Musial, and G. Scott. Definition of a 5-mw reference wind turbine for offshore system development. 2 2009. doi: 10.2172/947422. URL <https://www.osti.gov/biblio/947422>.
- M. Y. Mahfouz, M. Salari, S. Hernández, F. Vigar, C. Molins, and P. Trubat. D1.3 Public design and FAST models of the two 15MW floater-turbine concepts. (April), 2020.
- J. Mann. The Spatial Structure of Neutral Atmospheric Surface-Layer Turbulence. *Journal of Fluid Mechanics*, 273:141–168, 1994. ISSN 14697645. doi: 10.1017/S0022112094001886.
- C. Molins, P. Trubat, and M. Y. Mahfouz. UPC - WINDCRETE OpenFAST model 15MW FOWT - Grand Canary Island, Dec. 2020. URL <https://doi.org/10.5281/zenodo.4322446>.
- MoorDyn 2021. Moordyn online documentation. <https://moordyn.readthedocs.io/en/latest/index.html>, 2021. Online documentation site under construction. Accessed 2021-11-11.
- F. G. Nielsen. Floating support structures. Personal correspondence. Unpublished lecture notes., 4 2021.
- NREL. OpenFAST Documentation Release v2.5.0. pages 1–101, 2020a. URL <https://openfast.readthedocs.io/en/dev/index.html>.
- NREL. ROSCO. Version 2.0.1, 2020b. URL <https://github.com/NREL/ROSCO/releases/tag/v2.0.1>. Accessed: 2021-29-09.
- NREL. ROSCO. Version 2.3.0, 2021. URL <https://github.com/NREL/rosco>. Accessed: 2021-02-09.
- OpenFAST binaries. Openfast v2.5.0 binaries. Binaries available at <https://github.com/OpenFAST/openfast/releases/tag/v2.5.0>, 2021. Updating version requires API changes.

- P. Petrova and C. Guedes Soares. Maximum wave crest and height statistics of irregular and abnormal waves in an offshore basin. *Applied Ocean Research*, 30(2):144–152, 2008. ISSN 01411187. doi: 10.1016/j.apor.2008.08.004.
- I. Prowell. Get FAST style polynomial matlab routine direct link to download the matlab routine created by ian prowell for finding the 6th order polynomial required as input in openfast. this link was provided by jason jonkman in a nrel forum discussion. link is for direct download. <https://wind.nrel.gov/forum/wind/download/file.php?id=1678>, 2017. Accessed: 2021-09-21.
- M. Reistad, O. Breivik, H. Haakenstad, O. J. Aarnes, B. R. Furevik, and J.-R. Bidlot. A high-resolution hindcast of wind and waves for the north sea, the norwegian sea, and the barents sea. *Journal of Geophysical Research: Oceans*, 116(C5), 2011. doi: <https://doi.org/10.1029/2010JC006402>. URL <https://agupubs.onlinelibrary.wiley.com/doi/abs/10.1029/2010JC006402>.
- P. Skeie, D. J. Steinskog, and J. Näs. *Kraftproduksjon og vindforhold*. 2012. ISBN 9788241008481.
- R. B. Stull. *An Introduction to Boundary Layer Meteorology*, volume 13. Springer Netherlands, 1 edition, 7 1988. ISBN 9789400930278.
- W. T. Thomson and M. D. Dahleh. *Theory of Vibration with Applications*, volume 5. Prentice-Hall Inc., 2005.
- A. S. Vatshelle. *Investigation of the dynamic response of a spar FOWT , and its sensitivity to variations in draft*. PhD thesis, The University of Bergen, 2020. URL <https://hdl.handle.net/1956/23119>.
- D. N. Veritas. Recommended practice dnv-rp-c205: environmental conditions and environmental loads. *DNV, Norway*, 2010.
- F. Vigarra, L. Cerdán, R. Durán, S. Muñoz, M. Lynch, S. Doole, C. Molins, P. Trubat, and R. Guanache. D1.2 design basis. (August), 2020. URL <http://corewind.eu/wp-content/uploads/files/publications/COREWIND-D1.2-04-Design-Basis.pdf>.
- WAMIT 2021. Wamit. <https://www.wamit.com/>, 2021. WAMIT is an advanced set of tools for analyzing wave interactions with offshore platforms and other structures or vessels. Accessed 2021-11-11.
- WindEurope. Offshore wind in Europe - Key trends and statistics 2020. *WindEurope*, 3(2):14–17, 2021. ISSN 14710846.
- Windfloat Atlantic, 2021. The windfloat atlantic project. <https://www.offshorewind.biz/2021/09/24/floating-wind-farm-offshore-portugal-overdelivers/>, 2020. Description of the Windfloat Atlantic project. This is the first semi-submersible wind farm in operation, located off the coast of Portugal. Accessed 21.11.2021.

Appendices

A OPENFAST INPUT

ElastoDyn input

Table 26: Distributed Tower Properties

| Height fraction (-) | Mass density [kg/m] | Fore-aft stiffness [Nm ²] | Side-to-side stiffness [Nm ²] |
|------------------------|------------------------|--|--|
| 0.00 | 1.657108e+04 | 7.457729e+12 | 7.457729e+12 |
| 0.05 | 1.560079e+04 | 6.746782e+12 | 6.746782e+12 |
| 0.10 | 1.480248e+04 | 6.146014e+12 | 6.146014e+12 |
| 0.15 | 1.413040e+04 | 5.627674e+12 | 5.627674e+12 |
| 0.20 | 1.354573e+04 | 5.169989e+12 | 5.169989e+12 |
| 0.25 | 1.301631e+04 | 4.756360e+12 | 4.756360e+12 |
| 0.30 | 1.251633e+04 | 4.374594e+12 | 4.374594e+12 |
| 0.35 | 1.202599e+04 | 4.016202e+12 | 4.016202e+12 |
| 0.40 | 1.153113e+04 | 3.675738e+12 | 3.675738e+12 |
| 0.45 | 1.102289e+04 | 3.350210e+12 | 3.350210e+12 |
| 0.50 | 1.049734e+04 | 3.038530e+12 | 3.038530e+12 |
| 0.55 | 9.955036e+03 | 2.741037e+12 | 2.741037e+12 |
| 0.60 | 9.400639e+03 | 2.459067e+12 | 2.459067e+12 |
| 0.65 | 8.842496e+03 | 2.194578e+12 | 2.194578e+12 |
| 0.70 | 8.292200e+03 | 1.949826e+12 | 1.949826e+12 |
| 0.75 | 7.764137e+03 | 1.727096e+12 | 1.727096e+12 |
| 0.80 | 7.275024e+03 | 1.528469e+12 | 1.528469e+12 |
| 0.85 | 6.843428e+03 | 1.355645e+12 | 1.355645e+12 |
| 0.90 | 6.489264e+03 | 1.209790e+12 | 1.209790e+12 |
| 0.95 | 6.233268e+03 | 1.091439e+12 | 1.091439e+12 |
| 1.00 | 6.096451e+03 | 1.000417e+12 | 1.000417e+12 |

AeroDyn input

Table 27: The final diameters throughout the tower height. This data is required as input in the AeroDyn submodule.

| Height above MSL [m] | Tower diameter [m] |
|----------------------|--------------------|
| 15.00 | 12.42 |
| 25.00 | 12.01 |
| 35.00 | 11.61 |
| 45.00 | 11.20 |
| 55.00 | 10.79 |
| 65.00 | 10.39 |
| 75.00 | 9.98 |
| 85.00 | 9.57 |
| 95.00 | 9.16 |
| 105.00 | 8.76 |
| 115.00 | 8.35 |
| 125.00 | 7.94 |
| 135.00 | 7.54 |
| 135.90 | 7.50 |

B OPENFAST OUTPUT

8 m/s steady wind

Table 28: Some input parameters and initial values for 8 m/s steady wind.

| Parameter | Initial/input value | Unit |
|--------------------|---------------------|-------|
| Mean wind | 8.0 | [m/s] |
| Power Law exponent | 0.06 | (-) |
| Rotor speed | 5.7 | [rpm] |
| Blade pitch | 0.0 | [deg] |
| Wave H_s | 0.6 | [m] |
| Wave T_p | 4.2 | [s] |
| Surge | 5.9 | [m] |
| Pitch | 2.0 | [deg] |
| Heave | -0.3 | [deg] |
| Yaw | 0.0 | [deg] |

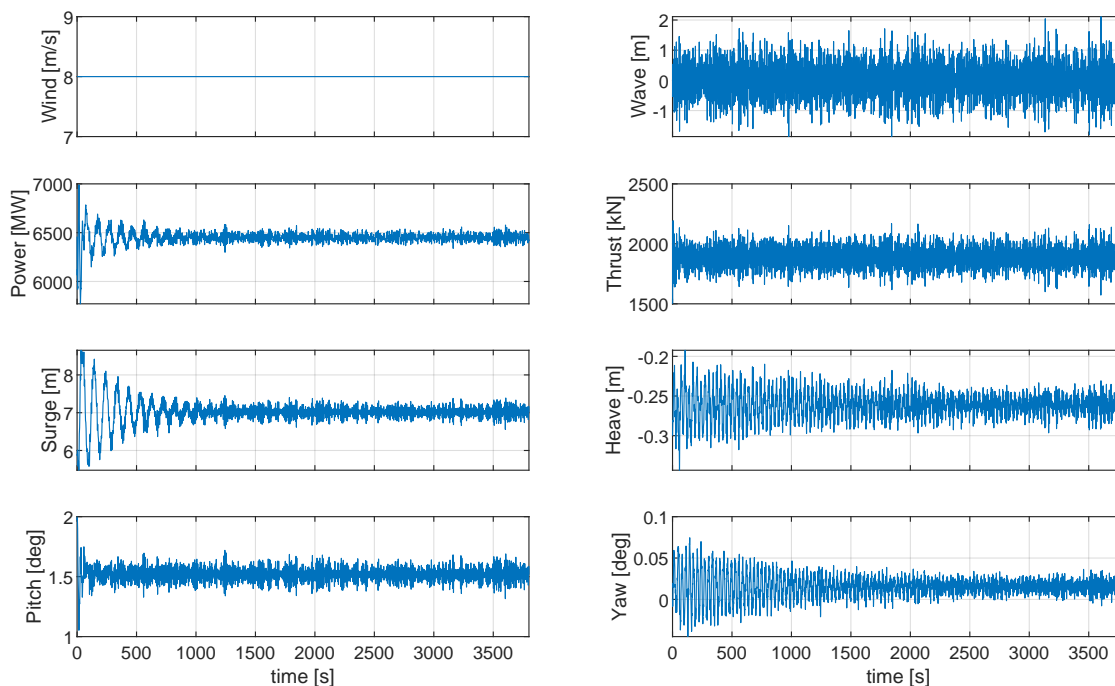


Figure 37

The ranges of motion is calculated from a time series of 3800 s. I exclude the first 1800 s from the calculations, to avoid any transients to impact the output data. Figure 37 shows prominent start-up transients in surge, but almost no visible start-up transients in pitch. Platform surge stabilizes much faster than what we see in Figure 30. The variations in power are small, caused by the stochastic waves.

Table 29: Ranges of motion in the 8 m/s steady wind simulation.

| Surge maximum [m] | Surge average [m] | Pitch maximum [deg] | Pitch average [deg] | Yaw maximum [deg] | Yaw average [deg] |
|-------------------|-------------------|---------------------|---------------------|-------------------|-------------------|
| 7.39 | 7.02 | 1.69 | 1.52 | 0.04 | 0.02 |

18 m/s steady wind

Table 30: Some input parameters and initial values for 18 m/s steady wind.

| Parameter | Initial/input value | Unit |
|--------------------|---------------------|-------|
| Mean wind | 18.0 | [m/s] |
| Power Law exponent | 0.06 | (-) |
| Rotor speed | 7.54 | [rpm] |
| Blade pitch | 15.56 | [deg] |
| Wave H_s | 3.43 | [m] |
| Wave T_p | 8.62 | [s] |
| Surge | 4.6 | [m] |
| Pitch | 1.7 | [deg] |
| Heave | -0.3 | [deg] |
| Yaw | -0.4 | [deg] |

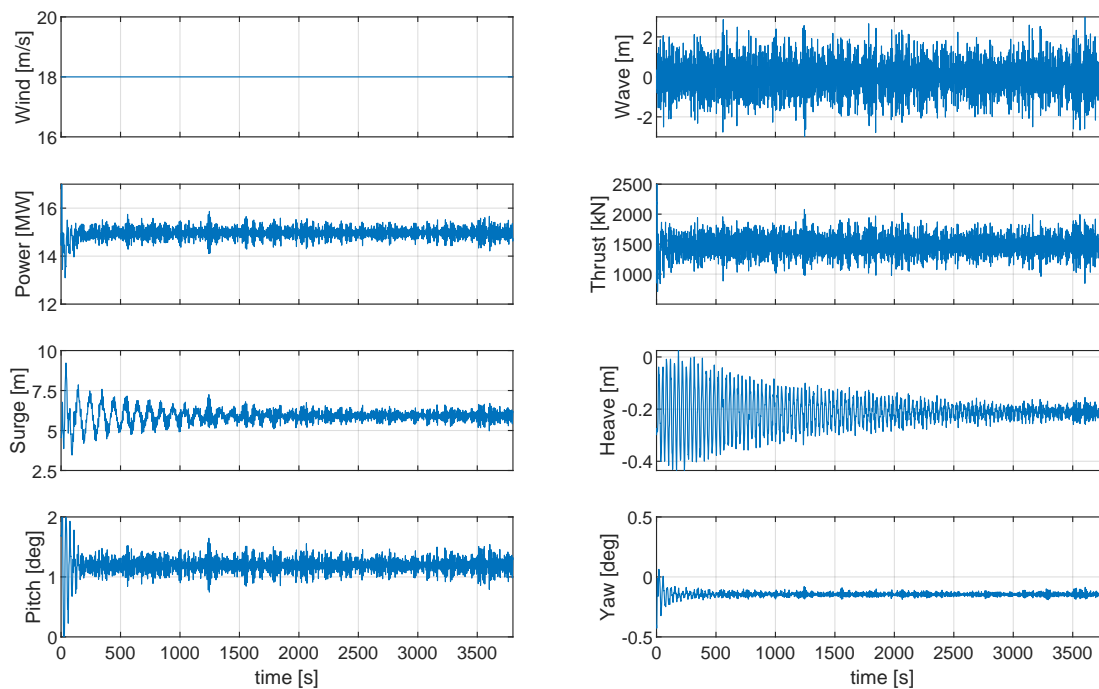


Figure 38

Figure 38 shows that the model is stable for the non-realistic case of 18 m/s steady wind. The average thrust force is relatively low, and the power output varies around 15 MW, as expected. The average platform pitch is just above 1 deg, with very little variation. This is as expected, as the wave spectre is relatively weak.

Table 31: Range of motions for the 18 m/s steady wind simulation.

| Surge maximum [m] | Surge av- erage [m] | Pitch maximum [deg] | Pitch average [deg] | Yaw maximum [deg] | Yaw average [deg] |
|-------------------------|------------------------|---------------------------|---------------------------|-------------------------|-------------------------|
| 6.74 | 5.91 | 1.55 | 1.19 | -0.19 | -0.15 |

